HIGH-PERFORMANCE READOUT CIRCUIT FOR RESONATOR-BASED MEMS ACCELEROMETER USING DIGITAL CONTROL LOOP

A THESIS SUBMITTED TO
THE GRADUATE SCHOOL OF NATURAL AND APPLIED SCIENCES
OF
MIDDLE EAST TECHNICAL UNIVERSITY

BY

MUHAMMAD ALI

IN PARTIAL FULFILLMENT OF THE REQUIREMENTS
FOR
THE DEGREE OF DOCTOR OF PHILOSOPHY
IN
ELECTRICAL AND ELECTRONIC ENGINEERING

NOVEMBER 2022

Approval of the thesis:

HIGH-PERFORMANCE READOUT CIRCUIT FOR RESONATOR-BASED MEMS ACCELEROMETER USING DIGITAL CONTROL LOOP

submitted by **MUHAMMAD ALI** in partial fulfillment of the requirements for the degree of **Doctor of Philosophy** i**n Electrical and Electronic Engineering, Middle East Technical University** by,

Prof. Dr. Halil Kalıpçılar
Dean, Graduate School of **Natural and Applied Sciences** _____

Prof. Dr. İlkay Ulusoy
Head of the Department, **EEE, METU** _____

Prof. Dr. Tayfun Akın
Supervisor, **EEE, METU** _____

Examining Committee Members:

Prof. Dr. Haluk Külah
Electrical and Electronics Eng., METU _____

Prof. Dr. Tayfun Akın
Electrical and Electronics Eng., METU _____

Assoc. Prof. Dr. Kıvanç Azgın
Mechanical Engineering, METU _____

Asst. Prof. Dr. Yakup Özkazanç
EEE, Hacettepe University _____

Asst. Prof. Dr. Erdinç Tatar
EEE, Bilkent University _____

Date: 29.11.2022

I hereby declare that all information in this document has been obtained and presented in accordance with academic rules and ethical conduct. I also declare that, as required by these rules and conduct, I have fully cited and referenced all material and results that are not original to this work.

Name Last name : Muhammad Ali

Signature :

ABSTRACT

HIGH-PERFORMANCE READOUT CIRCUIT FOR RESONATOR-BASED MEMS ACCELEROMETER USING DIGITAL CONTROL LOOP

Ali, Muhammad
Doctor of Philosophy, Electrical and Electronic Engineering
Supervisor: Prof. Dr. Tayfun Akın

November 2022, 161 pages

This study proposes a new digital control loop-based compact readout circuit for a resonant MEMS accelerometer providing high performance with reduced temperature and power supply dependence while utilizing low processing power. The readout circuit utilizes a charge-sensing pre-amplifier stage that converts the small motional current to readable voltage, which is then converted to the digital domain using a 16-bit ADC to perform the amplitude and frequency extraction in the digital domain. A Proportional Integral (PI) controller is used to maintain the sensor output at a stable value. The frequency tracking is performed by implementing a Phase-Locked-Loop (PLL) in the digital domain. A timed reference signal technique used in this study reduces the computational requirements for the PLL implementation. A drive signal is generated based on the demodulated frequency and amplitude, and a DAC is used to transfer the signal to the resonators.

Chip-level characterization of several resonant MEMS accelerometer sensors is performed with a dynamic signal analyzer (DSA). A lock-in-amplifier is used to characterize different sensor parameters. The frequency-sweeping tests are performed to obtain resonance frequency and gain of the resonators. The PLL and

PI controllers, available in the lock-in-amplifier software, are used to operate the sensors in a closed loop.

The digital PCB realization is performed using one of the characterized resonant MEMS accelerometers. A frequency-sweeping algorithm is used to obtain the resonance frequency of the resonators under different biasing conditions: 3V to 10V proof mass voltage and 0.1mV to 1mV excitation voltage. The resonance frequency of the resonators is approximately 16485Hz and 16720Hz. The readout circuit accurately and repeatedly measures the resonance frequency of the resonators, and the results are consistent with the sensor characterization results. The frequency-sweeping tests also show that a high value of excitation voltage drives the resonators in the non-linear region. The scale factor calculated with the readout circuit is 95Hz/g which is stable under all the biasing conditions. The sensitivity of the individual resonators is different: 45Hz/g for *Resonator 1* and 50Hz/g for *Resonator 2*. This configuration achieves a bias instability of 9.7µg, which can be further reduced with a better MEMS accelerometer design, and this value is very close to the bias instability obtained using a lock-in-amplifier setup. Testing with a pure sine generator shows that this readout circuit can achieve a 0.3µg/√Hz noise level. The system's bandwidth is approximately 68Hz, which can be improved by sacrificing the noise performance. The temperature compensation improves the bias instability of the sensor by 3 times. The differential resonator design is ideally immune to temperature, but the difference in the sensitivity of the resonators due to fabrication-related problem make the sensor data dependent on the temperature.

Keywords: MEMS, Resonant Accelerometer, Digital Control Loop, Readout Circuit

ÖZ

DİJİTAL KONTROL DÖNGÜLERİ KULLANARAK MEMS TİTREŞEN YAY TİPİ İVMEÖLÇER İÇİN YÜKSEK PERFORMANSLI OKUMA DEVRESİ GELİŞTİRİLMESİ

Ali, Muhammad
Doktora, Elektrik ve Elektronik Mühendisliği
Tez Yöneticisi: Prof. Dr. Tayfun Akın

Kasım 2022, 161 sayfa

Bu çalışma, düşük sıcaklık ve güç kaynağı bağımlılığına sahip yüksek performanslı bir rezonant ivmeölçer için yeni bir düşük güç tüketimine sahip dijital tabanlı okuma devresi önermektedir. Okuma devresi, küçük hareket akımını okunabilir voltaja dönüştüren, daha sonra dijital alanda genlik ve frekans çıkarımını gerçekleştirmek için 16 bitlik bir ADC kullanılarak dijital alana dönüştürülen bir şarj algılayıcı ön amplifikatör aşaması kullanır. Sensör çıkışını sabit bir değerde tutmak için Oransal-İntegral (PI) denetleyici kullanılır. Frekans izleme, dijital alanda bir Faz-Kilitli-Döngü (PLL) uygulanarak gerçekleştirilir. Bu çalışmada kullanılan zaman ayarlı bir referans sinyal tekniği, PLL uygulaması için hesaplama gereksinimlerini azaltır. Demodüle edilmiş frekans ve genliğe dayalı olarak bir sürüş sinyali üretilir ve sinyali rezonatörlere aktarmak için bir dijitalden analoğa çevirici (DAC) kullanılır.

Birkaç ivmeölçer sensörünün çip düzeyinde karakterizasyonu, bir dinamik sinyal analizörü (DSA) ile gerçekleştirilir. Farklı sensör parametrelerini karakterize etmek için bir kilitli yükseltici cihazı kullanılır. Rezonatörlerin rezonans frekansını ve kazancını elde etmek için frekans tarama testleri yapılır. Kilitli yükseltici cihazı yazılımında bulunan PLL ve PI kontrolcüleri, sensörleri kapalı bir döngüde çalıştırmak için kullanılır.

Dijital PCB üzerindeki testler, karakterize edilen rezonanslı MEMS ivmeölçerden biri kullanılarak gerçekleştirilir. Farklı ön gerilim koşulları altında rezonatörlerin rezonans frekansını elde etmek için bir frekans süpürme algoritması kullanılır: 3V ila 10V arası ataletsel kütle voltajı ve 0.1mV ila 1mV uyarma voltajı. Rezonatörlerin rezonans frekansı yaklaşık olarak 16485Hz ve 16720Hz'dir. Okuma devresi, rezonatörlerin rezonans frekansını doğru ve tekrar eden şekilde ölçer ve sonuçlar, sensör karakterizasyon sonuçlarıyla tutarlıdır. Frekans tarama testleri ayrıca yüksek bir uyarma gerilimi değerinin doğrusal olmayan bölgede rezonatörleri tahrik ettiğini gösterir. Okuma devresi ile hesaplanan ölçek faktörü, tüm ön gerilim koşulları altında kararlı olan 95Hz/g'dir. Her bir rezonatörün ölçüm hassasiyeti farklıdır: rezonatör 1 için 45Hz/g ve rezonatör 2 için 50Hz/g. Bu konfigürasyon ile, daha iyi bir MEMS ivmeölçer tasarımı ile daha da azaltılabilecek olan 9.7µg'lik bir sapma kararsızlığı değerine ulaşılır ve bu değer kilitli yükseltici cihazı ile elde edilen değere yakındır. Dışarıdan uygulanan temiz sinüs sinyali ile elde edilen gürültü değeri 0.3µg/√Hz'dir. Sistemin bant genişliği 68Hz'dir ve bu değer gürültü performansından feragat ederek iyileştirilebilir. Sıcaklık kompanzasyonu, sensörün sabit kayma hatası kararsızlığını 3 kat iyileştirir. Diferansiyel rezonatör tasarımı ideal olarak sıcaklığa karşı bağışıktır, ancak üretimde yaşanan sorunlar nedeniyle rezonatörlerin duyarlılığındaki fark, sensör verilerini sıcaklığa bağımlı hale getirir.

Anahtar Kelimeler: MEMS, Rezonans Tabanlı İvmeölçer, Dijital Kontrol Döngüsü, Okuma Devresi

Dedicated to my family.

ACKNOWLEDGMENTS

I want to express my gratitude to my supervisor, Prof. Dr. Tayfun Akın, for his guidance, advice, criticism, and encouragement throughout the research.

I also thank my Thesis-Monitoring-Committee members, Prof. Dr. Haluk Külah and Assoc. Prof. Dr. Kıvanç Azgın, for their time and sightful comments throughout this study.

I would also like to express my gratitude to the external Jury members, Dr. Erdinç Tatar and Dr. Yakup Özkazanç, for their precious time and valuable comments for the improvement of this thesis.

I wish to express my gratitude to Dr. Said Emre Alper for his advice, suggestions, technical support, and insight throughout this study.

I would also like to acknowledge Hasan Doğan for his suggestions, comments, and understanding of the mechanical design of the sensor.

I would also like to thank Ferhat Yeşil for his suggestions and insight into programming the digital control loop.

I would also like to thank the staff of Mikrosistemler for all the technical support they provided throughout the testing period.

TABLE OF CONTENTS

LIST OF TABLES

TABLES

LIST OF FIGURES

FIGURES

LIST OF ABBREVIATIONS

MEMS	Micro Electro Mechanical Systems
RMA	Resonating MEMS Accelerometer
VPM	Proof Mass Voltage
PLL	Phase Locked Loop
HF2L	High-Frequency Lock-in-Amplifier
DSA	Dynamic Signal Analyzer
DETF	Double-Ended Tuning Fork
ADC	Analog to Digital Converter
DAC	Digital to Analog Converter
FPGA	Field Programmable Gate Array
SPI	Serial Peripheral Interface
UART	Universal Asynchronous Receiver Transmitter
PID	Proportional Integral Derivative
VCO	Voltage Controlled Oscillator
DCO	Digitally controlled Oscillator

CHAPTER 1

INTRODUCTION

Micro Electro Mechanical Systems (MEMS) based sensors are used in a number of applications ranging from commercial devices to high-performance inertial applications [1-3] for sensing pressure, acceleration, angular rotation, temperature, sound signals, infrared radiation, etc. MEMS sensors also have applications in medical areas, including surgical instruments, portable test equipment, miniature labs, and monitoring devices [4]. The MEMS market is growing at 13% annually [1], and this increase results from many advantages in the practical applications of MEMS sensors. The miniature size of a MEMS device is the first advantage that attracts space-constraint applications, as several sensors can be incorporated into a tiny space to achieve high performance. Multiple MEMS sensors have started to be included in mobile phones or intelligent gadgets for adding various capabilities to these devices. The second advantage of MEMS sensors is their cost-effectiveness, making them desirable for many commercial applications. Cost-effectiveness comes from the fact that MEMS sensors are produced at the wafer level in batches, where a single wafer can contain many MEMS devices, significantly reducing the fabrication cost of a single device. With the advancement of the fabrication techniques and the improvements in the designs, the MEMS sensors started to achieve higher and higher performances in higher operation temperature ranges, allowing their use in high-performance applications, like inertial grade MEMS accelerometers and gyroscopes [5].

Extensive research has been carried out in the last few decades to improve the performance of MEMS inertial sensors, especially on MEMS accelerometers; various high-performance MEMS accelerometers are reported with performances

satisfying inertial-grade applications [6, 7]. MEMS accelerometers are essential to several applications that require positioning or navigation. The acceleration information can be extracted from a sensing element using different techniques, resulting in different types of MEMS accelerometers. Resonant MEMS accelerometers are one of the several types of MEMS accelerometers, which have been developed since the 1990s[8, 9] due to their advantages compared to other MEMS accelerometer types. Resonant MEMS accelerometers are distinguished due to their advantages, such as quasi-digital output simplifying digitization, high sensitivity, improved dynamic range, insensitivity to temperature and power supply variations, and low electronic noise.

Many readout schemes are used to operate a resonant MEMS accelerometer. All readout circuits have three essential components: a pre-amplifier stage to convert the motional current to voltage, an oscillation-sustaining part that keeps the resonators operating in a closed loop, and a frequency extraction or reading part that converts the demodulated frequency to a digitally readable format. Implementing a digital control loop has advantages such as frequency-friendly interfacing, flexibility to change parameters, multiple algorithms without increasing hardware complexity, an easy debugging process, and modification of performance parameters. This study proposes a new digital control loop-based compact readout circuit for a resonant MEMS accelerometer providing high performance with reduced temperature and power supply dependence while utilizing low processing power.

This chapter briefly gives an introduction to the MEMS accelerometer and reviews some previous efforts in the development of resonant MEMS accelerometers. Section 1.1 overviews different types of MEMS accelerometers available in the literature. Section 1.2 mentions a few advantages of resonant MEMS accelerometers that make them an attractive choice for many applications. Section 1.3 overviews some distinguished literature on the sensor and the readout circuit design. Section 1.4 explains the motivation for this study. Section 1.5 describes the aims of this research. Section 1.6 outlines the topics discussed in different chapters of this thesis.

1.1 Types of MEMS Accelerometers

Different techniques are available in the literature for the fabrication of MEMS accelerometers. The applied acceleration affects a sensing element in different ways, changing various parameters like capacitance, resistance, temperature, or resonance frequency due to acceleration. There are other MEMS accelerometer types, such as tunneling and electromagnetic accelerometers, but they are rarely used due to their disadvantages. This section presents a brief introduction to the most popular types of MEMS accelerometers, including piezoresistive, piezoelectric, thermal, optical, capacitive, and resonance-based accelerometers.

1.1.1 Piezoresistive Accelerometer

The resistance of piezoresistive materials changes under stress. The working principle of a piezoresistive MEMS accelerometer is based on the fact that the resistance of the sensing element changes with applied acceleration. The stress in the piezoresistive material changes under acceleration, causing a change in its resistance. Different techniques can measure this resistance change. A commonly used technique is to use a Wheatstone bridge circuit for measuring the resistance variation. The drawback of this technique is the dependence of resistance on temperature [10, 11], i.e., the resistance change due to temperature is inseparable from resistance change due to applied acceleration. Piezoresistive accelerometers have low sensitivity and high drift compared to other MEMS accelerometers.

1.1.2 Piezoelectric Accelerometer

This type of MEMS accelerometer uses the piezoelectric property of sensing elements, where the applied acceleration introduces stress in a sensing element that generates a charge. This charge is converted to voltage and translated to corresponding acceleration [12]. There are a few disadvantages of MEMS

piezoelectric accelerometers. Mainly, the sensitivity of the piezoelectric accelerometer is unstable near its resonance frequency. These sensors are not suitable for low-frequency measurements.

1.1.3 Thermal Accelerometer

Thermal accelerometers work on the heat flow principle between a heater and a sink due to applied acceleration. A micro-heater acts as a heat source and generates a bubble of heated air that acts as the proof mass of the sensor. Two temperature sensors measure temperature at the opposite sides of this heater. Acceleration can either increase or decrease the heat flow between the heater and the temperature sensors. The change in the measured temperatures determines the direction and intensity of the applied acceleration. The main drawback of this type of sensor is low sensitivity [13]. The sensors suffer from low bandwidth, and drift exists in their output. They are unsuitable for power constraint applications because they consume much power. They are also sensitive to environmental temperature.

1.1.4 Optical Accelerometer

Optical accelerometers work on the principle that the light intensity of two light waves traveling in the core and cladding of an optical fiber changes with applied acceleration [14]. The difference in intensity relates to input acceleration. These sensors have high power consumption. Intensity noise, due to quantum noise, vibrations of cavity mirrors, and thermal fluctuations in the gain medium, limit the performance of these sensors.

1.1.5 Capacitive Accelerometer

Capacitive accelerometers are the most commonly fabricated type of MEMS accelerometers. The capacitance between the proof mass and electrodes becomes a

function of acceleration. An applied acceleration generates a force displacing the proof mass; this displacement results in a change of capacitance which then converts to charge and voltage. The sensed voltage can be mapped to applied acceleration [15]. Equation 1.1 shows the relation between input acceleration and output voltage:

$$V\left(\Delta C\left(x_F\left(a\right)\right)\right) \qquad 1.1$$

Where a is the input acceleration, x_f is the displacement caused by this acceleration, ΔC is the change in capacitance due to displacement of electrodes, and V is the output voltage.

Capacitive sensors have high sensitivity, extensive range, low power consumption, and low-temperature dependence; therefore, they dominate accelerometer types in the market, and they are highly studied in the literature. However, their performance is not enough for very high-performance applications due to drifts caused by their temperature dependence.

1.1.6 Resonant Accelerometer

Resonating or vibrating beam MEMS accelerometers are becoming popular for high-performance applications. They work on the principle that the resonance frequency of a resonating beam changes with applied acceleration [8], where the applied acceleration causes compression or tension in the vibrating beam resulting in a decrease or increase in its resonance frequency [8, 16]. This change in resonance frequency can be translated into an applied acceleration. Equation 1.2 shows the relation between the input acceleration and output frequency:

$$f\left(V\left(\Delta C\left(x\left(a\right)\right)\right)\right) \qquad 1.2$$

Where a is the input acceleration, x is the displacement caused by this acceleration, ΔC is the change in capacitance, V is the voltage obtained from motion current, and f is the output frequency.

The resonant MEMS accelerometers are becoming increasingly popular for applications requiring very high performance without being affected by temperature variations. The focus of the current study is the development of a digital control loop-based readout circuit for resonant MEMS accelerometers. The following section presents the advantages of resonant MEMS accelerometers.

1.2 Advantages of Resonating MEMS Accelerometers

Resonant MEMS accelerometers have several advantages when compared to other types of MEMS accelerometers. The following sub-sections provide brief information on these advantages.

1.2.1 Quasi-digital Output

The output of the resonant MEMS accelerometer is a frequency that easily converts to a digital domain. The resonant MEMS accelerometers with analog closed loops also have a frequency output that requires a frequency reading interface [8, 17-19]. Conversion of frequency or acceleration information to the digital domain has several advantages; more specifically, (i) signal conditioning improves the quality of the signal, and (ii) several noise sources can be suppressed by signal conditioning.

1.2.2 Sensitivity

The sensitivity of a resonant MEMS accelerometer can be increased by increasing the size of the proof mass. However, a lever system introduced in some resonant MEMS accelerometer designs can increase the sensitivity even without increasing the size of the proof mass [19-22]. The purpose of the lever system is to transfer more force to the vibrating beams when the proof mass displaces as a result of applied acceleration. However, the size of the proof mass is inversely proportional

to the Brownian noise of the structure [23]. The proof-mass size should be chosen, considering the system's desired level of Brownian noise.

1.2.3 Dynamic Range

The dynamic range of a resonant MEMS accelerometer is improved because the applied acceleration is along the vibrating beam axis. The dynamic range is limited if the direction of sensitivity is lateral to the beam axis [3, 8, 9, 17, 19]. In a resonant MEMS accelerometer, the range of linear operation is increased due to the axial loading (compression or tension) of the beam.

1.2.4 Immunity to Temperature

Temperature is one of the main factors that degrade the performance of MEMS sensors [5, 24, 25]. The performance of MEMS sensors degrades because of the drift caused by temperature changes. Resonant MEMS accelerometers are more immune to temperature effects than other accelerometers [26]. Current designs include two resonators placed on the sense axis such that one of the resonators is in compression and the other is in tension when acceleration is applied. Temperature changes the resonance frequency in the same direction, whereas the change due to acceleration is opposite in the two resonators [3, 17, 19, 27, 28]. This structure eliminates the temperature effect as a common-mode error, and acceleration impact doubles because of differential reading. The differential design makes the resonant MEMS accelerometers more immune to temperature.

1.2.5 Low Electronic Noise

Resonant MEMS accelerometers have low electronic noise because the output is in the form of frequency [19]. The noise added due to the readout circuit reduces in the resonant MEMS accelerometer designs as the transfer of acceleration to output is

performed by frequency reading compared to capacitive voltage readings [28-30]. This low electronic noise advantage can be enhanced further by implementing a digital control loop and eliminating some analog components that generate electronic noise, which is the main focus of this thesis, i.e., the implementation of a digital control loop for resonant MEMS accelerometers.

1.2.6 Power Supply Fluctuations

Temperature change causes power supply fluctuations, a severe problem with capacitance-based sensors. Resonant MEMS accelerometers are more immune to power supply fluctuations because the output of these sensors is frequency [26].

1.3 Literature Review of Resonant MEMS Accelerometers

The idea of a surface micromachined resonant MEMS accelerometer was first presented in 1997 [8]. Different designs have been published since then to improve the performance of resonant MEMS accelerometers. Most of these research works focus on improving the mechanical design of resonant MEMS accelerometers. Some literature is available on the design of pre-amplifiers stages for these sensors. Analog circuits to sustain oscillations and obtain amplitude stabilization are also in the literature. The output of resonant MEMS accelerometers is in the form of frequency. Therefore, some papers present different frequency reading techniques. This section shows a summary of some distinguished articles to understand the motivation of this study.

Surface micromachined resonant MEMS accelerometers were introduced by [8], where differential oscillating beams obtained first-order temperature compensation. The lever mechanism enhanced the sensor sensitivity, and a double-ended tuning fork (DETF) served as the resonator. They reported a sensitivity of 45Hz/g, but the bias instability was around 12mg. To isolate any interference between the resonators, [3] used two independent proof masses and resonators and reported bias stability of

5.2µg. The work presented by [30] used PLL to track the individual resonant frequency of two resonators, and they used an FPGA-based readout circuit to measure the output frequency and reported a bias instability of 6µg. Research published by [6] reports a bias instability of 0.4µg and a noise floor of 1.2µg/√Hz after eliminating noise in the post-processing stage. They used an integrator-differentiator type pre-amplifier with amplitude control implemented in CMOS and an independent PLL loop for frequency measurement. They discussed a frequency-to-digital (FDC) circuit that converts the output of a PLL to the frequency to interface with a digital system [19]. However, PLL has a drawback, as it requires a startup circuit to start tracking a resonant frequency.

Work done by [7] reports a bias instability of 56ng using a single resonator and a differential sensing scheme, sacrificing the immunity to temperature dependence. In contrast to other popular methods, they used a single resonator between two proof mass structures. The drive voltage is applied 180° out of phase at two ends of the resonating beam. The paper did not provide any information about temperature dependency. However, temperature dependency must be high due to the absence of a differential reading.

It is shown by [31] that by employing a lever mechanism, the sensor sensitivity is increased by 30%, even after lowering the proof mass by 40%. The reduced size of the proof mass adds Brownian noise to the sensor output. Another design by [32] showed a bias instability of 0.16µg owing to an environmentally robust design, which is realized by reducing the number of anchors to isolate the sensing element from environmental effects. This group also showed in another work [33] that bias instability and scale factor can be made more stable by maintaining the temperature of the sensing element by using an on-chip micro-oven. However, the micro-oven significantly increases the power consumption of the system.

A piezoelectric resonant MEMS accelerometer is shown by [29] with a 140dB linear dynamic range. Variation in resonance frequency results from a change in the overlapping area between a proof mass and a resonating beam. Applied acceleration

in the direction of the sense axis causes a shift in the overlap area. Although they achieved a wide dynamic range, their noise values are very high: 850µg/√Hz white noise and 3mg bias instability.

The electrostatic spring softening effect is used in [17] to increase the sensitivity of a sensor by 60%. Additional parallel plate actuators are used to create the softening effect. A similar concept with slight modification has been used by [34] to achieve a sensitivity of 297Hz/g. The sensitivity-enhancement electrode changes the stiffness of the sensing structure under the effect of input acceleration. This change directly changes the resonance frequency of the resonant beam.

Some research on the resonant MEMS accelerometer focuses on the pre-amplifier stage design [6, 16, 19, 35-39]. These types include single-stage resistive trans-impedance amplifiers (TIA), two-stage resistive TIA, capacitive feedback-based TIA, charge-sensing TIA, and integrator-differentiator-based TIA. Noise, gain, stability, and bandwidth are the leading performance parameters that show the efficiency of a pre-amplifier stage. The literature shows that there is always a tradeoff between gain, bandwidth, stability, and noise of a pre-amplifier stage.

The readout circuit of most published work employs an analog control loop for the closed-loop operation of the resonant MEMS accelerometers. Some papers use a network analyzer to acquire the output frequency of the resonators [17, 34, 36], which is not practical to use in an actual application. The work done by [7, 30] uses an external lock-in-amplifier system to read the frequency, which is also not practical to use in an actual application. [19] shows a ΣΔ frequency-to-digital converter (FDC) implemented in a PLL, where the closed loop operation is achieved in the analog domain, while an FPGA measures the digital output of the FDC using comparators. A drawback of this approach is an additional requirement of a startup circuit for the proper operation of the PLL. Another work [40] uses 18-bit analog-to-digital converter (ADC) to convert the oscillator output into the digital domain, where a PLL is implemented in an FPGA to track the frequency and perform processing. However, no feedback from the digital domain goes back to the circuit, which

operates in the analog domain, i.e., the advantage of having a digital control loop is not achieved even though a digital processor is implemented. This type of readout circuit is suitable only for data acquisition in a lab environment.

A study on the digital control loop of a resonant MEMS accelerometer is presented by [41]. This research uses only theory and simulation results, and no implementation of an actual sensor is present in the paper. The actual implementation uses some digital processors, analog-to-digital conversion, and digital-to-analog conversion components. These electronic components have limitations, such as speed and accuracy, that must be considered in the simulation. Otherwise, such a simulation demonstrates only the operation of an ideal system with no representation of actual hardware.

Another work [42] shows a lock-in-amplifier type implementation of digital control of a MEMS resonator, but it is not a complete accelerometer system. The size of this implementation does not make it suitable for real applications. They used an FPGA to implement the digital control loop for the developed sensor. However, their implementation uses power-consuming components focusing only on frequency acquisition. The closed loop operation is achieved using an amplitude tracking method, which is inefficient. The drive signal is in the form of pulses due to the absence of a digital-to-analog converter (DAC). The sensor performance degrades with this type of drive signal compared to a sinusoidal drive signal.

A study by [43] reports a digital control loop-based readout circuit for a resonant MEMS accelerometer, but due to its size, it is not suitable for real applications. The reported bias instability is high (18~40µg), and there is no amplitude stabilization algorithm or a temperature compensation method. The frequency tracking algorithm also consumes more processing power.

Table 1.1 summarizes some of the resonant MEMS accelerometer designs published in the literature. The analog readout circuit-based designs show better performance in terms of bias instability. However, these reported values of bias instability are after post-processing of the data.

Table 1.1: Summary of some major contributions to the resonant MEMS accelerometer field.

Work	Readout type	Bias Instability*	Scale factor	Remarks
[8]	Analog	12mg	45Hz/g	Dual resonators
[3]	Analog	5.2µg	128Hz/g	Dual resonators Dual proof-mass
[30]	Analog	6µg	4.4Hz/g	FPGA-based frequency reading
[6]	Analog, CMOS	0.4µg	280Hz/g	Digital frequency reading
[7]	Analog	56ng	2752Hz/g	Single resonator Temperature-dependent Frequency reading by lock-in-amplifier
[32]	Analog	0.16µg	427Hz/g	Frequency reading by lock-in-amplifier Single anchor design
[43]	Digital	18-40µg	75Hz/g	FPGA based No amplitude control Non-integrated form

*Some papers only report the bias instability values after post-processing the data.

Some studies implement a digital control loop for a frequency-modulated MEMS gyroscope. The drive loop of an FM gyroscope resembles the operation of a resonant MEMS accelerometer. A study used synchronous demodulation for input signals to extract frequency information from MEMS gyroscope output [44]. In some of the studies [45, 46] least mean squares (LMS) adaptive filter is used for frequency demodulation to achieve low complexity and better noise tolerance.

1.4 Motivation

Implementing a digital control loop for resonant MEMS accelerometers has many advantages that can benefit the industry and academia. The following sections show some significant motivational aspects of this thesis study.

1.4.1 Digitalization

The first motivation for this study is digitizing the resonant MEMS accelerometer. This type of sensor has frequency as its output and requires a frequency reading method to measure its output frequency. Therefore, a processor is already present in most designs for frequency measurement, even in analog implementations. The same processor can be used for frequency measurement and sustaining oscillations.

1.4.2 Reduction in Analog Electronics

Analog electronics add noise and power consumption to any readout circuit and requires complex circuitry to achieve high performance. If some of the logic implemented in the analog domain transfers to the digital domain, noise and power consumption will reduce significantly. In an analog readout circuit of a resonant MEMS accelerometer, amplitude stabilization and oscillation sustaining are performed by analog modules. These functionalities transfer to the digital domain in a digital control loop implementation resulting in a reduction of analog components in the readout circuit. Some of the readout circuit schemes in the literature use a PLL for frequency tracking, which requires a startup circuit to begin the oscillations. The PLL implemented in the digital domain does not require an external startup circuit. Therefore, a digital control loop implementation can reduce analog electronics in a readout circuit, which also results in the reduction of electronic noise.

1.4.3 Configurable Parameters

The digital control loop implementation allows configuring some sensor parameters, which is impossible in an analog circuit without making changes in the hardware. For example, the time constant of filters implemented in software can be changed by modifying a line of code in contrast to changing capacitance or resistance in an analog circuit. Similarly, the gain is another parameter that can be controlled easily

with software without modifying anything in the hardware. This reconfigurability feature is critical in a design process and also has applications in a final product.

1.4.4 Testability

Testability is another advantage of a digital control-based readout circuit. Different functional tests can monitor the health of a sensor and detect different malfunctions present in a sensor. For example, the functional test for the frequency tracking capability of each resonator can show if the individual resonator is oscillating correctly.

1.4.5 Debugging and Data Acquisition

Another motivation for transferring the logic to the digital domain is easy debugging and data acquisition, which is very beneficial in the design phase or understanding the behavior of a sensor because it gives access to sensor data at different points of operation. Input data, demodulated data, input to the PI controller, PI controller output, and frequency of resonators can be monitored and analyzed. This flexibility makes the debugging process simple, highlighting the exact point of a problem.

1.4.6 Multiple Algorithms

The digital control-based readout circuit is capable of performing multiple functionalities. Maintaining oscillations is one of the functions that is achievable with a digital control loop. Other functionalities, such as health monitoring, frequency sweeping, and scale measurements, are also implemented in the digital domain. Implementation of multiple algorithms enhances the performance of a sensor. For example, a PI controller for amplitude stabilization, PLL for frequency tracking, and temperature compensation can run simultaneously to achieve better performance. With each algorithm, the performance of a sensor improves without

adding additional circuit components. However, the number and complexity of the algorithms implemented in a digital processor are limited by its speed and capability.

1.4.7 Iterative Design Process

Previous sections show that digital design allows changing parameters or implementing multiple algorithms simultaneously. Another essential feature is its capability to accommodate iteration in the design process. Any algorithm implemented in the digital domain can be replaced with an entirely different algorithm without making any changes to the hardware. For example, sine wave generation can be achieved by the trigonometric functions available in a processor, a CORDIC module available in a processor, or with the help of a lookup table.

1.4.8 Direct Access to Sensor Parameters

The last motivation is inspired by the author's expertise in the development of embedded systems. Commercially available digital accelerometers do not give access to the sensor parameters. Their digital interface mainly performs frequency counting and signal conditioning only. In some applications, the bandwidth is more important than the noise performance and vice versa. With a digital control loop implemented and a processor controlling the sensor directly, it is possible to change different parameters according to application requirements. This feature makes a sensor useful for many applications. Another critical parameter that can be modified is the sensitivity of a sensor. The electrostatic softening effect can change the sensitivity of a resonator. The biasing voltage applied to the sensitivity-enhancing electrodes determines the sensitivity of a resonator.

1.5 Aims

The published literature shows no compact system implementing a digital control loop for a resonant MEMS accelerometer. The first objective of this thesis is to design and develop a compact readout circuit that implements a digital control loop using readily available off-the-shelf electronic components.

In the digital domain, multiple algorithms can run in parallel without making changes to the hardware, in contrast to analog circuits, where complexity increases with sensor performance [47]. The second objective is to implement multiple algorithms in the digital domain to improve performance and increase the testability of the sensor. The performance improves with algorithms such as temperature compensation, and the testability improves with different self-tests and functional tests.

The third motivation of the study is to implement a technique that requires fewer processing resources. This feature allows the use low powered processors and accommodates other performance-enhancing algorithms.

1.6 Thesis Outline

Chapter 2 of this thesis presents the working principle of a general resonant MEMS accelerometer. The chapter also shows different readout circuit topologies used with resonant MEMS accelerometers. It also mentions different techniques available in the literature for amplitude and frequency demodulation.

Chapter 3 gives information about the available sensors for this study. It also provides results of the sensor characterization using a dynamic signal analyzer (DSA) and a lock-in-amplifier.

Chapter 4 focuses on implementing digital control for a resonant MEMS accelerometer. It explains several components of a typical readout circuit of a resonant MEMS accelerometer. This chapter provides a noise analysis for the circuit

used for the digital control loop. The chapter also provides a Simulink model for the implemented method.

Chapter 5 presents results obtained from the microcontroller-based digital control PCB. The chapter discusses the results to understand the effect of different parameters on sensor performance.

Chapter 7 concludes this thesis and suggests possible future works related to the digital control loop-based readout circuit of a resonant MEMS accelerometer.

CHAPTER 2

RESONATING MEMS ACCELEROMETER READOUT METHODS

This chapter presents various critical components of a typical resonant MEMS accelerometer and reviews some amplitude and frequency demodulation techniques that can be implemented in the digital domain. Section 2.1 explains the operating principle of a typical differential resonant MEMS accelerometer. Section 2.2 shows the major components of a typical readout circuit: (i) the pre-amplifier stage, (ii) the oscillation sustaining part, and (iii) the frequency reading part. Section 2.3 details different pre-amplifier topologies available in the literature and focuses on their gain, bandwidth, stability, and noise performance. Section 2.4 briefly explains different schemes used for oscillation sustaining and highlights the importance of a stable output amplitude of a resonant MEMS accelerometer. Section 2.5 summarizes a few popular frequency demodulation techniques that are present in the literature. Similarly, Section 2.6 presents the amplitude demodulation techniques that can be implemented in the digital domain. Finally, Section 2.7 summarizes the essential points of this chapter.

2.1 Theory of Operation

This section explains the theory of the most generic resonant MEMS accelerometer, which comprises a proof mass, two resonating beams (typically DETF), and a lever mechanism [8]. Figure 2.1 shows a conceptual schematic of a resonant MEMS accelerometer. The proof mass is the sensing element of a resonant MEMS accelerometer, which is flexible in the direction of the sensitive axis and rigid in all other directions. The proof mass connects to vibrating beams via a lever mechanism. The lever is a unique structure that transfers amplified force from the proof mass to

the beams. If the beams are connected directly to a proof mass, they experience less force for an input acceleration as compared to the beams connected via a lever mechanism. An anchor is at one end of the beams, and a proof mass at the other. The direction of the vibrating beams is such that they only experience axial loading under the effect of acceleration applied to the sensitive axis. Also, both resonating beams are placed such that the direction of the applied stress is opposite to each other, i.e. when one resonator beam is in tension, the second is in compressive stress. Drive electrodes are at one end of the resonators, and sense electrodes are at the other. An electrode is also present for applying any desired voltage to the proof mass.

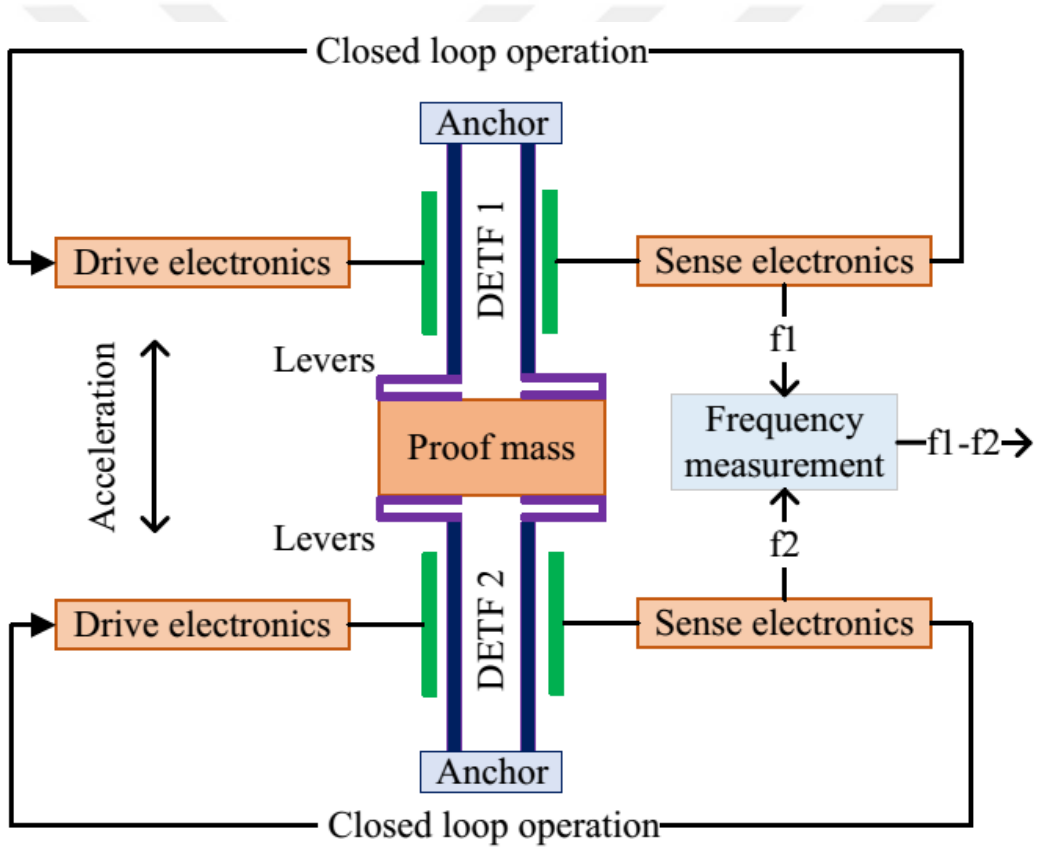

Figure 2.1: A schematic of a generic differential resonant MEMS accelerometer, showing its main components and interfacing with a typical readout circuit.

The function of the drive electrodes is to oscillate both resonators, whereas the sense electrodes sense the frequency of the oscillators at the other end. A feedback system sustains the oscillations, and the resonator oscillates at its resonance frequency. There are different methods to operate the resonators in a closed loop. Equation 2.1 shows the mathematical model of a single resonator expressed by the second-order differential equation using a mass-spring-damper model.

$$f_D(t) = m\,\frac{d^2x}{dt^2} + b\,\frac{dx}{dt} + k\,x(t) \qquad 2.1$$

Where f_D is the force acting on the proof mass as a result of input acceleration, m is the mass of the structure, including beams, and proof mass, $x(t)$ is the displacement of the beam, b is the damping factor, and k is the spring constant of the beam. The Laplace transform of Equation 2.1 gives the frequency domain representation as follows:

$$F_D(s) = m\,s^2X(s) + b\,sX(s) + k\,X(s) \qquad 2.2$$

The relation between applied force and resulting displacement can be represented by Equation 2.3 as follows:

$$\frac{X(s)}{F_D(s)} = \frac{1}{m\left(s^2 + \frac{\omega_r}{Q}\,s + {\omega_r}^2\right)} \qquad 2.3$$

Where w_r is the resonator's resonance frequency, and Q is the resonator's quality factor. The quality factor and the resonance frequency in terms of mass, damping factor, and spring constant are defined as follows:

$$\omega_r = \sqrt{\frac{k}{m}} \qquad 2.4$$

$$Q = \frac{\sqrt{k\,m}}{b} \qquad 2.5$$

At the resonance frequency, Equation 2.3 can be re-written as follows:

$$\frac{X\,(j\omega)}{F\,(j\omega)} = \frac{1}{m\,(\,(j\omega)^2 + \,\omega\frac{j\omega}{Q} + \,\omega^2)} \qquad 2.6$$

$$\frac{X\,(j\omega)}{F\,(j\omega)} = \frac{1}{m\,(\,-\omega^2 + \frac{j\omega^2}{Q} + \,\omega^2)} \qquad 2.7$$

$$\frac{X\,(j\omega)}{F\,(j\omega)} = \frac{Q}{j\,m\,\omega^2} \qquad 2.8$$

The resonance frequency is a function of stress in the resonator. Therefore, when the proof mass displaces due to applied acceleration in the direction of the sense axis, it results in tension in one of the resonators and compression in the other. The resonance frequency increases in the resonator with tension and decreases in the resonator with compression. The feedback loop follows the resonance frequency of each resonator. The difference between the frequencies of the two resonators gives information about the input acceleration.

Other factors also affect the resonance frequency of a resonator. A dominant factor is temperature, which results in shifting the natural frequency of the resonators in the same direction resulting in a common mode error. A differential reading eliminates this error, and only the effect of the applied acceleration remains. Figure 2.2 shows a conceptual diagram of how differential reading gives information about input acceleration.

$$f1 = resonance\ frequency\ of\ resonator\ 1$$

$$f2 = resonance\ frequency\ of\ resonator\ 2$$

$$f_0 = natural\ resonance\ frequency\ of\ resonator\ 1\ \&\ 2$$

$$\Delta f_T = Change\ in\ resonance\ frequency\ due\ to\ temperature\ change$$

$$\Delta f_a = Change\ in\ resonance\ frequency\ due\ to\ input\ acceleration$$

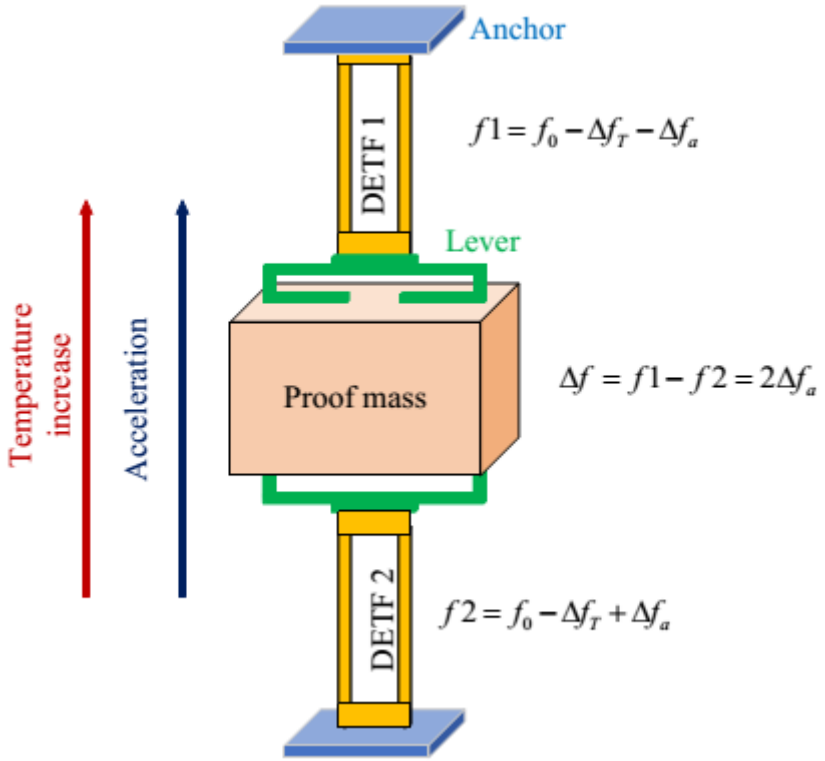

Figure 2.2: The conceptual diagram of the differential reading of a resonating MEMS accelerometer under applied acceleration and varying temperature shows how a differential reading cancels the first-order temperature effect.

The temperature cancellation effect due to differential reading has limitations because only first-order temperature effects cancel out. The scale factor of both the resonators has to be identical to have a similar temperature effect. Resonators with different sensitivity values change differently when temperature changes and the differential value remains temperature-dependent. However, this dependency is much lower than a single resonator's dependency. This temperature dependency can be compensated using simple temperature compensation [5]. These algorithms can be applied efficiently if the readout scheme is implemented with a digital control loop with the resonant MEMS accelerometers, as demonstrated in this thesis.

2.2 Blocks of a readout circuit

Figure 2.3 shows a conceptual block diagram of different components of a typical analog readout circuit for resonant MEMS accelerometers. The first part of the circuit has two components: a sensor and a pre-amplifier stage. The sensor is a resonant MEMS accelerometer with motional current output, and the pre-amplifier stage amplifies this current and converts it into voltage form.

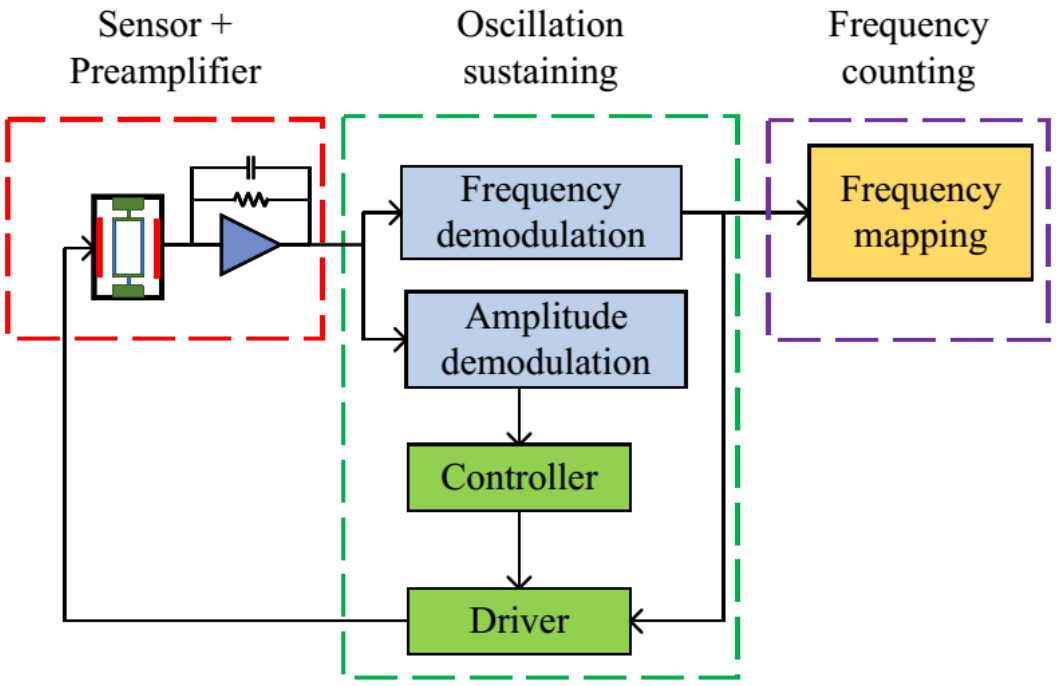

Figure 2.3: A conceptual diagram of a typical analog readout circuit for resonating MEMS accelerometers, showing this circuit's three main components: pre-amplifier, oscillation sustaining, and frequency counting.

The next major part of a typical readout circuit is its ability to sustain oscillations. This part of the circuit sustains oscillations to operate the resonators at their resonance frequency. This circuitry ensures that the correct phase and amplitude reach the drive electrodes to maintain oscillations. Amplitude demodulation extracts amplitude information and keeps the resonator displacement in the linear region.

Typically a controller is present in this circuit to maintain the sensor output at a set point value and ensures that the resonators oscillate without going into a non-linear region. This part of the circuit also performs frequency extraction. The circuit uses this frequency and amplitude information to generate the drive signal to close the loop for resonators. Therefore, amplitude and frequency extraction are essential functionalities of the oscillation-sustaining circuit for maintaining stable output amplitude and supplying the correct phase to the drive electrodes of the sensor.

The third main component of the readout circuit for resonant MEMS accelerometers is frequency counting and mapping. This component is not directly part of the sensor operation but is critical for data analysis. This part converts the demodulated frequency to a digital form that can be analyzed and mapped to input acceleration.

2.3 Types of pre-amplifier stages

The output of a resonant MEMS accelerometer is a weak motional current converted to voltage using a pre-amplifier stage. Equation 2.9 gives the capacitance of the sense electrode:

$$C_{sense}(t) = C_{static} + 2 * n_e * \varepsilon * h * \frac{x_s(t)}{g} \qquad 2.9$$

C_{sense} is the capacitance of the sense electrodes, C_{static} is the capacitance of the sense electrodes under static conditions, n_e is the number of the sense electrode, h is the height of the sense electrodes, g is the gap between electrodes, and x_s is the displacement of the sense electrodes. Equation 2.10 gives the relation for the generated motional current.

$$I_s(t) = V_{pm} * \frac{C_{static}}{L_s} * \frac{dx_s}{dt} \qquad 2.10$$

Here V_{pm} denotes the proof mass voltage, and L_s is the length of sense electrodes. This equation shows that the motional current generated by resonant MEMS accelerometers is directly proportional to the proof mass voltage. A higher proof

mass voltage gives a higher motional current. This current goes to a pre-amplifier that converts it to a voltage signal.

There are three features of a sound pre-amplifier stage. First is a significant gain to sustain oscillation [36]. The loop gain of a resonant MEMS accelerometer must be greater than one to sustain oscillations. The second desirable feature in a pre-amplifier is wide bandwidth. This feature is essential for high-frequency applications to avoid phase shifts. As a general rule of thumb, the bandwidth of a pre-amplifier stage should be ten times larger than the resonance frequency of a sensor [21]. Low input referred noise is the third and most critical feature [48]. The pre-amplifier is the first stage of amplification and the most dominant source of noise in the system. Noise added by any later amplifier stage is not as important as the first stage. Therefore, a pre-amplifier scheme with low input referred noise is suitable for high noise performance. The input referred noise of the pre-amplifier stage should be, ideally, less than the Brownian noise of the resonator. Some major topologies of pre-amplifier stages available in the literature are discussed here.

2.3.1 Single-stage resistive trans-impedance amplifier (TIA)

Figure 2.4 shows a simplified schematic of a single-stage resistive trans-impedance amplifier [15, 35]. C_{in} is the parasitic capacitance seen at the inverting node of the amplifier, R_f is the feedback resistance, and C_c is the compensation capacitance for stability. Equation 2.11 gives the trans-impedance of this circuit.

$$H(s) = \frac{-R_f}{R_f\, C_c\, s\, + 1} \qquad 2.11$$

The values of feedback resistance and compensation capacitor determine the type of TIA. The amplifier becomes resistive if $R_f C_c\, s \ll 1$. This condition reduces the transfer function equal to the feedback resistance. The gain becomes independent of the capacitance and the frequency. The compensation capacitor improves the stability but limits the bandwidth of the amplifier. The relation of bandwidth is given by Equation 2.12:

$$Bandwidth = \frac{1}{2\,\pi\,R_f\,C_c} \qquad 2.12$$

The bandwidth increases with a decrease in the feedback resistance and the compensation capacitor. Therefore, a tradeoff exists between the bandwidth and the stability of the pre-amplifier stage.

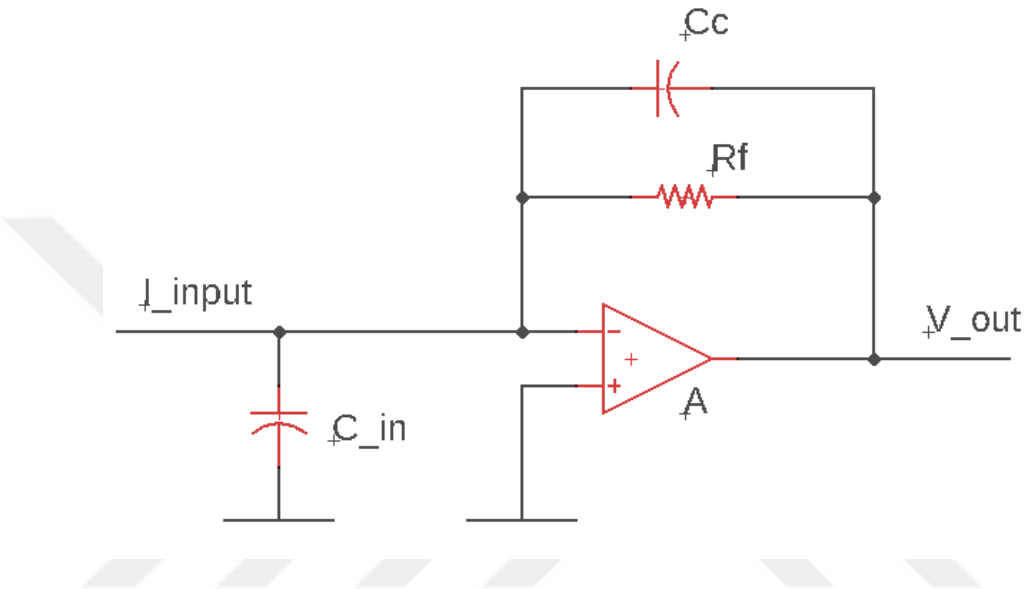

Figure 2.4: The single-stage resistive trans-impedance amplifier (TIA). The values of the feedback resistor and compensation capacitor determine this amplifier scheme's bandwidth, gain, and noise.

The pre-amplifier is the first amplification stage, and it is essential to have a small value of input-referred noise. Equation 2.13 gives the relation for the input-referred noise of the single-stage resistive pre-amplifier.

$$I_{in}{}^2 = \frac{4\,k\,T}{R_f} + \left\{ V_n{}^2 * \left[\frac{1 + s\,R_f\,(C_{in} + C_c)}{R_f} \right]^2 \right\} \qquad 2.13$$

Where I_{in} is the input-referred current noise, $V_n{}^2$ is the amplifier's voltage noise, and C_{in} is the parasitic input capacitance. This equation shows that the input-referred noise is inversely proportional to the feedback resistance. There is a tradeoff between noise and bandwidth of the amplifier. Increasing feedback resistance reduces the

input-referred noise and limits the amplifier's bandwidth. The first term in this equation is the dominant noise term at low frequencies, and the second term dominates the noise at higher frequencies. Parasitic capacitance seen at the input of the amplifier increases the noise. Another tradeoff exists between bandwidth, stability, and noise of the pre-amplifier due to the value of the compensation capacitance. The bandwidth decreases, and the noise increases with an increase in the compensation capacitance. The stability, however, increases with an increase in the compensation capacitor value.

2.3.2 Two-stage resistive TIA

A significant value of feedback resistance increases the gain of a TIA but limits the amplifier's bandwidth. A two-stage resistive TIA approach increases the gain without sacrificing the amplifier's bandwidth [36]. Figure 2.5 gives a schematic of a two-stage resistive TIA. Equation 2.14 gives the trans-impedance of the two-stage resistive pre-amplifier as follows:

$$R_{eq} = R_f * (1 + \frac{R_2}{R_1}) \qquad 2.14$$

Where R_1 and R_2 are the gain-setting resistors of the second stage, and R_f is the feedback resistance of the first stage. This scheme allows a large trans-impedance by using a small feedback resistance value. The smaller value of the feedback resistance increases the bandwidth of the pre-amplifier. Equation 2.15 gives the input-referred noise of the two-stage resistive feedback pre-amplifier stage.

$$I_{in}{}^2 = \left(1 + \frac{R_2}{R_1}\right)\frac{4\,k\,T}{R_{eq}} + \left\{ V_n{}^2 * \left[\frac{1 + s\,R_f\,(C_{in} + C_c)}{R_f}\right]^2 \right\} \qquad 2.15$$

This configuration has the benefit of improved gain and bandwidth, but noise performance degrades when compared to single-stage resistive TIA. The addition of resistors increases the input-referred noise. The frequency-dependent term of the two-stage resistive pre-amplifier term is similar to the single-stage resistive pre-amplifier, but the first term differs. The second gain stage amplifies the constant

noise of this pre-amplifier stage and any DC offset present in the signal. This feature can limit the dynamic range of the amplifier [36].

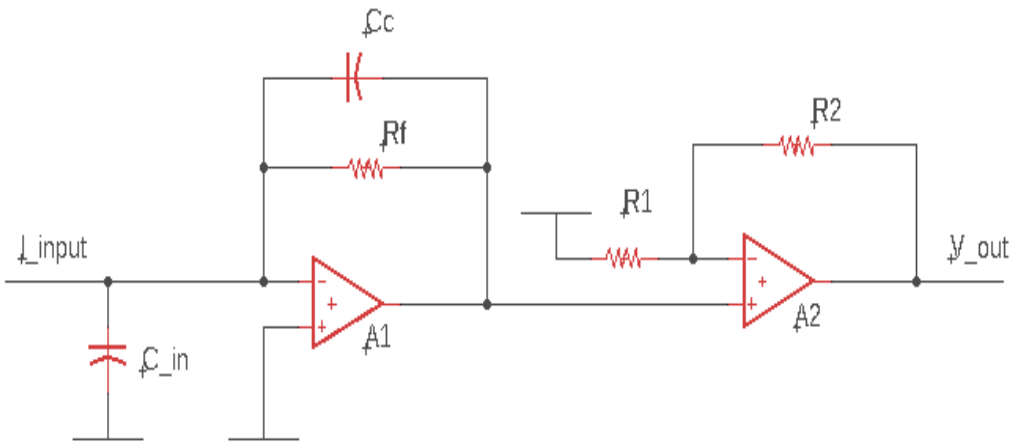

Figure 2.5: A schematic of a two-stage trans-impedance amplifier. The second gain stage increases the gain, but noise performance is degraded.

2.3.3 Charge sensing amplifier (CSA)

Figure 2.6 give a schematic of a charge-sensing trans-impedance amplifier. The schematic is the same as a single resistive TIA. The difference is the value of the feedback capacitor and the biasing resistor. The amplifier acts as capacitive if $R_b C_f \, s \gg 1$. The value of R_b is selected to be very large. These values allow a considerable gain required to amplify the weak sensor current. The feedback capacitance and the biasing resistor govern the bandwidth of this pre-amplifier.

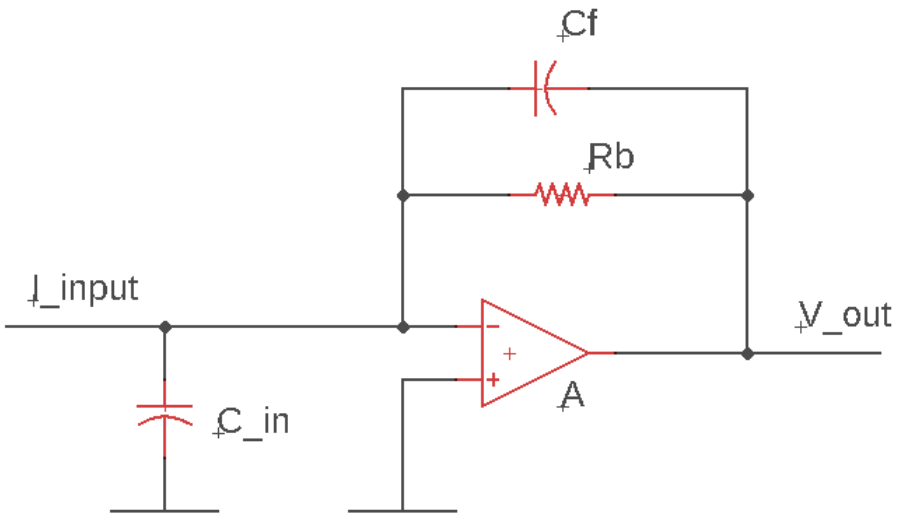

Figure 2.6: A schematic of a charge-sensing TIA, which provides a high gain and inherent stability.

The noise equation of the charge-sensing preamplifier is similar to that of the single-stage resistive TIA. Equation 2.16 gives the relation for input-referred noise:

$$I_{in}{}^2 = \frac{4\,k\,T}{R_b} + \left\{ V_n{}^2 * \left[\frac{1 + s\,R_b\,(C_{in} + C_f)}{R_b} \right]^2 \right\} \qquad 2.16$$

However, the noise performance is better than single-stage resistive TIA because the value of biasing resistor is very high. This pre-amplifier is more stable than the resistive type TIA. The parasitic capacitance at the amplifier input degrades the noise performance but does not affect the stability. The CSA acts as an integrator, and the output is 90° phase lagged from the input. Therefore, a phase shift is required to meet the self-oscillating condition [16, 37].

2.3.4 T-Network resistive TIA

Another approach to increase the gain of the amplifier without sacrificing the bandwidth is to use T-network resistors in the amplifier [38]. Figure 2.7 shows a

schematic of a T-network resistive TIA. Equation 2.17 gives the gain with the resistive network scheme:

$$R_{eq} = R_f * \left(1 + \frac{R_2}{R_1}\right) + R_2 \qquad 2.17$$

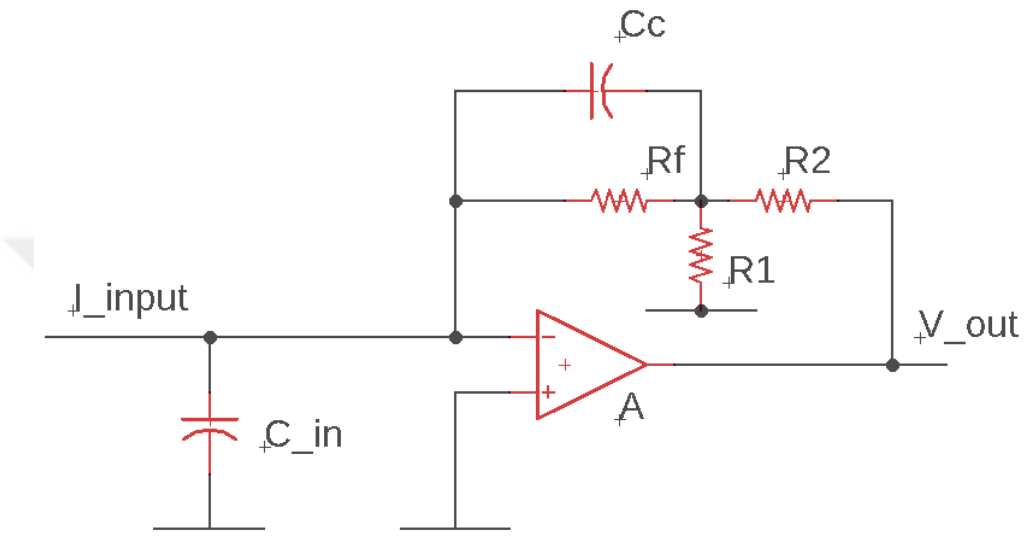

Figure 2.7: A schematic of a T-network resistive TIA.

The bandwidth is independent of the resistors R1 and R2. The noise performance is similar to two-stage resistive TIA as the number of resistors is the same. The size is smaller than the two-stage resistive TIA because of a single opamp. In summary, the T-network resistor performs similarly to a two-stage resistive pre-amplifier in terms of noise, bandwidth, and gain but is smaller. The amplification of the DC offset is also present in this scheme of the pre-amplifier.

2.3.5 Capacitive feedback pre-amplifier

Another approach to reducing the noise of an amplifier is to use a capacitive feedback pre-amplifier [26, 39]. The capacitive feedback pre-amplifier is a shunt-series amplifier with current as its output, which is converted to a voltage using another

current-to-voltage conversion stage. Equation 2.18 shows the input-referred noise of the capacitive feedback TIA.

$$I_{in}{}^2 = \frac{4\,k\,T}{R_f\,\left(1+\frac{C_2}{C_1}\right)^2} + \left\{ V_n{}^2 \ * \ [s\,(C_{in} + \ C_1)]^2 \right\} \qquad 2.18$$

Where R_f is the output resistance of the output amplifier that converts the current to the voltage form, and C_1 and C_2 are the feedback network capacitances. The noise from the resistor reduces significantly, with a factor controllable by the values of the feedback capacitors. The noise problem is solved with this method, but the circuit lacks DC feedback, and a biasing circuit is required for the practical implementation.

2.3.6 Integrator-Differentiator based TIA

Figure 2.8 shows another implementation method of the pre-amplifier stage presented by [16]. The first opamp acts as an integrator, and the second opamp acts as a differentiator. The second opamp compensates for the phase lag caused by the first stage. Equation 2.19 gives the overall transfer relation:

$$H(s) = \frac{R_b\,R_f\,C_2\,s}{(R_b\,C_1\,s+1) * (R_f\,C_c\,s+1)} \qquad 2.19$$

The transfer function is directly proportional to the velocity, which easily satisfies the oscillation condition. The topology acts as a bandpass, with the first opamp defining the lower cut-off frequency and the second opamp defining the upper cut-off frequency. Equation 2.20 gives the trans-impedance:

$$R_{eq} = \ R_f * \frac{C_2}{C_1} \qquad 2.20$$

The equation shows that the gain of this amplifier sets by setting the value of capacitors C_1 and C_2. There are four primary noise sources at the input in this configuration. The current noise due to the biasing resistor R_b appears directly at the input, and the current noise due to the feedback resistor R_f appears at the input after

division by the factor of C_2/C_1. The other two noise sources are the voltage noise of the two amplifiers.

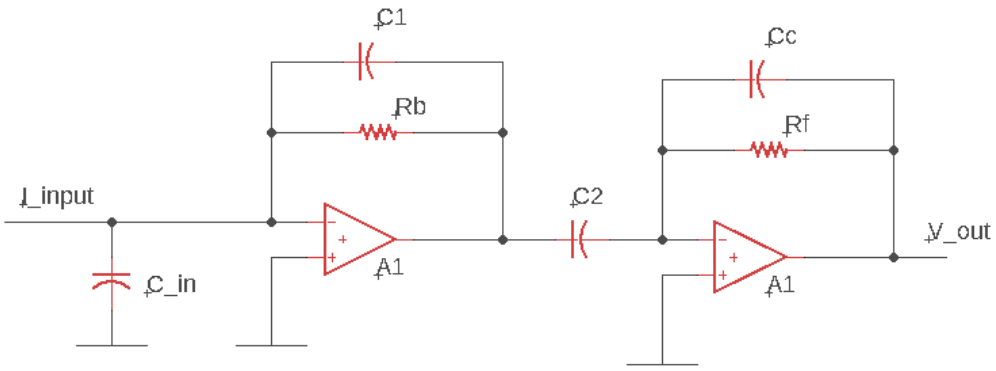

Figure 2.8: A schematic of an integrator-differentiator-based TIA. This scheme provides high gain and noise performance.

Equation 2.21 gives the relation of the input-referred noise of the integrator-differentiator pre-amplifier scheme [19].

$$I_{in}{}^2 = I_{nb}{}^2 + I_{in}{}^2\left(\frac{C_1}{C_2}\right)^2 + V_{n1}{}^2\,[s\,(C_{in} + C_1)]^2 + V_{n2}{}^2\,[s\,C_1]^2 \qquad 2.21$$

Where I_{nb} is the current noise of the biasing resistor, I_{nf} is the current noise of the feedback resistor, V_{n1} is the voltage noise of the first opamp, and V_{n2} is the voltage noise of the second opamp. The bandwidth and the trans-impedance are not dependent on each other. The noise performance is excellent compared to other topologies. The values of capacitors C_2/C_1 attenuate noise from the second stage. The transfer function is directly proportional to the velocity, and the scheme is inherently stable. The integrator-differentiator-based TIA can also be implemented in a discrete-time configuration [49]. The choice between continuous or discrete time amplifiers depends on the interfacing circuit.

2.3.7 Comparison of pre-amplifier topologies

Table 2.1 shows a comparison of different pre-amplifier stage schemes present in the literature. The comparison is based on the amplifier schemes' gain, bandwidth, stability, and noise performance. The different schemes are compared to the first scheme, i.e., the single-stage resistive pre-amplifier.

Table 2.1: Comparison of different pre-amplifier stage topologies for a resonant MEMS accelerometer

Scheme	Pros	Cons
Single-Stage Resistive TIA	*This amplifier scheme will be used as a reference for comparison*	There is a trade-off between gain, bandwidth, and noise performance
Two-stage resistive TIA	Better gain and bandwidth	Degraded noise performance and larger footprint DC noise amplfication.
Charge Sensing TIA	Better gain, bandwidth, and noise performance	90° phase shift in the output
Resistive T-Network TIA	Better gain and bandwidth	DC noise amplification Degraded noise performance
Capacitive feedback TIA	Better gain and noise performance	No DC biasing Additional amplification stage required
Integrator-Differentiator TIA	Better gain, noise, and bandwidth Output suitable for oscillation	Larger footprint

2.4 Oscillation sustaining topologies

The oscillation sustaining stage of an analog readout circuit of a resonant MEMS accelerometer performs amplitude and frequency demodulation and provides feedback to the drive electrode to sustain the oscillations of the resonators. The resonators oscillate when they satisfy the Barkhausen stability criterion, and different

approaches are used to self-oscillate the circuit depending on the type of pre-amplifier stage.

In the digital implementation of the control loop, the functionalities of this stage transfer to the digital domain. The functionalities such as frequency demodulation, amplitude demodulation, amplitude stabilization, and frequency tracking transfer to the digital environment.

This section briefly explains some major topologies from the literature used to sustain the oscillations of the resonators of a resonant MEMS accelerometer. However, firstly it is crucial to explain the effect of resonator displacement on the resonance frequency because it affects the resonance frequency of a resonator. Equation 2.22 shows the dependence of the resonance frequency of a resonator on its displacement:

$$f = f_0 \left(1 + \frac{3}{4}\frac{K_3}{K_1} {x_s}^2\right) \qquad 2.22$$

$$f = effective\ resonance\ frequency$$

$$f_0 = ideal\ resonance\ frequency$$

$$K_1 = spring\ constant\ of\ resonator$$

$$K_3 = non - linearity\ stiffness\ constant$$

$$x_s = displacement\ of\ resonator\ beam$$

The equation shows that the resonance frequency of a resonant MEMS accelerometer shifts with a change in the displacement of the beam. Therefore, it is imperative to keep this displacement constant to obtain a stable resonance frequency.

All the oscillation circuit schemes of the resonant MEMS accelerometers ensure that the resonator operation is in a linear region by maintaining the displacement of the resonators at a fixed set point value. The first topology is shown by [8, 50], where the TIA gain is tunable and set by the difference between output amplitude and a set-point reference voltage. This method produces a stable output amplitude, but the

beam displacement fluctuates. The reason is that the variable gain controller only monitors the amplitude coming out of TIA and stabilizes that amplitude by changing the TIA gain. The excitation signal of the resonator is not changed, and the resonator can go into the non-linear region. Another important topology is presented by [49], in which a variable gain amplifier (VGA) controls the amplitude of the drive signal. The main difference from the first topology is that the VGA controls the drive signal, not the TIA output. The output of TIA is amplitude demodulated and compared with a set point voltage. The drive signal amplitude is calculated based on the difference between the set point voltage and TIA output amplitude.

Another topology for oscillation-sustaining circuits is shown by [30], where the amplitude is not controlled based on an external set point voltage, but a PLL is used to extract frequency information. An automatic gain control (AGC) is used to generate the drive signal based on demodulated frequency and amplitude. The absence of an external reference is a drawback of this topology.

Some other schemes in the literature are also used to sustain the oscillations of the resonators of a resonant MEMS accelerometer, but they differ slightly from the topologies mentioned above. However, the main objective is the same in all the methods, i.e., to keep the output amplitude of the sensor stable and oscillate the resonator at its resonance frequency.

2.5 Frequency Demodulation

Frequency demodulation is one of the main functions performed in a readout circuit of a resonant MEMS accelerometer that uses the frequency information for the generation of the drive signals. The frequency information is also used for mapping the input acceleration, i.e., calculating the input acceleration based on the measured resonance frequency. This section briefly discusses some frequency demodulation techniques implemented in the digital domain.

2.5.1 Direct frequency counting

Direct frequency counting is the simplest method used to find the frequency of an input signal. A sinusoidal signal oscillates around zero, and the number of zero crossings can be counted in a known period. This period divided by the number of zero-crossings, gives the input signal frequency. Figure 2.9 shows a simple algorithm for the direct frequency counting method. This method is straightforward but only suitable for low frequencies because of low resolution.

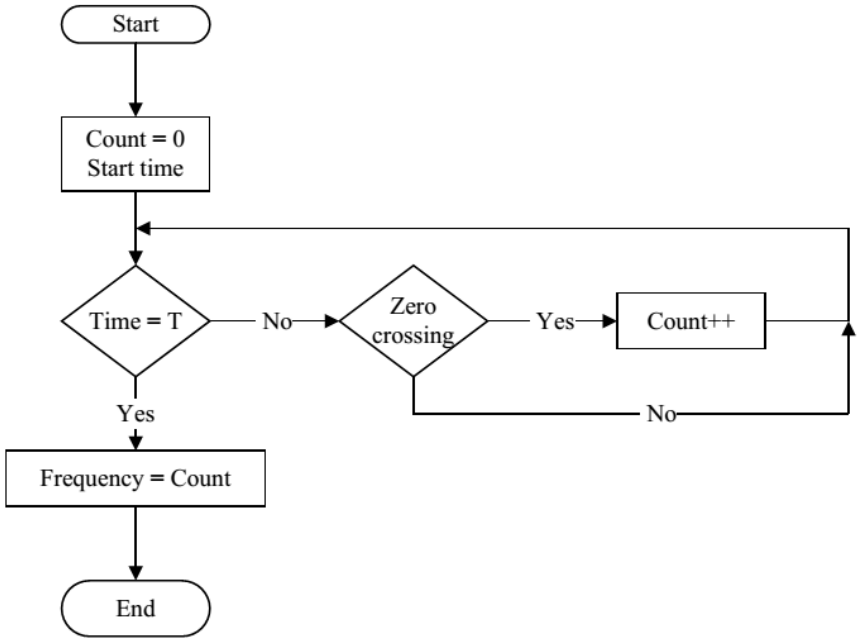

Figure 2.9: The flow diagram of the algorithm used for the direct frequency counting method. This method is simple but has low resolution.

2.5.2 Interval-based frequency counting

The interval-based frequency counting method measures the period of one cycle and finds the frequency by taking the inverse of that time. The resolution of this method can improve by taking the average of several samples. Figure 2.10 shows a

conceptual diagram for this technique. This method is simple to implement and has better resolution than the direct frequency counting method. The drawback of this technique is that only a very high sampling rate can provide high resolution, and therefore not suitable for high-frequency applications. Also, this technique requires a comparator design for time period measurement, resulting in a square wave that loses the amplitude information. This technique is also unsuitable for an analog-to-digital converter (ADC).

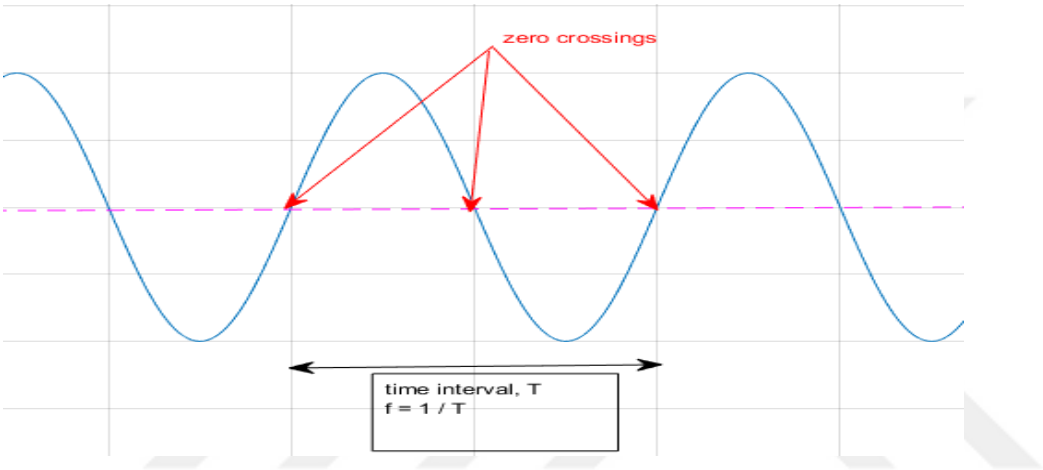

Figure 2.10: The interval-based frequency counting method measures the time between zero crossings. The resolution of this method improves by using a higher sampling rate and taking an average of the measured values.

2.5.3 PLL-based frequency counting

A phase-locked loop (PLL) approach is commonly used in many applications to track the input frequency, and it can be implemented in the analog and digital domains. A typical PLL has three main parts: (i) a phase detector, (ii) a loop filter, (iii) and a voltage control oscillator (VCO). The phase detector determines the phase difference between the input signal and a reference signal, and the VCO generates a reference signal based on the phase difference between the input and the reference signal. The loop filter takes the average of the phase difference and generates a voltage signal

for the VCO, which increases or decreases the reference frequency until it matches the input frequency.

The same concept is also present in the digital domain implementation of a PLL, where a digitally-controlled oscillator (DCO) replaces the VCO to generate the reference frequency. The phase between the input and the reference signal is calculated in the digital domain, and the loop filter is also implemented in the digital environment. The performance of the digital PLL depends upon factors such as phase detection technique, loop filter, and signal generator method. Figure 2.11 shows a conceptual diagram of the different components of an analog and a digital PLL. In both cases, phase detection is performed between an input and a reference signal. The loop filter is implemented in the analog and digital domains, and its output drives the oscillator. The signal from the loop filter is a voltage signal in an analog implementation, whereas it is a control word in a digital PLL.

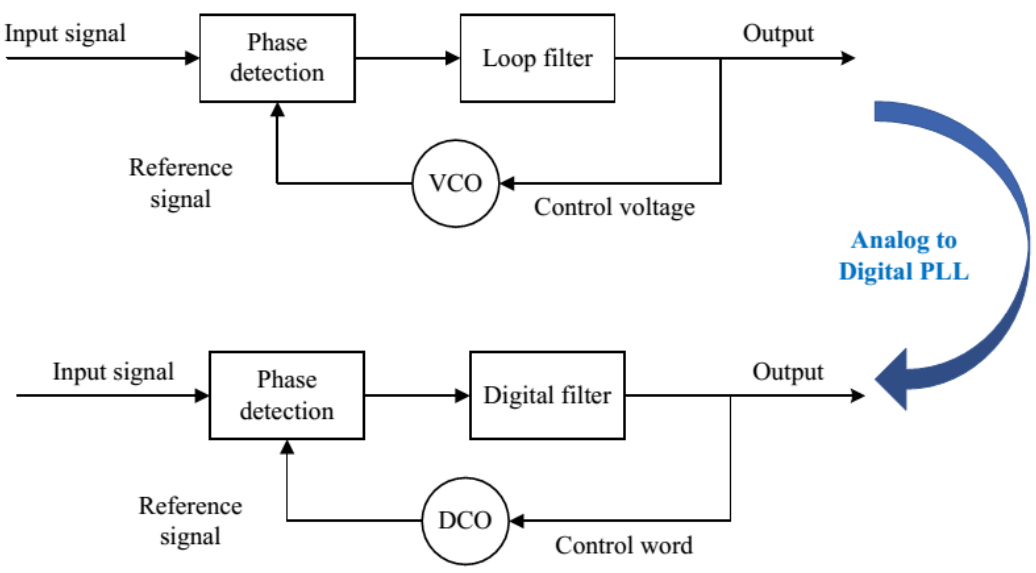

Figure 2.11: A conceptual diagram of an analog and a digital PLL. The functional blocks are the same in the analog and digital domains.

The digital implementation of a PLL is immune to temperature and power supply variations when compared to the analog PLL. However, it consumes much

processing power and works in a narrow bandwidth for high noise performance. The analog implementation has another drawback: it requires a startup circuit to drive the oscillator near its resonance frequency. The PLL can track the resonance frequency after the oscillator initially starts oscillating near its resonance frequency.

2.5.4 Synchronous demodulation

Synchronous demodulation can also extract the frequency information from an input signal. The process starts by multiplying the input signal by a reference signal and then passing the product through a low-pass filter to remove the high-frequency components. The filter output is zero if the phase difference between the input and the reference signal is 90° and the frequencies are identical. A proportional-integral (PI) controller is used to track the outcome of the low-pass filter, and this controller generates a control signal to update the reference signal until both frequencies are 90° phase-shifted. Figure 2.12 shows a simplified schematic of the synchronous demodulation technique.

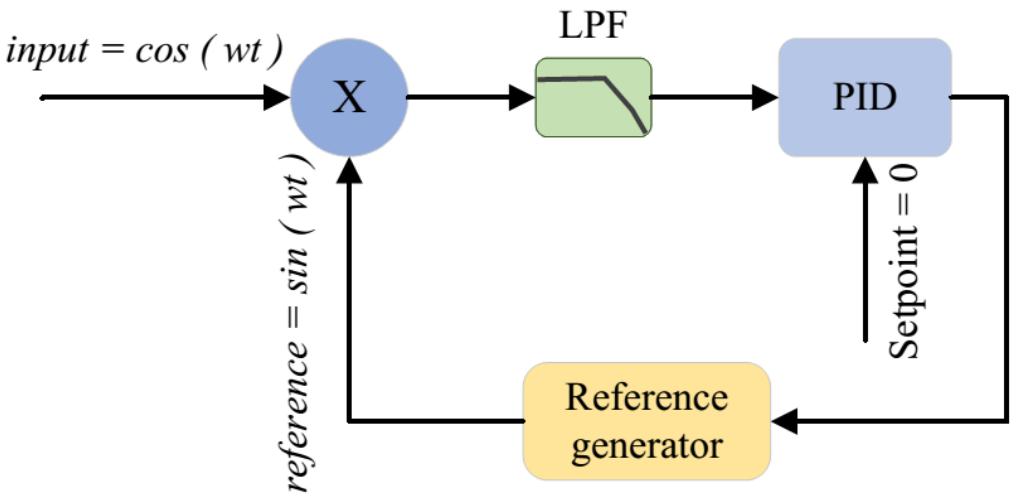

Figure 2.12: A schematic diagram showing the synchronous demodulation method. The mean of the multiplication between two signals is zero if they are 90° phase-shifted and have the same frequency.

The reference generator shown in the figure is a digitally controlled oscillator or any other mechanism that can generate a sine signal. This demodulation technique depends significantly on the phase difference between the input, and the reference signal, which must be 90°.

2.5.5 CORDIC-based frequency demodulation

Another commonly used method for frequency and amplitude demodulation is the CORDIC-based method. The input signal is converted to its in-phase and quadrature signals. Figure 2.13 shows the 'I' and 'Q' components of a signal with an 'A' magnitude.

$$In - phase\ component = I = A\cos\varphi$$

$$Quadrature\ component = Q = A\sin\varphi$$

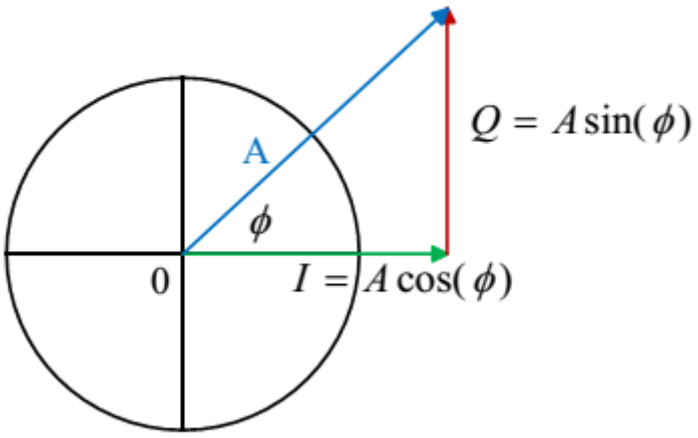

Figure 2.13: In-phase (I) and quadrature (Q) components of a signal. The amplitude of the components changes with the phase of the signal.

The following equations calculate the phase and amplitude information for the values of 'Q' and 'I' at any instant.

$$\varphi = \tan^{-1}(Q/I) \quad 2.23$$

$$A = \sqrt{I^2 + Q^2} \quad 2.24$$

Different methods can calculate a signal's quadrature and in-phase components. The most common practice is multiplying the input signal with two reference signals, which are 90° phase shifted. Figure 2.14 shows a simplified block diagram of frequency demodulation using the CORDIC function.

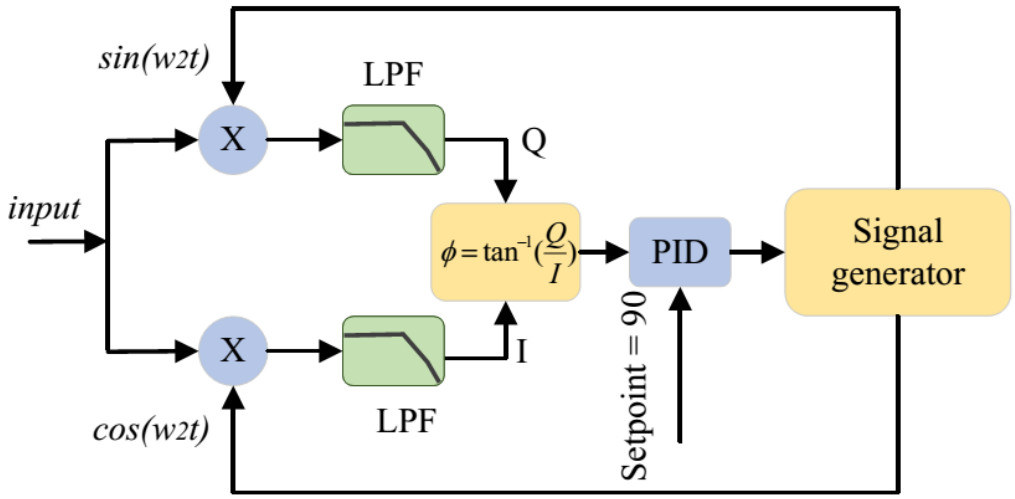

Figure 2.14: A simplified schematic of frequency demodulation using the CORDIC functions.

Another approach for finding an input signal's quadrature component is the Hilbert transform. Implementing the Hilbert transform in the digital domain consumes much processing power and is only recommended for systems with high processing power.

2.5.6 The least mean squares (LMS) based frequency demodulation

The LMS adaptive filter is another technique that can extract frequency information from an input signal. The following equations show the LMS algorithm [45]:

$$y(k) = \sum_{i=0}^{N} \omega_i(k)\ x_i\ (k-i) \qquad 2.25$$

$$e(k) = d(k) - y(k) \qquad 2.26$$

$$\omega(k+1) = w(k) + 2\,\mu\,e(k)\,x(k) \qquad 2.27$$

Where *x* is the input signal, ω is the weight vector, *d(k)* is the reference signal, *y(k)* is the filter output, *e(k)* is the error signal, and μ determines the stepsize for updating the weight vector. The filter keeps the error signal as small as possible by adjusting the μ factor.

2.6 Amplitude demodulation

Amplitude demodulation is another critical function performed in the analog readout circuit of a resonant MEMS accelerometer. The amplitude information is used to maintain a stable displacement of the resonators by comparing it with a setpoint value. There are a few techniques to calculate the amplitude of a sinusoidal signal. This section summarizes some of the commonly used methods.

2.6.1 Full wave rectification

Full wave rectification is the simplest method that can be implemented in the digital domain. In this method, the absolute value of all the input samples is passed through a low-pass filter to estimate the amplitude of the input signal. Equation 2.28 shows the relation to finding the input signal's amplitude using *N* last samples.

$$mean\ value = \ x_{avg} = \frac{1}{N}\sum_{n=1}^{N}|x_n| \qquad 2.28$$

$$N = length\ of\ low\ pass\ filter$$

The performance of this method improves by using cascaded filters with a smaller number of taps. There is a tradeoff between the speed and performance of this method. Increasing the length of the samples improves the performance but decreases the method's speed.

2.6.2 Root mean square

Root mean square (RMS) is another simple method that can be implemented in the digital domain. Equation 2.29 gives the relation to calculate the RMS value of the input signal.

$$x_{rms} = \sqrt{\frac{1}{N}\sum_{1}^{N} x^2} \qquad 2.29$$

Where *x* is the input signal sample and *N* is the number of samples used to calculate the RMS value. The accuracy of this method also improves by using a large window of samples to calculate the mean value. This method also presents a tradeoff between its performance and speed.

2.6.3 CORDIC-based amplitude demodulation

The previous section explained the CORDIC-based method to perform frequency demodulation. However, the CORDIC method also provides the amplitude information using the Pythagoras theorem, as shown in Equation 2.31. The advantage of using the CORDIC-based method is that a single method calculates both frequency and amplitude of the input signal.

$$\varphi = \tan^{-1}({}^{Q}/_{I}) \qquad 2.30$$

$$A = \sqrt{I^2 + Q^2} \qquad 2.31$$

2.7 Summary

The typical readout circuit of a resonant MEMS accelerometer can be divided into three parts: a pre-amplifier stage, an oscillation-sustaining part, and a frequency reading part. Different topologies for the pre-amplifier stage differ in their performance concerning gain, bandwidth, stability, and noise. The oscillation-sustaining part ensures a correct closed-loop operation of the resonators; however, this part is transferred to the digital domain in a digital control loop implementation. Several techniques available in the literature can be implemented in the digital domain to achieve the amplitude and frequency of the resonant MEMS accelerometer output signal.

CHAPTER 3

SENSOR DESIGN AND CHARACTERIZATION

This chapter briefly introduces the design and characteristics of the resonating MEMS accelerometer sensors used to develop the digital control loop-based readout circuit in this study, where these sensors are developed in the framework of another ongoing thesis study[1]. Section 3.1 presents the salient design features of the resonant MEMS accelerometer sensors available throughout this study. Section 3.2 reviews the results of chip-level characterization of the resonant MEMS accelerometer sensors, which is achieved using a Dynamic-Signal-Analyzer (DSA) and a Lock-in-Amplifier. Section 3.3 discusses the detailed characterization of the resonant MEMS accelerometer sensors using a lock-in-amplifier setup to obtain the sensor's resonance frequency, gain, scale factor, and bias instability. Section 0 briefly mentions the problems encountered in operating the resonant MEMS accelerometers in a closed loop using a lock-in-amplifier setup. Finally, Section 3.5 summarizes the main observations of this chapter.

3.1 Sensor Design

Three resonant MEMS accelerometers (RMA) designs were available throughout this study. The first design (R1A) has no lever mechanism, whereas the second design (R1B) has a lever mechanism. A third design (R2B), an improved version of

[1] Hassan Doğan is doing his Ph.D. on development of a high performance resonant MEMS accelerometer, and the sensors used in this study are developed as a part of his ongoing study.

the second, also has a lever mechanism. The main focus of this study is the third design, as it is used for digital control realization.

The sensor used in this study has two identical double-ended tuning fork (DETF) resonators that allow differential reading, which helps compensate for first-order temperature effects by subtracting the common drift in the resonance frequencies. The DETF beams are 4µm x 4µm x 792µm in dimension, where each DEFT is connected to an anchor at one end and to the proof mass at the other via a lever mechanism. The size of the proof mass is small to reduce the sensor footprint, but the smaller proof mass comes with a few disadvantages; higher Brownian noise due to smaller proof mass and reduced sensitivity because a smaller proof mass generates a smaller force. The sensitivity reduction problem can be solved by introducing a lever mechanism, which transfers higher force from the proof mass to the DETF resonators. The lever mechanism can be single-stage or multi-stage, but only a single-stage lever mechanism is used in the current design to avoid mechanical complexity. The other important component of a resonant MEMS accelerometer is the drive and sense electrodes. The drive electrode has 76 fingers with a 2µm gap between the electrode fingers and the resonator beams. The overlapping length between the drive electrode and beam fingers is 1µm. The drive and sense electrodes have a similar structure. The number of fingers of the sense electrodes is also 76. Equation 3.1 gives the relation for the force induced on the proof mass.

$$F_e = \frac{1}{2}\,\alpha\,\varepsilon_0\,N\,\frac{l}{d}\,V^2 \qquad 3.1$$

Where F_e is the electrostatic forcing applied on the parallel plates, α is the correction factor for the fringing fields, N is the number of fingers, l is the overlapping length, d is the gap between the plates, and V is the applied voltage between the plates.
Another electrode is also present to provide DC biasing to the proof mass. The force generated between the parallel plates of the capacitor is proportional to the square of the applied voltage. This voltage is the difference between the voltages applied to the proof mass and the drive electrodes. The sensor performance also depends on the environmental effects. One of the mediums to transfer the disturbances from the

environment to the sensor structure is the anchor points. The literature shows that the sensor performance improves by reducing the number of anchors. Therefore, the number of anchors is reduced to two to minimize frequency fluctuations caused by external factors and internally generated stress. The sensors are vacuum packaged to achieve more robustness against environmental effects, such as temperature. Table 3.1 gives different parameters for the sensor design.

Table 3.1: The salient design parameters of the sensor

Parameter	**Value**	**Unit**
DEFT beam length	792	µm
DEFT beam width	4	µm
DEFT beam mass	2.58e-10	kg
Mass of proof-mass, *m*	3.7e-7	kg
Number of fingers, *N*	76	-
Sensing gap, *d*	2	µm
Overlapping length, *l*	1	µm
Sense capacitance, *C*	11.8	pF
Sensitivity, *dC/dX*	1.18e-08	F/m

3.2 Chip-level sensor characterization

The chip-level testing ascertains the health of a sensor chip before connecting it to a PCB. Figure 3.1 shows a probe station setup that can access the electrodes of the sensor chips to perform chip-level testing. All the designs have the same pad configuration: *Pin-1* is used to supply the voltage to the wafer cap, which is either tied to the proof-mass voltage or the ground level. The wafer cap is grounded for all the tests performed except for the leakage testing. *Pin-4* is used to supply the proof-mas voltage to the proof mass of the sensor. The proof mass can get any voltage value depending on the test requirement. *Pin-2* and *Pin-3* are used to supply

excitation voltage to the resonators of a sensor. The output of the sensor is a current read at *Pin-6* and *Pin-7* (coming from the two resonators).

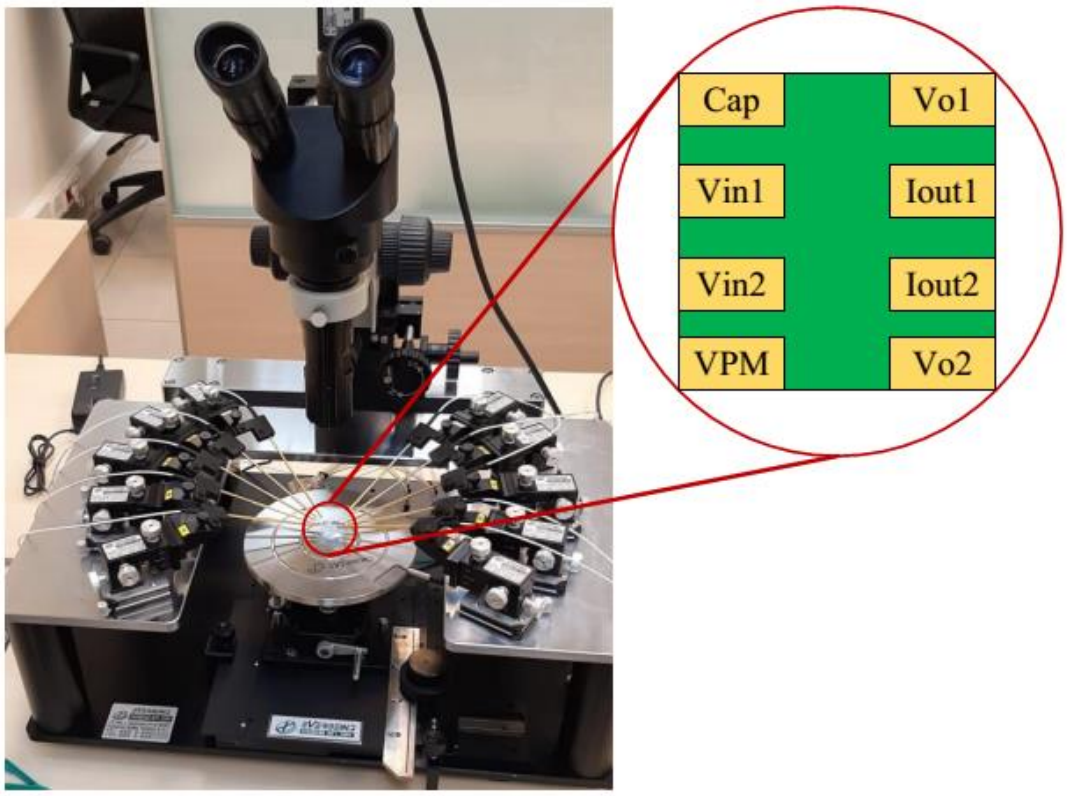

Figure 3.1: Probe station to perform chip-level testing of the sensor chips with a close conceptual view of a sensor chip showing different input and output signals of the sensor.

The input and output signals of the sensor can be connected to a dynamic signal analyzer (DSA) or a lock-in-amplifier using an interface PCB to perform chip-level tests. The interface PCB has a pre-amplifier stage for each resonator that converts the current into voltage. An additional gain stage is also present on this interface PCB to adjust the level of the sensor output signal.

The chip-level testing consists of three types of tests: (i) the first test checks for any current leakage between the wafer cap and the sensor structure, (ii) the second test is a fast Fourier transform (FFT) test to check the frequency components present in the

signals coming from the resonators, (iii) and the third is the frequency sweep test to find the exact resonance frequency value. Figure 3.2 shows a schematic of the connections for this test setup.

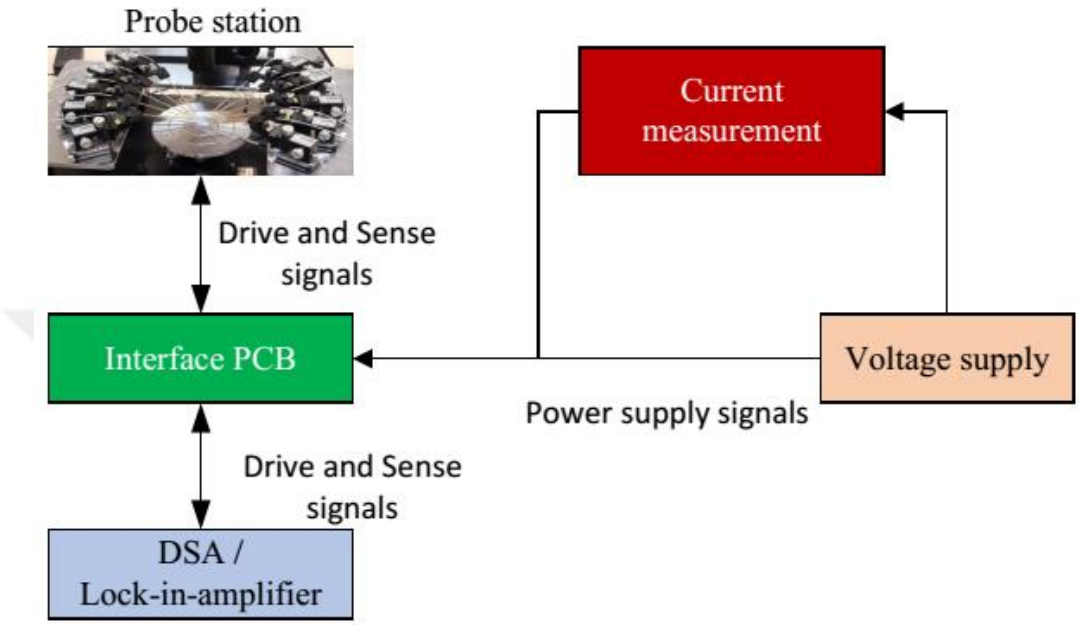

Figure 3.2: The schematic of the test setup used for chip-level testing of the developed resonant MEMS accelerometers.

3.2.1 Leakage Test

The leakage test checks if there are any unwanted shorts between different conducting components of the sensor. The probes are lowered onto the chip one by one, and the current drawn by the sensor is monitored using an ammeter. Initially, The proof-mass voltage is set to 15V, and the wafer cap is set to 0V. If no abnormal current flows due to touching down the probes under the conditions mentioned above, the wafer cap voltage is also raised to 15V. Any short between the wafer cap and other conducting parts results in an increased current drawn by the sensor. If there is no abnormal current in both biasing conditions, it can be said there is no leakage in the sensor. Both the resonators of each sensor must pass the leakage test for a qualified sensor.

3.2.2 FFT Test

FFT test can obtain an approximate resonance frequency value for any resonator. The sweep-frequency range is set very large (400~1600 Hz), and the excitation voltage is also set high (100mV). The proof mass voltage is varied between 3V and 15V to observe any resonance behavior.

Table 3.2 shows the results of a chip-level characterization of the sensors selected from the final design (R2B-type). The resonance frequency lies in the region between 16kHz and 17kHz. The two resonators of any chip have different resonance frequencies, which also vary from chip to chip. Also, the difference between the resonance frequencies of the two resonators of a single sensor is not constant for all chips. This difference varies between 43Hz and 187Hz in different sensors and results from fabrication imperfections. The resonance frequency of the resonators also changes with time.

3.2.1 Frequency Sweep

After obtaining an approximate resonance frequency of each sensor chip, the frequency sweep test in a narrow range is performed to get a more accurate resonance frequency value. The frequency range is now reduced to 10Hz around the approximate resonance frequency. A narrow frequency range requires a low excitation voltage. Therefore, the excitation voltage level is reduced to 0.25mV. The frequency sweep is performed at different values of proof mass voltage, such as 3V, 5V, and 10V. The results from the frequency sweep are consistent with the results obtained in the FFT test but with more accuracy.

Table 3.2: The chip level sensor characterization of the R2B-type resonant MEMS accelerometers showing resonance frequency under different biasing conditions.

Sensor No	Proof mass voltage	Resonance frequency 1 (Hz)	Resonance frequency 2 (Hz)	Difference |f1-f2|
N4N4	10V	16428.4	16240.8	187.6
	5V	16424.3	16236.5	187.8
	3V	16423.4	16235.5	187.9
N4N2	10V	16604.1	16540	64.1
	5V	16601.4	16537	64.4
	3V	16600.7	16536.5	64.2
N4P3	10V	16924.7	17018	93.3
	5V	16921.8	17015.5	93.7
	3V	16921.1	17014.9	93.8
N3N7	10V	16997.5	17044.7	47.2
	5V	16993	17040.9	47.9
	3V	16991.7	17040.1	48.4

3.3 Sensor Characterization with lock-in-amplifier

The resonant MEMS accelerometer sensors qualified in the chip-level testing are selected and soldered to a pre-amplifier PCB module, which is suitable for testing with a lock-in-amplifier and a digital control PCB to implement a digital control loop for the resonant MEMS accelerometer. The output of this amplifier module is signals from the sensor amplified by the pre-amplifier, and the input to this PCB is the drive signals to oscillate the resonators. Figure 3.3 shows a conceptual connection diagram

for the test setup employing the lock-in-amplifier, which converts the analog signal to the digital domain using an ADC and then generates the drive signals using a DAC after processing in the digital domain.

The sensor characterization is carried out systematically to get an in-depth understanding of the sensor behavior. Different parameters, such as proof-mass voltage, excitation voltage, and PLL parameters, affect the performance of these sensors, and their effect can be observed in the sensor output data.

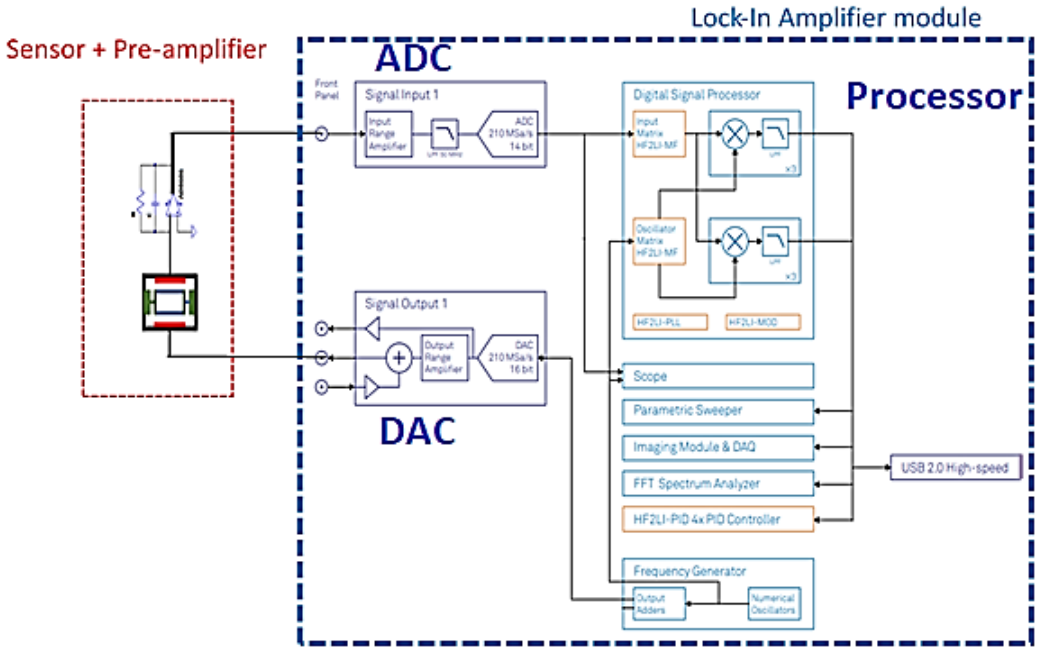

Figure 3.3: The setup diagram for testing the resonant MEMS accelerometers with a lock-in-amplifier showing major components of the testing scheme.

3.3.1 Frequency Sweep

Testing with a lock-in-amplifier also starts with frequency sweeping to know the exact value of resonance. Understanding the resonance behavior of the resonators in their new configuration is essential. The resonance frequency and gain of sensors are

affected by several factors that can be modified. Especially the amplification is very much dependent on the biasing conditions. It is, therefore, necessary to perform the sweep test at different biasing conditions. The test settings are as follows:

Proof mass voltage: 3V~15V

Excitation voltage: 0.1mV~5mV

The biasing conditions determine the sensor's region of operation. Too high excitation voltage levels can push the sensor into a non-linear region. Therefore, it is also essential to know the limits of the excitation voltage level that should be applied to excite the sensor. The frequency sweeping is carried out at different values of proof mass voltage and excitation voltage, and their effects on the resonance frequency, gain, and region of operation are recorded for later use.

Figure 3.4 shows the result of the frequency sweep of *Resonator 1* of sensor N4N2 at different proof mass voltages using a lock-in-amplifier, using 0.1mV excitation voltage. The plot shows that the resonance frequency of this resonator changes only a few Hz when the proof mass voltage is changed. The figure also shows an increase in the gain of the resonator as the proof-mass voltages increases from 5V to 15V. The figure also shows the phase response of the resonator at different biasing conditions. The phase changes sharply at the point of the resonance frequency. The resonance frequency of *Resonator 1* is approximately 16763Hz at 5V proof-mass voltage, which increases to 16766Hz at 15V proof-mass voltage.

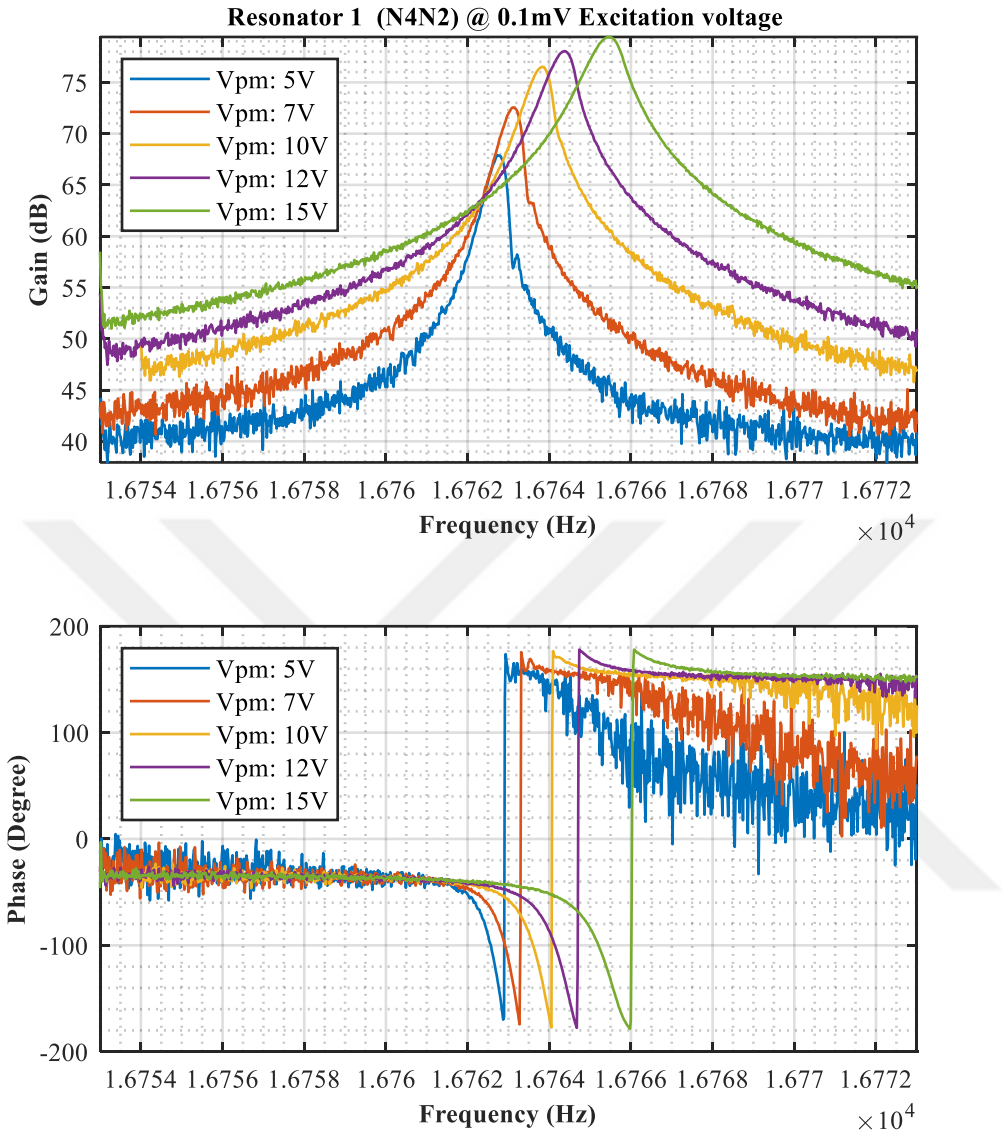

Figure 3.4: The frequency response of *Resonator 1* of sensor N4N2 at different proof mass voltages with excitation voltage set to 0.1mV, showing approximately 16763Hz resonance frequency.

Figure 3.5 shows the frequency response of *Resonator 2* of sensor N4N2 at different proof-mass voltage values while the excitation voltage is set to 0.1mV. The resonance frequency of *Resonator* 2 is approximately 16480Hz at 5V proof-mass voltage, which increases to 16483Hz at 15V proof-mass voltage. The plot shows an

increase in the gain as the proof mass voltage is increased from 5V to 15V. The figure also shows the phase response of the resonator, where the phase changes sharply at the resonance frequency point. The resonance frequency of *Resonator 2* is approximately 187Hz lower than the resonance frequency of *Resonator 1*.

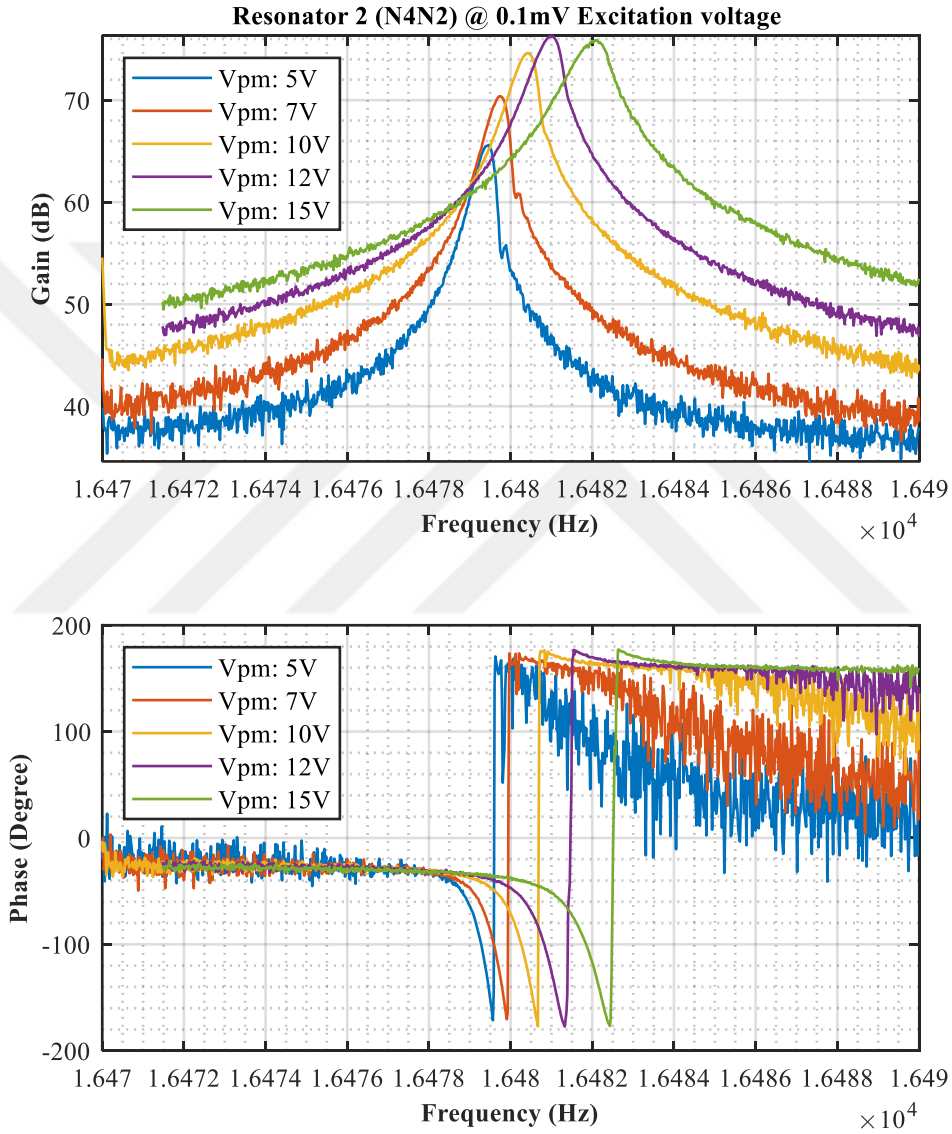

Figure 3.5: The frequency response of *Resonator 2* of sensor-N4N2 at 0.1mV excitation voltage under different values of proof-mass voltage. The resonance frequency is approximately 16480Hz.

Figure 3.6 shows the frequency sweep response *Resonator 2*, demonstrating the linear and non-linear behavior of the resonator at 5V proof-mass voltage. The gain and phase response at 2mV excitation voltage indicates a non-linear behavior. A higher value of excitation voltage must be avoided for a linear operation.

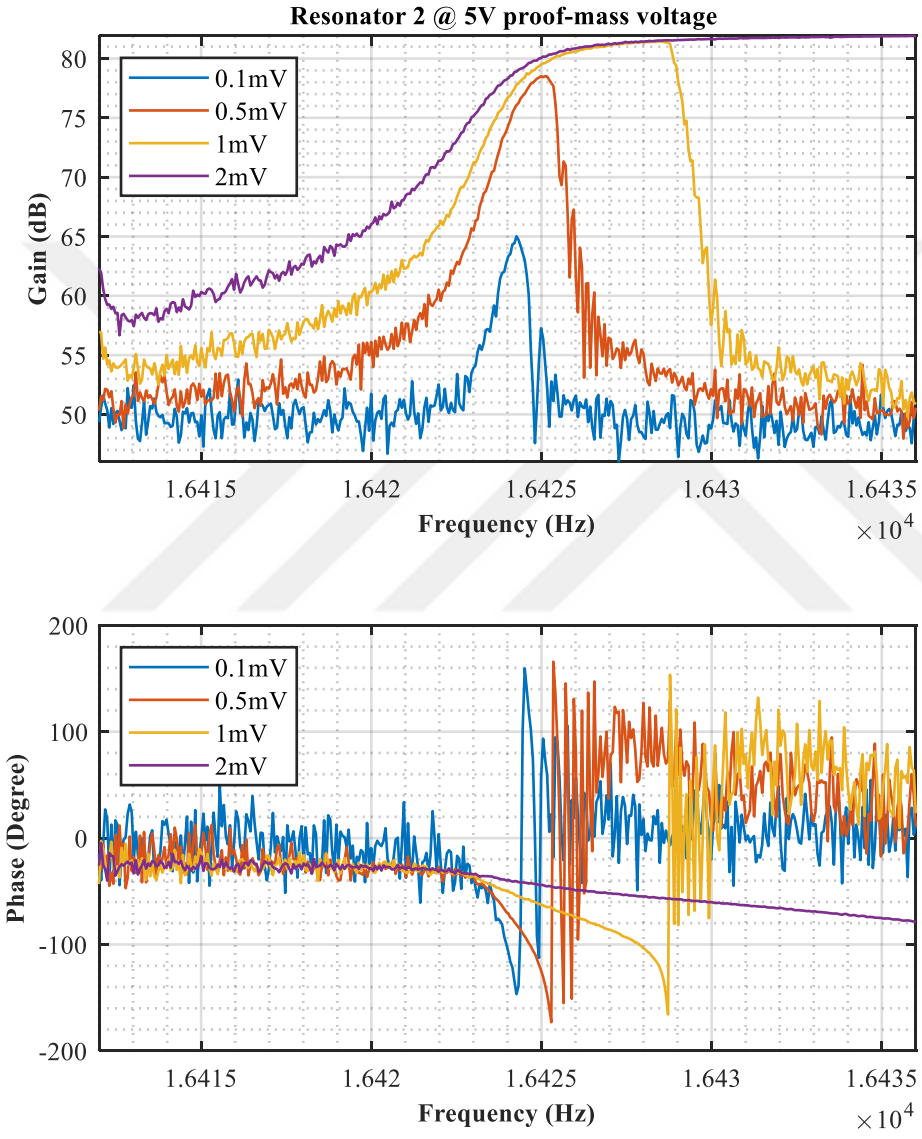

Figure 3.6: Frequency response of *Resonator 2* of sensor-N4N2 at 5V proof mass voltage showing non-linearity at higher values of excitation voltage.

Figure 3.7 summarizes the resonance frequency behavior of the *Resonator 1* of the sensor N4N2 under different biasing conditions. The x-axis shows the biasing conditions as a set of the proof mass voltage and the excitation voltage. The first number shows the proof mass voltage in volts, and the number after '+' shows the excitation voltage in mV. The plot shows that the resonance frequency of *Resonator 1* is not much affected by the change in the proof mass voltage or the excitation voltage.

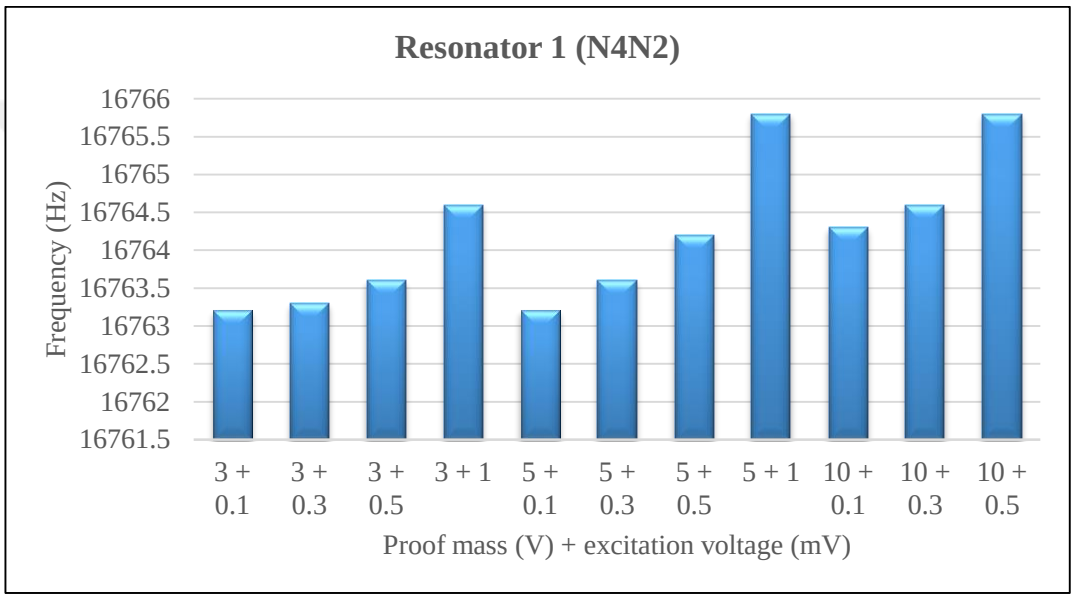

Figure 3.7: Summary of the resonance frequency of *Resonator 1* of sensor-N4N2 at different biasing conditions. There is not much change in the resonance frequency of *Resonator 1* due to a change in the biasing conditions.

Figure 3.8 summarizes the resonance frequency behavior of *Resonator 2* of the sensor N4N2 under different biasing conditions. The x-axis shows the biasing conditions as a set of the proof mass voltage and the excitation voltage. The first number shows the proof mass voltage in volts, and the number after '+' shows the excitation voltage in mV. The plot shows that the resonance frequency of *Resonator 2* also is not much affected by the change in the proof mass voltage or the excitation

voltage. The change in the resonance frequency due to the changes in the biasing voltages is not more than two or three hertz.

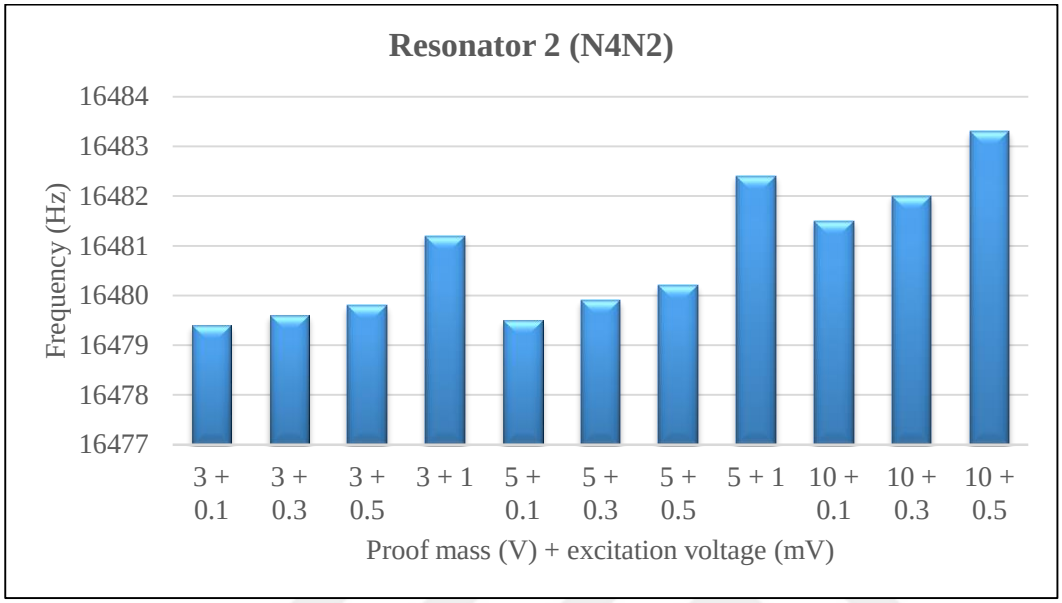

Figure 3.8: Summary of the resonance frequency of *Resonator 2* of sensor-N4N2 at different biasing conditions. There is not much change in the resonance frequency of *Resonator 2* due to a change in the biasing conditions.

The frequency sweep tests performed on other resonant MEMS accelerometer sensors with similar biasing conditions show similar behavior. This section has presented detailed results for all the possible biasing conditions applied to the sensor-N4N2. However, for brevity, one plot each from sensors N4N1 and N4P3 to understand the general trend of the R2B-type sensors is shown here. Figure 3.9 shows the frequency sweep response of *Resonator 1* of sensor-N4N1 at 5V proof mass voltage under different values of excitation voltage. The resonance value of this resonator is around 16922Hz, which is approximately 400Hz higher than the *Resonator 1* of the sensor-N4N2. The resonator shows a linear behavior for 0.1mV, 0.3mV, 0.5mV, and 1mV excitation voltage. Increasing the excitation voltage shifts the resonance frequency, and the sensor goes into nonlinearity. Compared to sensor N4N2, this resonator does not go into the non-linear region at 1 mV. It shows that

the nonlinearity threshold is different for different sensors, and it is critical to perform sweeping frequency tests to find the limits of non-linearity.

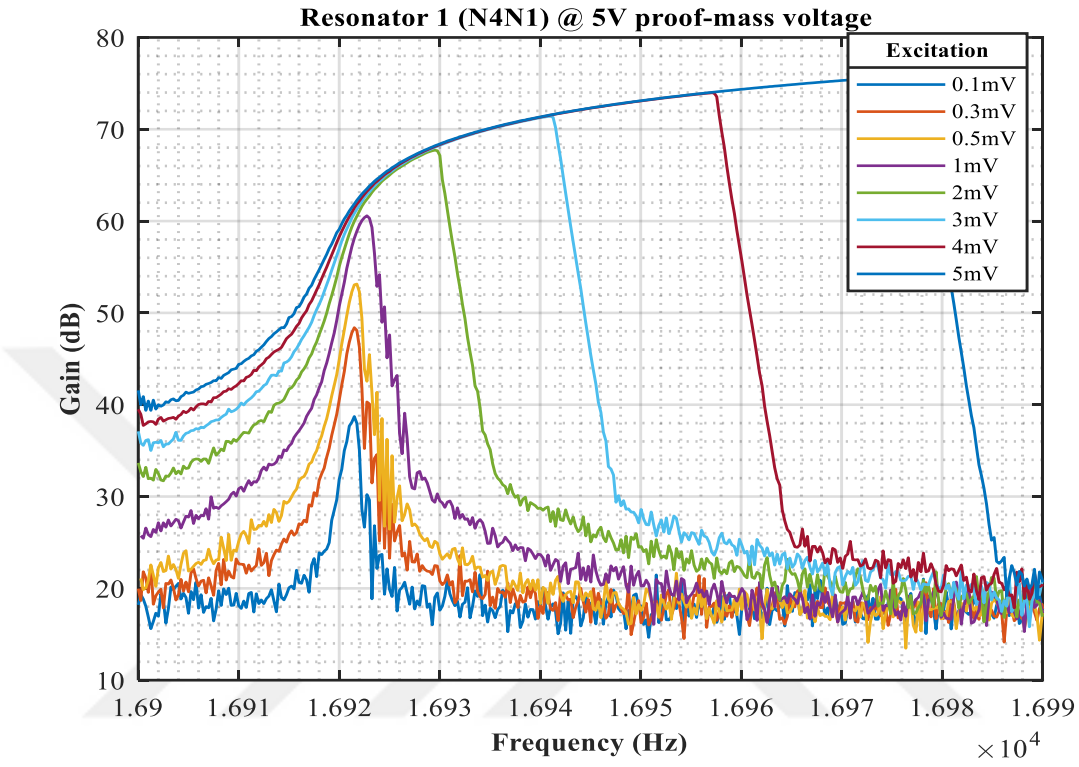

Figure 3.9: The frequency response of *Resonator 1* of sensor-N4N1 at a 5V proof mass voltage shows 16922Hz resonance frequency. A non-linear behavior is present at excitation voltage values higher than 1mV.

Figure 3.10 shows the frequency sweep response of *Resonator 2* of sensor-N4P3, showing a resonance frequency of approximately 16975Hz. This resonance frequency value is different from the values of sensors N4N2 and N4N1. This observation was also noted during the chip-level testing that the resonance frequency of the sensor varies from chip to chip. The plot in the Figure 3.10 shows that the sensor goes into a non-linear region at 2mV for 5V proof mass voltage.

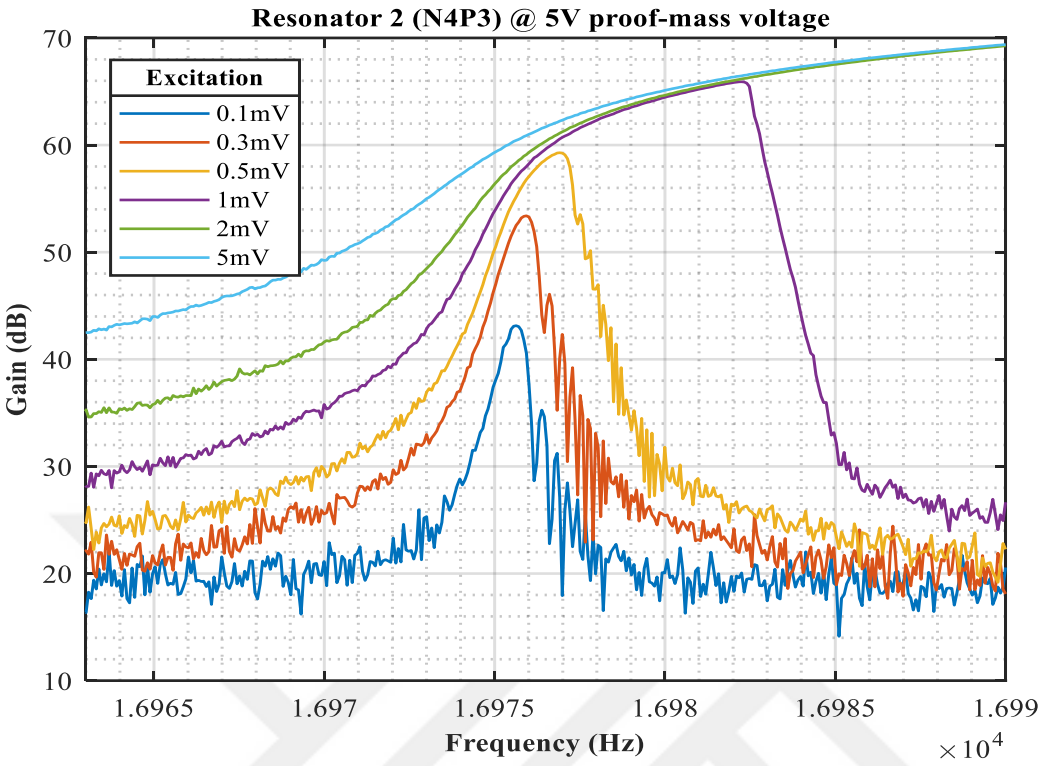

Figure 3.10: The frequency response of *Resonator 2* of sensor-N4P3 at a 5V proof mass voltage, showing a non-linear behavior at 2mV and higher excitation voltage values.

The results of this section underline the importance of frequency sweep at several biasing conditions because every sensor has a different threshold for excitation voltage that drives it into a non-linear region. The general trend is the same for all the sensors: the excitation voltage threshold is reduced with an increase in the proof-mass voltage. Therefore, it can be concluded that the gain depends on the proof-mass voltage, and the linearity of the response is dependent on the excitation value. The correct proof mass and excitation voltage combination operate the resonators at the desired gain value without going into the non-linear region.

3.3.2 Closed loop testing with the lock-in-amplifier

There are two essential requirements to operate the resonator in a closed-loop form: (i) the first is frequency tracking, (ii) and the second requirement is maintaining a stable output amplitude. The frequency tracking of the resonators of a resonant MEMS accelerometer can be performed using a proportional-integrator (PI) controller-based phase-locked loop (PLL) block present in the lock-in-amplifier, whereas another PI controller block performs the amplitude stabilization.

3.3.2.1 PLL for frequency locking

A PLL is used in the lock-in-amplifier for frequency tracking. The frequency demodulation results in the extraction of phase information and other parameters. A PI controller compares the calculated phase with a set-point phase. A numerically controlled oscillator generates the reference signal according to the PI controller output. The performance of a PI controller depends on the values of its parameters. Figure 3.11 shows a conceptual representation of a PLL.

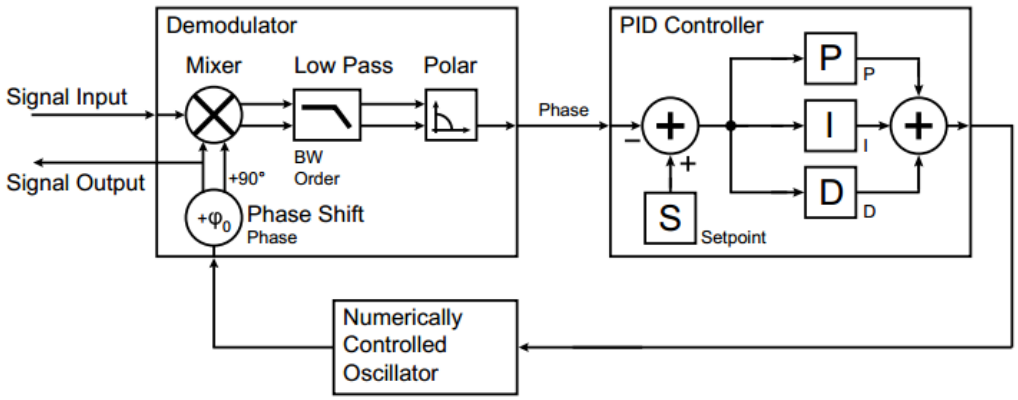

Figure 3.11: The block diagram of the PLL implementation of the lock-in-amplifier used in this study. The phase is used as a setpoint to track the input signal's frequency.

The phase difference obtained from the input and reference signals is compared with the set-point phase value. The difference between the actual and desired phase is the error signal that is used as input of the PI controller. The parameters *P* (proportional) and *I* (integral) are multiplied by the phase-error signal.

3.3.2.2 PID for stable output amplitude

The output amplitude of the resonator is maintained at a fixed point using a PI controller in the lock-in-amplifier. The user interface of the lock-in-amplifier accepts a fixed amplitude point and maintains the output amplitude at that set-point value. The proportional and integrator parameters control the performance of this PI controller. However, the speed of the amplitude stabilization PI controller does not require to be as fast as the frequency tracking PLL. Figure 3.12 shows an Allan variance plot of the data obtained from the sensor N4N2. The plot shows a 34µg/√Hz noise level and a bias instability of 10µg at 3V proof mass and 0.3mV excitation voltage. The bias value remains under 20 µg even after 200sec showing the inherent stability of the sensor at room temperature.

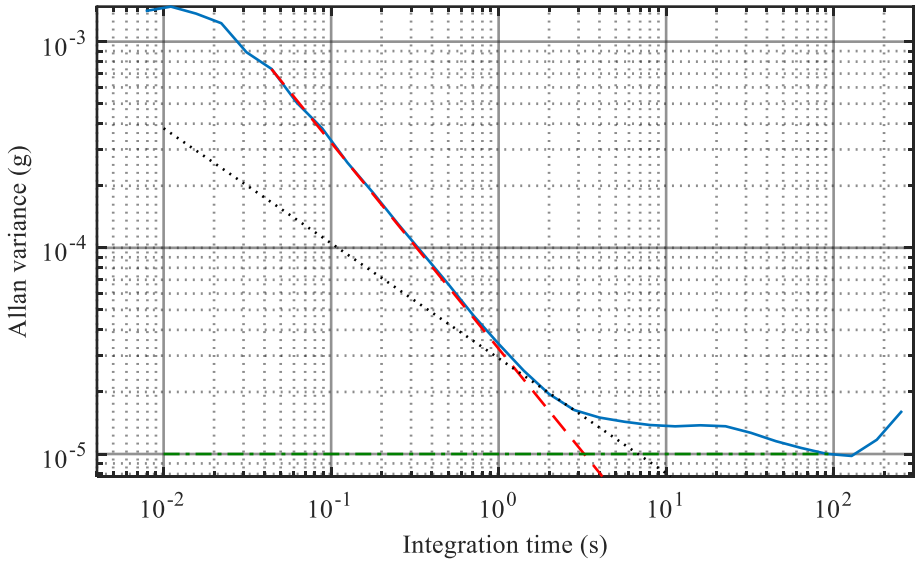

Figure 3.12: Allan variance plot of sensor N4N2 at 3V proof mass and 0.3mV excitation voltage showing 10µg bias instability and 34µg/√Hz noise level.

The data is collected at different values of the proof mass and excitation voltage to calculate the noise level and bias instability. Table 3.3 summarizes noise values and bias instability calculated from sensor data at several biasing points. The results show a bias instability value of 7µg, and a noise level of 10µg/√Hz can be obtained from this sensor. These values are also dependent on the bandwidth used in the PID controller, where a higher bandwidth increases the noise in the data and degrades the bias instability. The data shown in this table is collected at 20Hz bandwidth. Increasing the bandwidth increases the sensor's response time and the fluctuation in the demodulated frequency. The proof mass and excitation voltage also affect the bias instability and the sensor noise. The increase in the excitation voltage decreases the noise and bias instability of the sensor: the noise level drops from 109µg/√Hz to 26µg/√Hz when the excitation voltage increases from 0.1mV to 0.5mV while the proof-mass voltage is 3V. Similar improvement can be seen with an increase in the excitation voltage under 5V and 10V proof-mass voltage values. The proof-mass voltage also affects the noise and bias instability levels, and the results show that the noise and bias instability improves with the proof-mass voltage increase.

Table 3.3: Summary of noise and bias instability calculated at different biasing conditions at 20Hz bandwidth (sensor-N4N2 R2B-type).

Proof mass	**Excitation voltage**	**Noise (µg/√Hz)**	**Bias instability (µg)**
3V	0.1mV	109	9.4
	0.3mV	34	9.7
	0.5mV	26	9.2
5V	0.1mV	99	10
	0.3mV	41	9
	0.5mV	25	9
10V	0.1mV	60	8

3.3.3 Scale factor

The scale factor shows the sensitivity of a resonant sensor in terms of Hz/g. The scale factor of these sensors is calculated using 0g, +1g, and -1g positions. Each sensor has two resonators, so their sensitivity is calculated separately, and then the differential reading is taken to obtain the total scale factor. The following statements provide a simple method to calculate the scale factor of the sensors.

$$Sensitivity\ of\ Resonator\ 1, S_{R1} = {}^{Hz}/_{2g}$$

$$Sensitivity\ of\ Resonator\ 2, S_{R2} = {}^{Hz}/_{2g}$$

$$Scale\ factor, S_F = \frac{(S_{R1} + S_{R2})}{2}\ {}^{Hz}/_{g}$$

Figure 3.13 shows the scale factor calculation with the proof mass voltage set to 3V and the excitation voltage set to 0.3mV. The sensitivity of *Resonator 1* is approximately 44.8 Hz/g, and the sensitivity of *Resonator 2* is approximately 50.15 Hz/g. The differential scale factor of the sensor N4N2-R2B at these biasing conditions is 95.05 Hz/g.

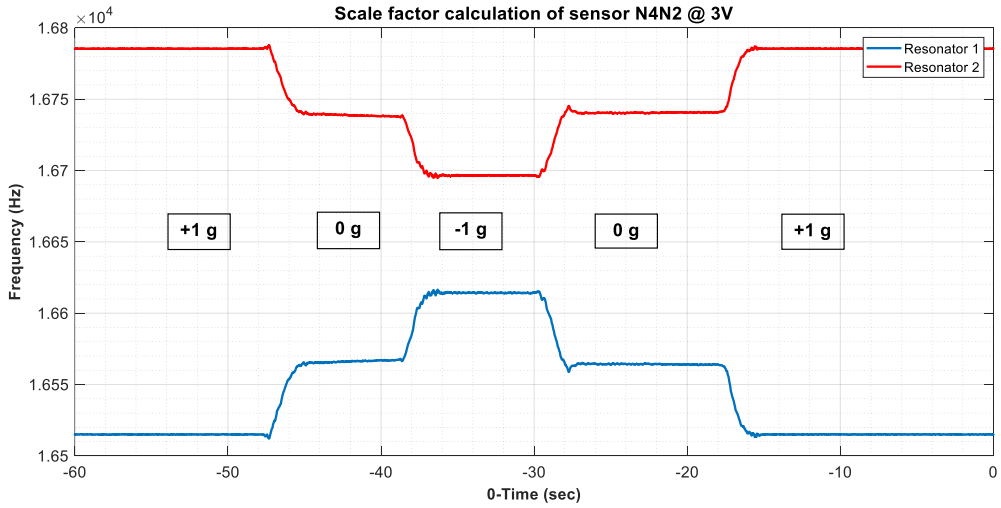

Figure 3.13: Scale factor calculation for sensor N4N2 at 3V proof mass voltage showing a scale factor of 95Hz/g.

The proof mass and excitation voltage are changed to measure the scale factor at different values. Figure 3.14 shows the scale factor calculation at 10V proof mass voltage. The scale factor value at these conditions is 94.5 Hz/g.

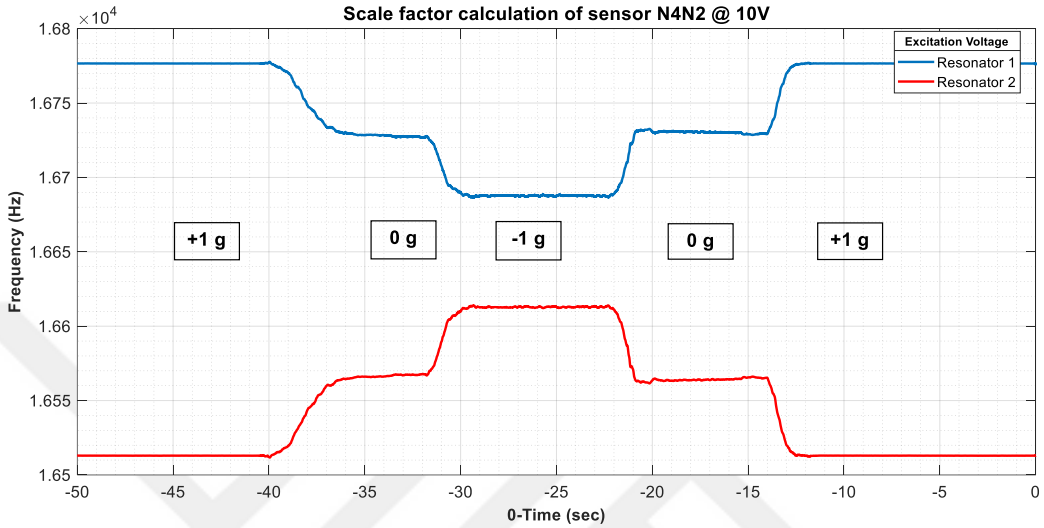

Figure 3.14: Scale factor calculation for sensor N4N2 at 10V proof mass voltage showing a scale factor of 94.5Hz/g. The scale factor is stable under different biasing conditions.

Several proof mass and excitation voltage pairs are used to measure the scale factor to understand the effect of biasing conditions on the sensitivity of the sensor. Table 3.4 presents a summary of these calculations, and the results show that the scale factor of sensor-N4N2 is stable under all the mentioned conditions. There is a total change of less than one hertz. Also, this change can be the result of a measurement error or an actual change in the resonance frequency under the effect of different biasing conditions. The test setup used to rotate the sensor in different positions is not very accurate; therefore, the measured scale factor change most likely results from the measurement error.

Table 3.4: Summary of scale factor calculation results at different biasing conditions for sensor-N4N2 (R2B-type). The results show a stable scale factor (~95Hz) under different biasing conditions.

Proof mass voltage	Excitation voltage	Sensitivity R1 (Hz/g)	Sensitivity R2 (Hz/g)	Scale factor (Hz/g)
3V	0.1mV	45.55	49.6	95.15
	0.3mV	44.8	50.15	94.95
	0.5mV	44.45	49.6	94.05
5V	0.1mV	44.3	50.35	94.65
	0.3mV	44.3	50.15	94.45
	0.5mV	44.5	50.05	94.5
10V	0.1mV	44.55	49.95	94.5
	0.3mV	44.3	50.1	94.4
	0.5mV	44.3	49.95	94.25

3.4 Problems and observations

Some problems were encountered while implementing the closed-loop operation using the lock-in-amplifier. The input of the lock-in-amplifier is noisy, and it cannot read signals with a small amplitude (<1mV). Therefore, there was too much noise in the data collected from the sensor. A way around this problem is to introduce a gain stage between the pre-amplifier and the lock-in-amplifier input. This gain stage improved the SNR, and there was a significant reduction in the noise. Secondly, the excitation voltage for the drive electrodes is also less than 1mV for a linear operation. It is critical to generate such a small signal without adding a significant noise from the readout circuit.

3.5 Summary and discussion

The resonant MEMS accelerometer sensors used to develop the digital control loop-based readout circuit in this study are characterized first at the chip level using a DSA and a lock-in-amplifier setup. Then the detailed characterization is performed using the lock-in-amplifier. Testing with different sensors (type-R1A and type-R2B) reveals that resonators' resonance frequencies differ, which varies with each sensor. This difference is 43Hz in some of the sensors and approximately 187Hz in some of the sensors. Additionally, the resonance frequency shifts from sensor to sensor, indicating an imperfection in the fabrication process. Characterization results show that the resonance frequency of the sensors does not change much with a change in the biasing conditions, while the sensors operate in linear regions. The linearity of the sensor operation depends on the value of the proof-mass voltage and the excitation voltage. The proof-mass voltage is directly proportional to the gain and SNR of the sensor. However, higher values of proof-mass voltage drive the sensor into non-linear regions. A higher excitation voltage value also drives the resonators into the non-linear region. The threshold of excitation voltage, which keeps a linear operation, decreases with an increase in the proof-mas voltage. The resonance frequencies of the sensor-N4N2 are approximately 16516Hz and 16784Hz during the presented sensor characterization. The scale factor of this sensor is approximately 95Hz/g. This sensor shows a bias instability of 7μg.

CHAPTER 4

IMPLEMENTATION OF DIGITAL CONTROL LOOP-BASED READOUT

This chapter explains the implementation of the digital control loop-based readout circuit using a microcontroller. Section 4.1 presents different blocks of a digital control loop-based readout circuit and their comparison to a typical analog readout circuit of a resonant MEMS accelerometer. Section 4.2 explains the components of the readout circuit, such as the pre-amplifier stage, the gain stage, the analog-to-digital conversion, the microcontroller, and the digital-to-analog conversion. Section 4.3 provides a noise analysis of the proposed readout circuit. Section 4.4 reviews the interpretation of noise using Allan variance plots. Section 4.5 shows the simulation results of the Simulink model of the readout circuit. Section 4.6 presents the technique used to operate the sensor in a closed loop using a microcontroller. Section 4.7 explains different algorithms used to realize different functionalities of a closed-loop operation in a microcontroller. Section 4.8 summarizes the focal points of a digital control loop implementation.

4.1 Blocks of the digital readout circuit

Figure 4.1 shows a block diagram of a digital readout circuit of a resonant MEMS accelerometer. Some digital readout circuit blocks for a resonant MEMS accelerometer are similar to an analog readout circuit. As mentioned in Chapter 2, an analog readout for a resonant MEMS accelerometer has three main components: the pre-amplifier stage, the oscillation-sustaining circuit, and a frequency reading mechanism, as shown in Figure 2.3. The preamplifier stage, which converts low-level current signals to readable voltage values, is also necessary for the digital

readout circuit, while the functions of the remaining two blocks are achieved for the digital readout circuit in the digital domain with a microcontroller after the analog signals are converted to the digital domain.

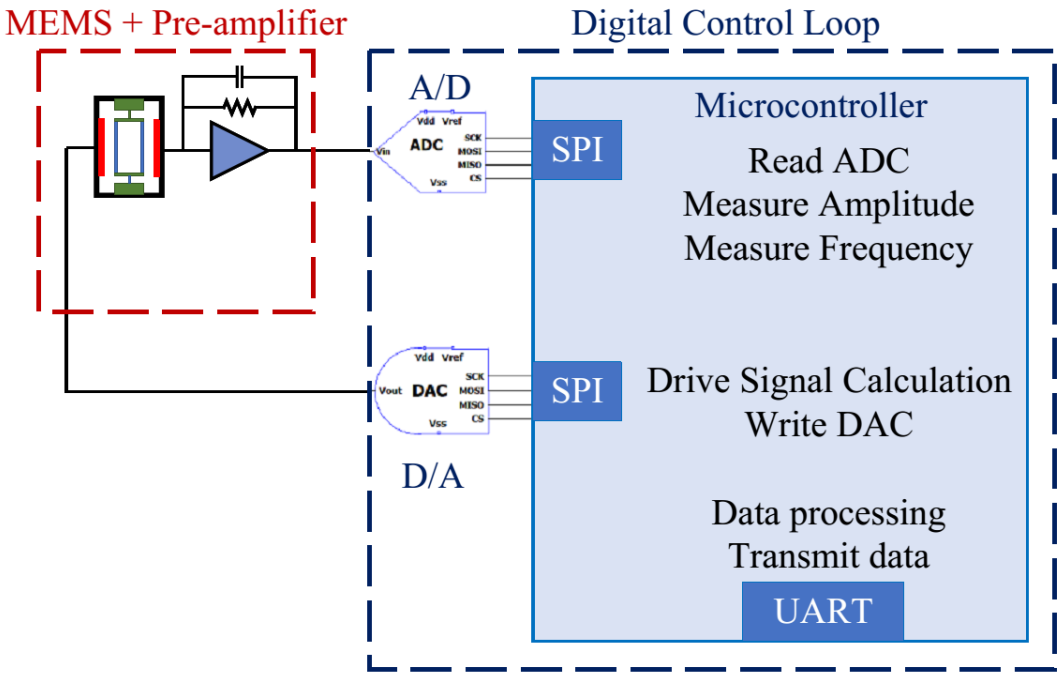

Figure 4.1: Conceptual diagram of the digital implementation of a resonant MEMS accelerometer. Off-the-shelf components are used to realize the digital control loop.

An ADC converts the analog signals to the digital domain. The quality of this conversion depends on the number of ADC bits and the sampling rate. Some of the functionalities previously performed in the analog are transferred to the microcontroller, such as amplitude and frequency demodulation. A PI controller inside the processor maintains the output amplitude by comparing the demodulated amplitude with a set-point value. Another PI controller-based PLL is implemented in the software to track the resonance frequency. The DAC generates the drive signals to oscillate both resonators. The excitation signal amplitude is based on the PI controller output that controls the output amplitude, whereas the PLL output controls the excitation signal frequency. A serial port transmits the frequency and

amplitude information to a computer or a system that will use this output data to provide the acceleration information.

4.2 Circuit Implementation

The digital control is implemented using discrete off-the-shelf components. The ADC converts the analog signals to the digital domain, and the DAC converts them back to the analog domain after processing. Different components require different voltage levels, such as 1.2V, 2.5V, 4.5V, and 3.3V. A single 5V is the input to this digital control PCB. The different power supply levels are generated using power conversion ICs.

Amplification is required at different stages in the circuit for a smooth operation. The first amplification stage is the pre-amplifier stage which converts the motional current into voltage. The characterization results show that an additional gain stage is required to improve the SNR of the signal at the input of the ADC. The second amplification stage is used to increase the input signal level. A well-defined input signal achieves a better result from the product between the input and the reference signal while extracting the frequency information. Therefore, the input signal is amplified before reading by the ADC. Amplification is also required to generate DC voltages for the proof mass and the wafer cap. The DAC can generate signals from 0~2.5V, but the proof mass and the wafer cap may require voltage up to 20V. In order to control the proof mass and the wafer cap voltage through software, an amplification stage is present after the DAC. The level of drive signals is small (typically < 1mV) and falls well within the range of the DAC, and hence does not need an additional amplification stage.

Figure 4.2 shows the schematic of the first component of the circuit comprising the sensor module and pre-amplifier stage. The sensor module has four inputs: two drive signals, cap wafer voltage, and proof mass voltage. There are two resonators in the sensor chip, and the two drive signals oscillate the resonators independently. The cap

wafer voltage provides a DC biasing to the wafer cap. The wafer cap should either be grounded or connected to the proof-mass voltage. The sensor's output is a current signal fed to the pre-amplifier stage. There are two resonators and hence two current outputs. Two additional pins provide feedback capacitance to the sensor.

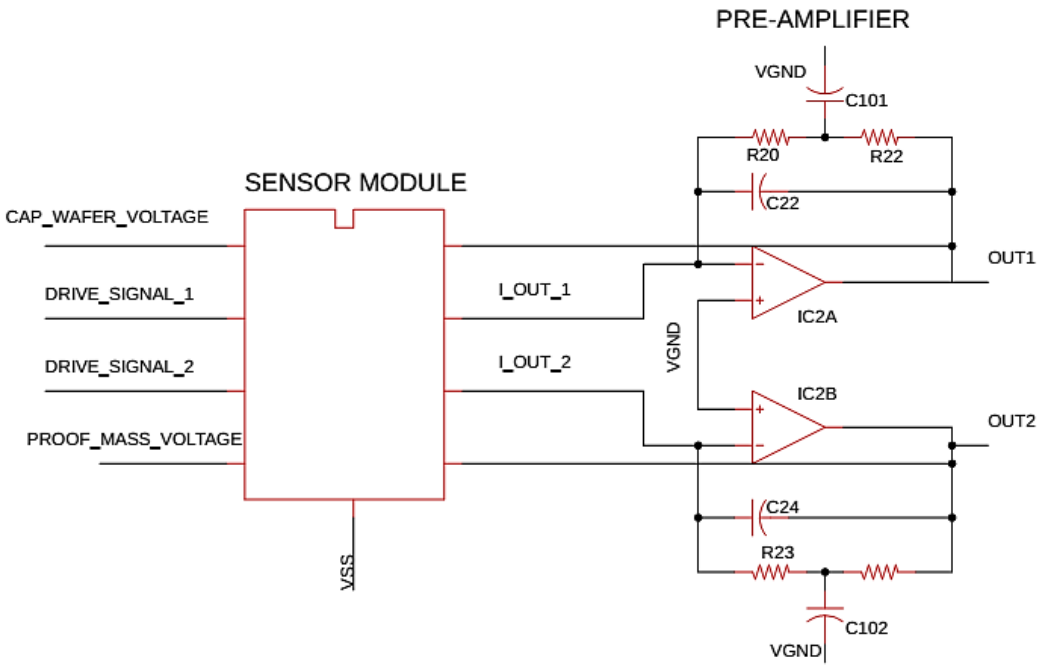

Figure 4.2: The schematic for the pre-amplifier stage and sensor module. A charge-sensing pre-amplifier scheme is used to obtain a substantial gain and a good noise performance.

The amplifier IC shown in the circuit diagram in Figure 4.2 has two amplifiers that amplify the signals from both resonators of a sensor. The pre-amplifier stage is a charge-sensing configuration where high resistance is used for DC biasing, and capacitance is used to achieve a very high gain. This pre-amplifier configuration has been discussed in a previous chapter. It provides high gain, and its noise performance is better than some other pre-amplifier configurations. A very high feedback resistor value limits the input-referred noise, which is critical for noise performance. Equation 4.1 gives the gain of the charge-sensing amplifier.

$$R(s) = \frac{R_b}{R_b\, C_f\, s + 1} \qquad 4.1$$

Where R_b is the biasing resistance, and C_f is the feedback capacitance. The biasing resistor used in the circuit has a value of 470MΩ, and the value of the feedback capacitor is 1pF. The gain of the pre-amplifier stage is approximately 52.28M around the oscillation frequency.

The gain and phase plot of the pre-amplifier stage is obtained using the Ltspice software, as shown in Figure 4.3. The parasitic capacitance of 14pF is used in the simulation as per the amplifier's datasheet values.

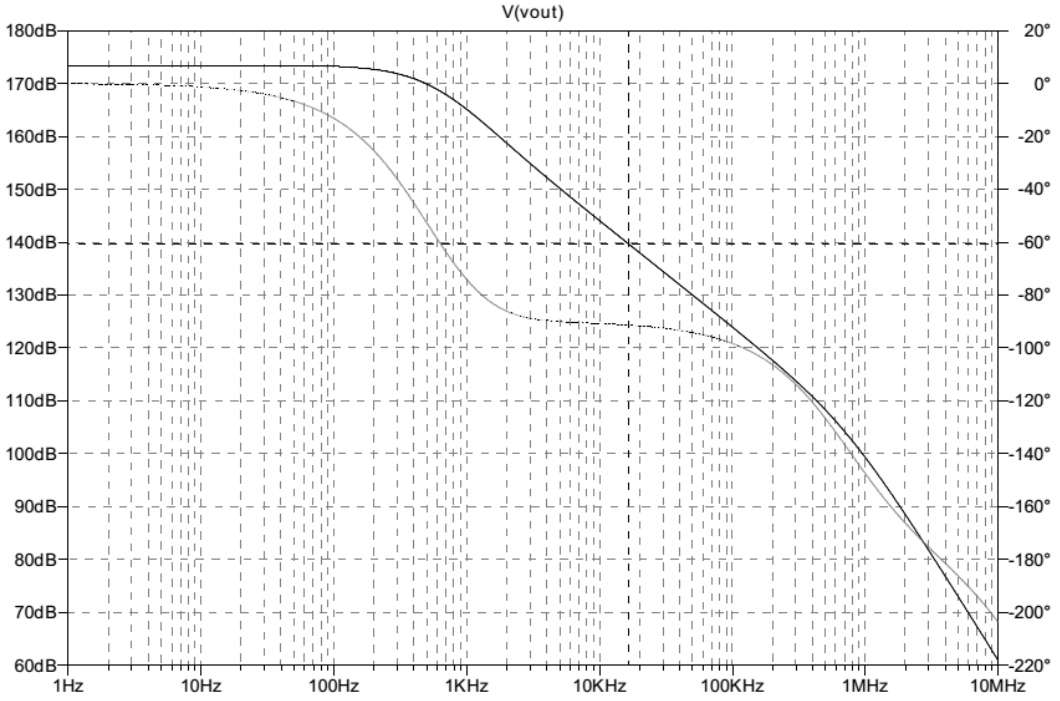

Figure 4.3: Phase and gain plot of the pre-amplifier stage simulated in ltspice. The gain at the oscillation frequency (17kHz) is 140dB.

The noise simulation of the pre-amplifier is shown in Figure 4.4 using ltspice software. The output noise is higher at lower frequencies, whereas its value decreases as the frequency increases and obtains a stable value after some point. The resonance

frequency is greater than 16kHz for all types of sensors used in this study. At this frequency value, the noise value is relatively low.

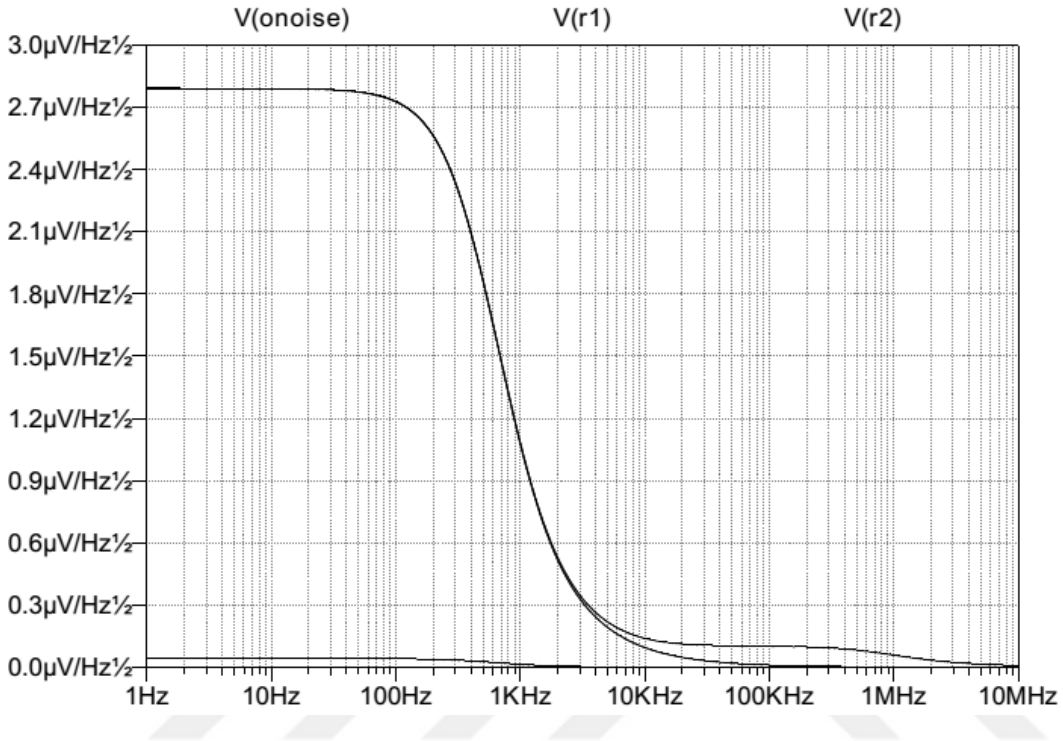

Figure 4.4: The output noise of the pre-amplifier stage simulated in ltspice showing 116nV/ √Hz output noise voltage around the oscillation frequency of the resonant MEMS accelerometers used in this study.

Figure 4.5 shows the circuit's next stage, where the pre-amplifier signal goes to the ADC after passing through an instrumentation amplifier. The amplifier stage provides gain to the input signal, and a differential signal is fed to the ADC to eliminate common biasing errors. The characterization results section has already discussed the importance of this intermediate stage. It provides an amplified signal to the microcontroller to achieve a useful multiplication product for frequency demodulation.

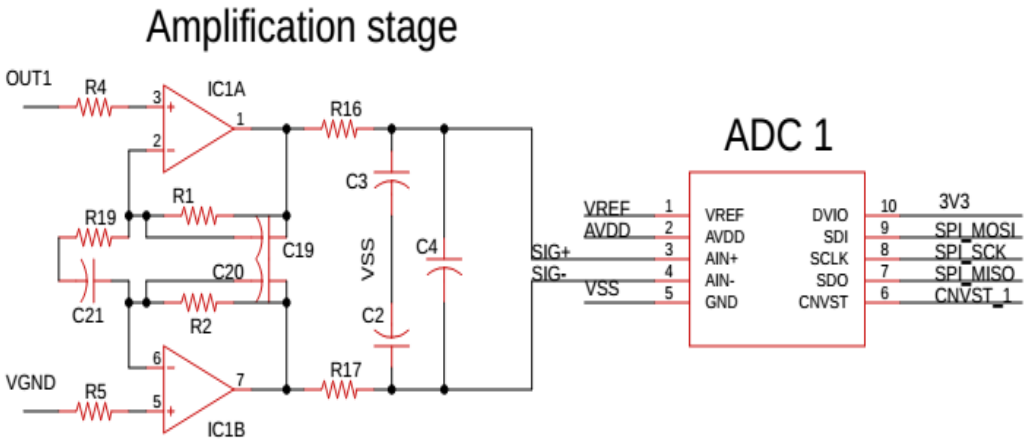

Figure 4.5: The schematic for the gain stage and differential input to ADC. The gain stage provides the necessary gain to the input signal to obtain a workable level.

Equation 4.2 gives the input/output relation of this amplifier configuration:

$$V_{out} = (V_{in+} - V_{in-}) * G \qquad 4.2$$

Where V_{out} is the output of the amplifier, V_{in+} and V_{in-} are the input and reference ground signals, and G is the gain of the amplifier. Equation 4.3 gives the gain of the instrumentation amplifier.

$$G = 1 + \frac{2 * R_1}{R_{19}} \qquad 4.3$$

Here it is assumed that R1 and R2 are equal in magnitude. A gain of 41 is achieved in the actual circuit by setting the resistor values of R1 and R16 to 1kΩ and 20kΩ, respectively. Another important parameter of this circuit is its bandwidth, which depends upon resistor and capacitance values.

$$BW = \frac{1}{2\,\pi\,R\,C}$$

The resonance frequency of the fabricated sensors (type-R2B) is approximately around 17 kHz. The bandwidth should be greater than twice this value. The value of the resistance is adjusted according to the gain required. Therefore, capacitance is

the only other parameter that can adjust the amplifier's bandwidth. The resistor and capacitance values are set to achieve a bandwidth of approximately 60 kHz. This bandwidth value limits the signals that can pass on to ADC and help block high-frequency noise.

The ADC used in this circuit has the following salient features:

Resolution: 16 bit

Mode: Differential

Sampling rate: 1 M samples/sec

Communication: SPI up to 100 Mbps

The literature shows that an ADC with 12 or higher numbers of bits generates very low quantization noise. The differential mode allows the use of virtual ground, which facilitates the DAC operation. The DAC used in this study can generate voltage levels between zero and reference voltage, which is 2.5V in the developed circuit. The drive signals generated by the ADC are added to the virtual ground, which is 1.25V. The swing of the excitation signals is very small and easily comes within the range of the DAC,i.e., 1.25V$\pm$excitation_voltage falls in the 0~2.5V range. Figure 4.6 shows the DAC configuration used in the circuit. The microcontroller controls the DAC through an SPI protocol. The DAC provides sinusoidal excitation signals to the resonators and static voltages to the proof mass and the wafer cap. The proof mass voltage and the wafer cap voltage can be changed at any time using the software. An amplifier stage is present between the DAC and the proof-mass voltage to amplify the DAC output to obtain the desired proof-mass voltage. The amplifier has a gain of 10, allowing it to generate voltage levels up to 25V. Under normal conditions, the proof mass and the wafer cap voltages are set at the sensor's power-up and do not change during the operation. DAC used in this has the following main features.

Resolution: 16 bit

Communication: SPI up to 100 Mbps

Refresh rate: 5µs

Range: 0 ~ V_{REF}

The drive signal magnitude is typically less than 1mV, which equates to a decimal value of 26 (out of 2^{15}) of the DAC, which affects the resolution of the generated signals. Therefore, a higher-value voltage is generated, and then a voltage divider is used to divide that signal to achieve the desired excitation voltage level.

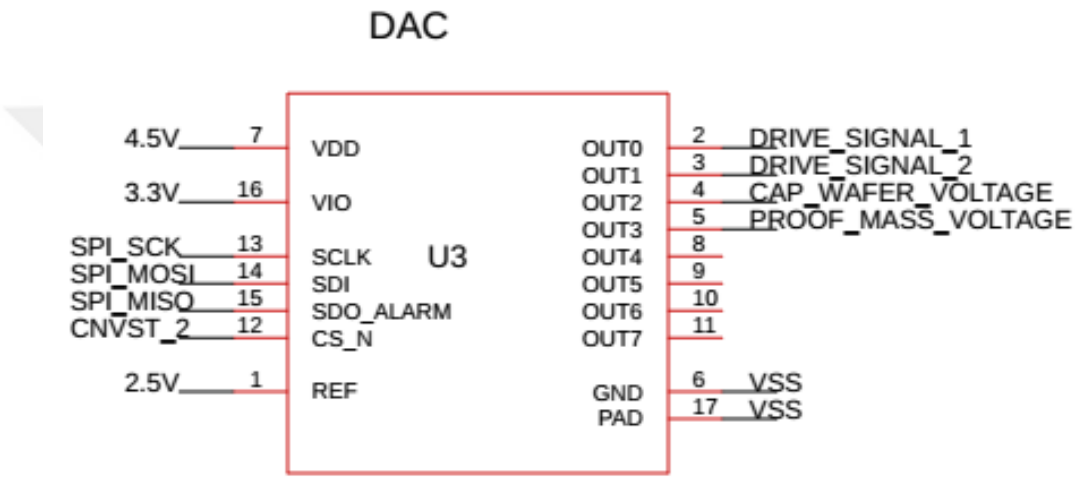

Figure 4.6: The schematic of the DAC, showing its biasing and control signals. Additional amplification stages are present externally where high voltages are required.

The communication between the microcontroller and the ADC/DAC chips is performed using the SPI protocol. The ADC and DAC chips allow up to 100Mbps, but the microcontroller can communicate at 42Mbps. The microcontroller can update the ADC and the DAC chips at 1.3Msps. This speed is higher than the ADC sampling speed and the DAC refresh rate. Therefore, the SPI communication is not a bottleneck for the data sampling from the ADC and drive signal generation.

The digital control loop circuit's most crucial part is the microcontroller. The microcontroller used in this circuit is STM32 from STMicroelectronics. It is a 32-bit microcontroller with 169 MHz speed. Multiple SPI ports control different SPI-based

components like ADC and DAC ICs. In-built CORDIC functions are available to generate a sine wave with minimal processing power. This microcontroller collects data from an ADC, and after processing, drive signals are generated and fed back to the sensor using a DAC. The algorithms that are implemented inside the microcontroller to perform different functionalities are discussed in the last section of this chapter.

Some other peripheral components in the circuit support the main ICs. Microcontroller debugger circuit to program the microcontroller and transmit serial data for logging. Voltage ICs generate different voltage levels required by different ICs. A temperature sensor, placed close to the sensor chip, acquires temperature data. Figure 4.7 shows the PCB with different components present on it.

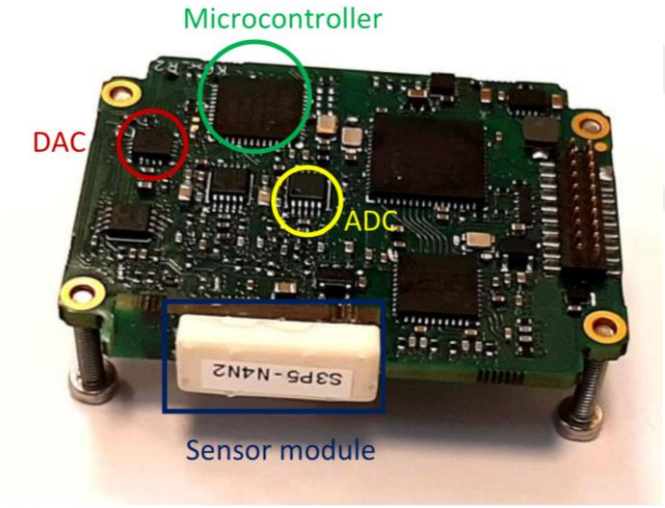

Figure 4.7: Digital control PCB showing different components of the circuit. The readout circuit is compact and suitable for commercial products.

4.3 Noise analysis

The noise in a resonant-based MEMS accelerometer is one of the main parameters determining the performance. The noise in an accelerometer system can be divided into two main categories: mechanical and electrical noise [51-53]. The mechanical

noise results from the Brownian motion of the sensor structure. The electrical noise results from different sources, such as pre-amplifier noise, quantization noise, clock inaccuracy, and mass residual motion noise [51]. The digital control loop implementation has a slightly different noise model than the conventional readout circuit of a resonant MEMS accelerometer. The noise sources due to the automatic gain control (AGC), variable gain amplitude (VGA), PLL, and other peripheral analog circuitry are eliminated in the digital control implementation. On the other hand, some new noise sources, such as quantization noise, clock inaccuracy noise, and PI controller-generated noise, need to be considered. The following sections will explain all noise sources in a digital control loop-based resonant MEMS accelerometer system.

4.3.1 Brownian noise

The following equation shows the equivalent acceleration noise due to the Brownian noise [53]:

$$a_n{}^2 = \frac{4\,K_b\,T\,b}{m^2} \qquad 4.4$$

Where K_b is the Boltzman constant, T is the temperature in Kelvin, b is the damping factor, and m is the mass of the proof mass. The equation shows that the noise is directly proportional to the damping factor of the sensor and inversely proportional to the mass of the sensor structure. The following equation gives the damping factor in terms of resonance frequency:

$$b = \frac{\omega_r\,m}{Q} \qquad 4.5$$

Where w_r is the resonance frequency, and Q is the quality factor of the sensor. The Brownian noise reduces if the mass of the sensor structure increases or the damping factor decreases. The damping factor decreases with a decrease in the resonance frequency or an increase in the quality factor. The value of this noise for a single resonator is calculated as 0.233μg/√Hz using the actual sensor parameters. The

amplification factor of the lever mechanism increases the noise level with a factor of 5, increasing the actual noise value to 1.16µg/√Hz. Since two uncoupled resonators are present in the sensor, the total noise due to the Brownian motion of the resonators equals 1.64µg/√Hz.

4.3.2 Amplifier Input Referred Noise

The pre-amplifier stage is the first stage of the system that significantly affects the noise performance. The input-referred noise of all the later stages has a minimal effect at this stage. The noise propagates back by dividing with the gain of the previous stage. The pre-amplifier stage used in this study has two sources of electrical noise. The first source of noise is the feedback resistor, and the second is the opamp of the pre-amplifier stage. The pre-amplifier output voltage noise is given as [35]:

$$V_{nout}{}^2 = I_n{}^2 \left(\frac{R_b}{R_b C_f s + 1}\right)^2 + V_n{}^2 \left(1 + \frac{R_b C_{in} s}{R_b C_f s + 1}\right)^2 \qquad 4.6$$

Where R_b is the biasing resistance, C_f is the feedback capacitance, I_n is the current noise of the resistor, V_n is the voltage noise of the opamp, and C_{in} is the parasitic input capacitance. The output voltage noise is divided by the gain of the sensor, and the input-referred noise as a current is given as [35]:

$$I_{ninput}{}^2 = \frac{4\,K\,T}{R_b} + V_n{}^2 \left[\frac{1 + s\,R_b(\,C_f + C_{in}\,)}{R_b}\right]^2 \qquad 4.7$$

The input referred noise reduces with an increase in the biasing resistance value. The noise also depends on the feedback capacitor and the parasitic input capacitance. At low frequencies, the noise from the resistor is the dominant noise source.

The input-referred current noise is calculated for the operational amplifier used in the readout circuit using the above equations at the resonance frequency. The value of the input-referred current noise is 5.5fA/√Hz based on the actual parameters of

the readout circuit. There are now three noise components of the pre-amplifier: (1) the input-referred current noise, (2) the current noise of the op-amp at the inverting node, and (3) the voltage noise of the op-amp at the non-inverting node. The output voltage noise resulting from these three sources of the pre-amplifier is calculated to be 192nV/√Hz.

4.3.3 Mass residual motion equivalent PI noise

The digital control loop implementation employs a proportional-integral (PI) controller to keep the reference frequency equal to the resonance frequency of the resonators. Under no external acceleration, the feedback signal applied to the resonators is not constant and oscillates around the mean position, resulting in the oscillation of the proof mass. This proof-mass motion is inseparable from the motion that results from the applied acceleration, resulting in noise generation. This type of noise only exists in closed-loop systems where feedback is continuously updated based on the sensor output [51, 53]. This noise depends on the parameters of the PI controller, which updates the feedback until it reaches the set point value, and the demodulated frequency oscillates around the actual frequency. The input to the PI controller comes from a filter whose fluctuation depends on the filter time constant value. This fluctuation is inevitable and generates a white noise in the demodulated frequency.

4.3.4 Clock jitter noise

The oscillator's frequency that supplies clock frequency to a microcontroller is not 100% accurate. Although very precise oscillators are available, they still have some errors in their accuracy. These oscillators affect the frequency of the reference signals generated by the microcontroller. Therefore, the error in the clock frequency of a microcontroller adds noise to the demodulated frequency. The crystal oscillator

used in this study has a stability of 0.2ppm, and the contribution of this noise is not significant compared to other noise sources.

4.3.5 Quantization noise

The continuous analog signals are converted to the digital domain using an analog-to-digital converter (ADC). The continuous time signals are first converted to discrete-time signals, and then they are quantized. Only a fixed number of voltage steps can be assigned to an input sample called a quantization level. The difference between any two quantization levels is called the quantization step. The quantization noise arises from rounding off the analog voltage to these quantization levels. The range of quantization error due to rounding is limited as per the following equation [54]:

$$-\frac{\Delta}{2} \leq e_q \leq \frac{\Delta}{2}$$

Where Δ is the quantization step, and e_q is the quantization error. For an ADC, the quantization step depends on the number of bits and voltage range:

$$\Delta = \frac{R}{2^b}$$

Where *b* is the number of bits of an ADC, and '*R*' is the input range of an ADC. The term in the denominator denotes the number of quantization levels. The ADC in the circuit used in this study is 16 bits, and its range is 5V (±2.5V). The quantization step of this ADC is 76.294µV.

The following equation gives the mean square power of quantization noise [54]:

$$P_q = \frac{1}{\tau}\int_0^{\tau} {e_q}^2(t)\ dt = \frac{\Delta^2}{12} \qquad 4.8$$

The quality of an ADC output is measured in a term called signal-to-quantization noise ratio [54]:

$$SQNR = \frac{P_{av}}{P_q} = \frac{3}{2}\, 2^{2b} \qquad 4.9$$

This term can be expressed in decibels:

$$SQNR\ (dB) = 1.76 + 6.02\ b \qquad 4.10$$

The signal-to-quantization noise ratio (SQNR) increases with the number of bits of an ADC. For a 16-bit ADC, the SQNR is 98.1dB. However, in actual ADC, the SNR value is much lower than the ideal value. The 16-bit ADC used in this study has an 85 dB SNR as mentioned in its datasheet.

4.3.6 Phase noise

The output of a resonator-based MEMS accelerometer is a frequency signal, which can be defined by Equation 4.11 [55].

$$v(t) = V_0\,[1 + \alpha(t)]\, cos[\omega_0 t + \varphi(t)] \qquad 4.11$$

Where *v(t)* is the output voltage, V_0 is the amplitude of the signal, α is the amplitude fluctuation, ω_0 is the resonance frequency of the signal, and φ is the phase fluctuation. The white noise of an oscillator circuit is equally divided into amplitude noise and phase noise [56, 57]. Leeson's equation defines the phase noise of an oscillator around a carrier frequency. Equation 4.12 gives a simplified version of Leeson's equation, giving phase noise [58].

$$L(\Delta\omega) = 10 \log\left(F\, \frac{2\,K\,T}{{V_0}^2}\, \left(1 + \frac{\omega_0}{2\,Q\,\Delta\omega}\right)^2\right) \qquad 4.12$$

Where Δω is the offset from the carrier frequency, Q is the quality factor of the resonator, and F is an empirical factor related to the noise figure of the resonator. The equation shows that the phase noise is inversely proportional to the quality factor of the resonator, which is the reason for the fabrication of high-Q oscillators. There are two regions in this equation: a flat region showing a frequency-independent white phase noise and the region where phase noise drops as $1/f^2$. This $1/f^2$ noise region decreases very fast with high values of Q. Equation 4.13 shows a Noise-to-Signal

ratio version of Leeson's equation [56-59]. This equation shows that the phase noise of an oscillator circuit can be calculated using the system's signal power and noise power.

$$L(\omega) = 10\log(\frac{Power_{noise}}{Power_{signal}}) \qquad 4.13$$

The quantization of the signals using an ADC also generates phase noise in the system. The phase noise generated due to quantization can be obtained by calculating the noise power of the ADC and the signal power. The general relation is given as Equation 4.14 [57].

$$S_{\varphi,adc}{}^2 = \frac{ADC\ noise\ power}{Full\ scale\ of\ ADC\ power} = \frac{v_{n,adc}{}^2}{0.5 * (V_{FS}/2)^2} \qquad 4.14$$

Where $v_{n,adc}$ is the spot noise of the ADC, and V_{FS} is the full-scale range of the ADC. The noise of the ADC is calculated by dividing the full-scale range by its SNR. The signal power cancels out, leaving only the noise power. Also, the sampling frequency has a direct effect on the noise of the ADC. The SNR of an ADC improves by 3dB by doubling the sampling frequency [60]. The relation for the ADC noise is, therefore, as follows [57]:

$$v_{n,adc}{}^2 = \frac{V_{FS}{}^2}{4 * 10^{\frac{SNR}{10}} f_s} \qquad 4.15$$

Where f_s is the sampling frequency of the ADC, and *SNR* is the signal-to-noise ratio of the ADC in dB. Therefore, Equation 4.14 becomes as follows:

$$S_{\varphi,adc}{}^2 = \frac{10^{-\frac{SNR}{10}}}{0.5\, f_s} \qquad 4.16$$

The phase noise can be converted to the frequency noise as frequency is a derivative of the phase. The following equation gives the frequency equivalent of the phase noise [57]:

$$S_\omega = \frac{10^{-\frac{SNR}{10}}}{0.5\, f_s}\, \Delta\omega^2 \qquad 4.17$$

Where S_ω is the equivalent frequency noise, which can be converted into g's by dividing it by the scale factor of the resonators. The noise added to the system depends upon the sampling frequency of the ADC and the SNR of the system. The increase in the sampling frequency gives a more accurate picture of the input signal. Figure 4.8 shows the effect of SNR and sampling frequency on the sensor's noise performance.

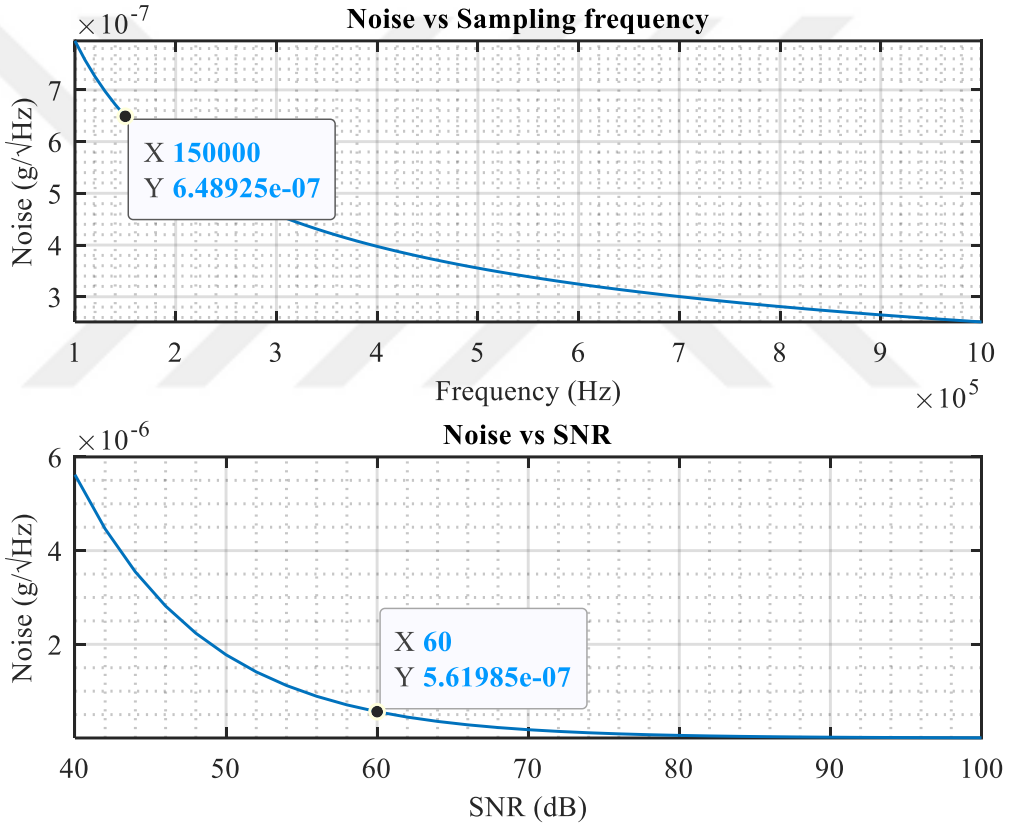

Figure 4.8: The effect of SNR and sampling frequency on quantization noise. The noise performance improves with higher sampling frequency and higher SNR.

The SNR of the ADC used in this implementation, according to its datasheet, is 85dB. However, the calculations suggested by [60] (using ADC noise power,

sampling rate, and noise of input resistance) show that the usable SNR of the ADC is approximately 60dB. This SNR value and the sampling frequency used in this implementation correspond to a frequency noise of 3.6µHz/√Hz. The corresponding noise in g is 36ng/√Hz theoretically.

Figure 4.9 shows different noise sources in the digital control loop-based readout circuit. N_{MEMS} denotes the Brownian noise due to the MEMS structure, N_{TIA} is the input-referred noise of the pre-amplifier stage, N_{QN} is the quantization noise, N_{PID} is the noise due to PI controller parameters, N_{CLOCK} is the noise due to DAC output voltage noise, and N_{CLOCK} is the noise due to inaccuracy of the clock.

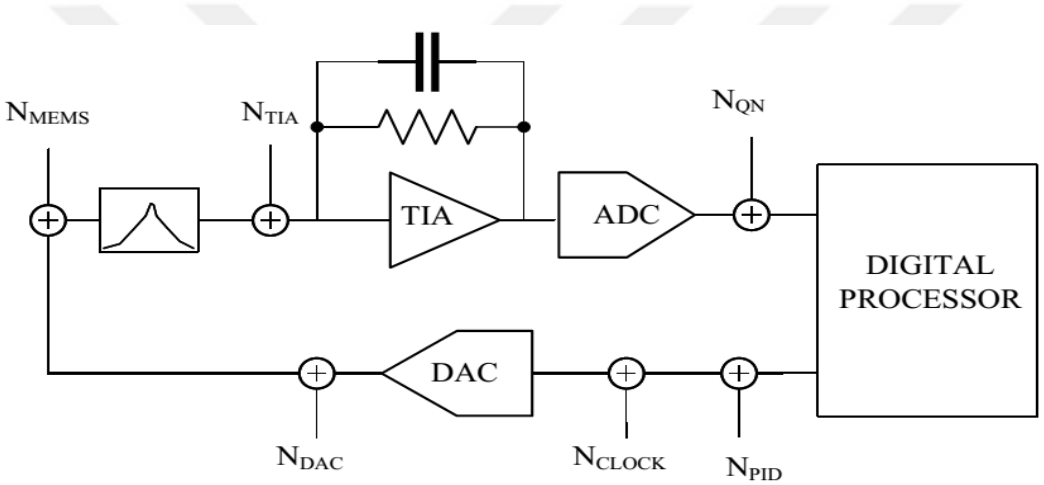

Figure 4.9: The schematic showing noise sources in the digital control implementation.

4.4 Interpretation of noise

Different techniques can analyze the noise present in the data of a frequency source. The noise in a sinusoidal signal is either due to amplitude variations or phase fluctuations. The effect of amplitude is minimal when compared to the effect of phase noise. The instantaneous frequency is the phase derivative, as shown in Equation 4.18.

$$f(t) = f_0 + \frac{1}{2\pi}\frac{d\emptyset}{dt} \qquad 4.18$$

Where *f(t)* is the measured frequency, f_0 is the noise-free frequency, and Ø is the phase noise in the signal. The power-law noise model shows different slopes of power spectral density (PSD) corresponding to different noise sources. PSD of phase noise, frequency noise, or relative-frequency noise use the power-law noise model to show different types of noise sources in the data. Another method to analyze the data in the time domain is plotting the Allan Variance curve [61]. Different slope regions in the Allan Variance plot correspond to different noise sources. Figure 4.10 shows different regions of the Allan variance plot corresponding to different noise types.

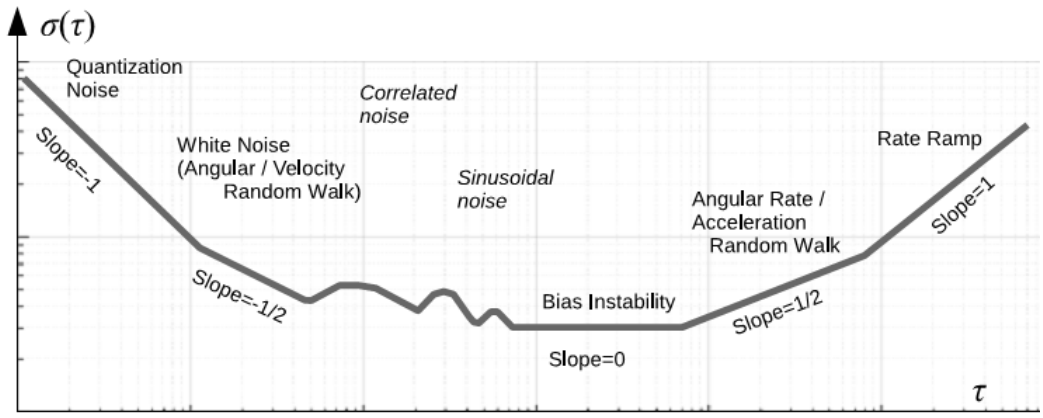

Figure 4.10: Interpretation of noise from the Allan Variance plot [61].

1) Quantization Noise

The quantization noise is the effect of converting the analog data to the digital domain and losing the information due to a finite step size of an ADC. The -1 slope in the Allan variance plot corresponds to the quantization noise present in the accelerometer data.

2) Velocity/Angle Random Walk

The velocity random walk (VRW) applies to an accelerometer, and the angle random walk (ARW) to the gyroscope data. The VRW comprises the high-frequency noise terms of the data. This type of noise has a slope of -1/2 at the left-most part of the Allan Variance plot. The -1/2 slope line passing through T=1 corresponds to the VRW co-efficient.

3) Bias Instability

The flat region with zero slope corresponds to the bias instability of the frequency data. Another term for bias instability is flicker noise. This noise arises from low-frequency fluctuations in the data resulting from different factors.

4) Acceleration/Rate Random Walk (ARW/RRW)

The +1/2 slope on the right side of the Allan Variance plot corresponds to the ARW. The ARW shows the long-term stability of the sensor. One known source of the ARW is the dependency of the sensor data on temperature. The ARW co-efficient is calculated from the Allan variance plot at T=3.

5) Rate Ramp

Rate Ramp (RR) is a deterministic type of error with a +1 slope in the Allan Variance plot. It represents the slow changes that occur over a long period. The co-efficient of the RR is present at T= $\sqrt{2}$.

Figure 4.11 shows the Allan Variance plot of the data obtained from the N4N2 sensor using the lock-in-amplifier. A line with slope -1 fits the Allan Variance plot indicating quantization noise in the data.

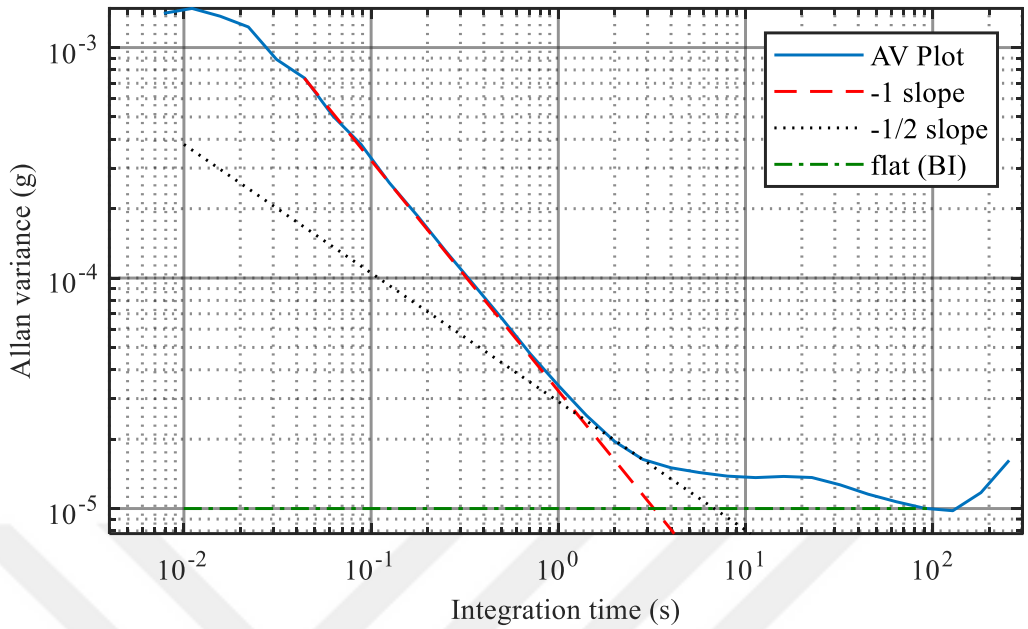

Figure 4.11: Allan Variance plot of data obtained from N4N2 using lock-in-amplifier showing -1 slope, representing the quantization noise present in the data. The bias instability value is 10µg, and the noise value is around 34µg/√Hz.

4.5 SIMULINK Model and Simulation

The control loop implementation can be simulated in MATLAB using a Simulink model. Synchronous demodulation extracts frequency information, and the rectification method obtains amplitude data. The resonator is modeled based on experimental data obtained from the sensor characterization presented in Chapter 3. This section discusses different essential blocks of the Simulink model: the resonator, the sampling of data, amplitude stabilization, frequency tracking, reference signal generation, and incorporation of microcontroller parameters. Figure 4.13 shows the complete Simulink model for a single resonator of a resonant MEMS accelerometer. A simpler block diagram of this Simulink model is shown in Figure 4.13 for easy understanding of the Simulink model.

a) Resonator

The transfer function of the resonator using the mass-spring-damper model is given by Equation 4.19.

$$\frac{X(s)}{F(S)} = A * \frac{1}{m\left(s^2 + \frac{\omega}{Q}\, s + \omega^2\right)} \qquad 4.19$$

Where m is the mass of the resonator/spring, ω is the resonator's resonance frequency, A is the DC gain depending on the proof-mass voltage and the rate of capacitance change with respect to displacement, and Q is the resonator's quality factor. X is the displacement as a result of input force F. The gain, quality factor, and resonance frequency are taken from resonant MEMS accelerometer sensor characterization data. Figure 4.14 gives a bode plot of the resonator model, which shows the resonance frequency at the desired value of 16700Hz.

b) Time delay and sampling

The Simulink model uses time delays at different points of the model. These time delay and hold blocks simulate signals' discrete nature and sampling. In the actual microcontroller-based implementation, data from the input signal is sampled using an ADC. The data is converted to the digital domain after passing through an ADC. The delay and hold block simulates this sampling functionality by holding an input for a fixed time. The hold and delay times are set according to the actual sampling rate implemented in the microcontroller. A discrete conversion block is used to quantize the discrete data. After these blocks, the data is in a 16-bits format that exactly matches the data acquired by a microcontroller. The sampling rate implemented in the microcontroller and the model is approximately 147ksps.

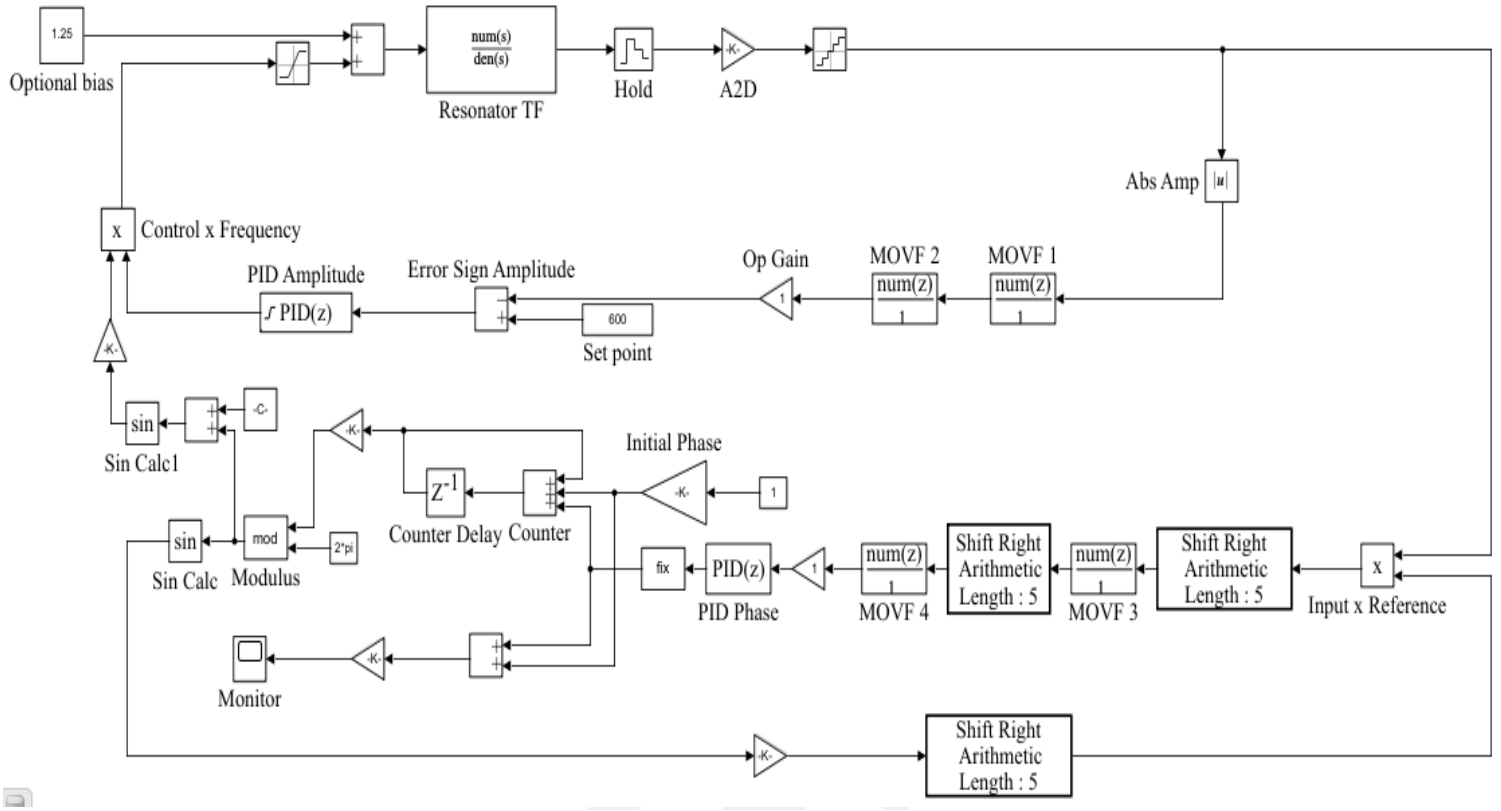

Figure 4.12: Simulink model of a resonator of a resonant MEMS accelerometer with amplitude and frequency control, employing the real sensor parameters and microcontroller environment.

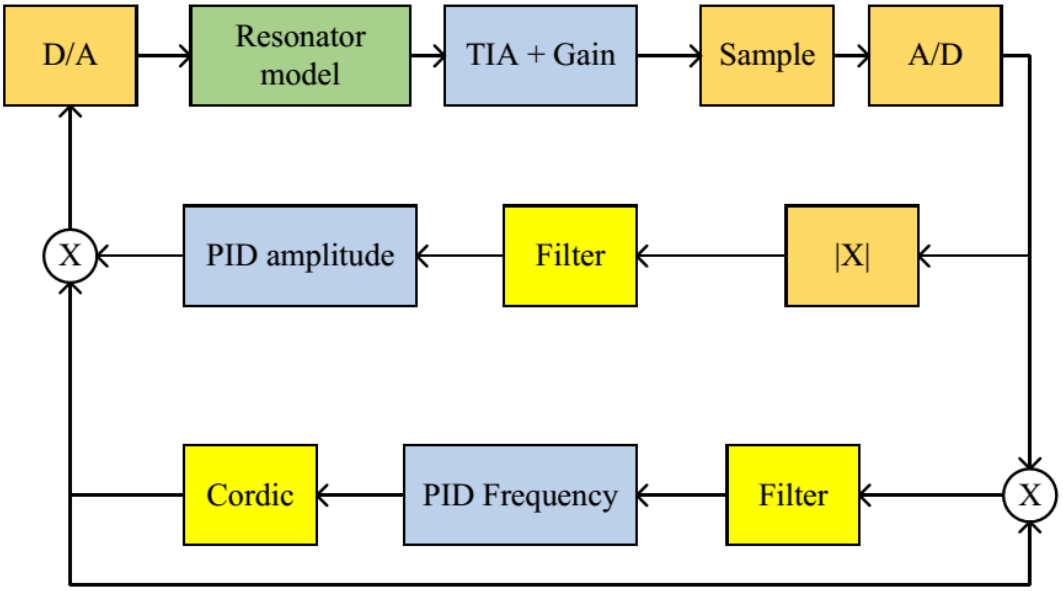

Figure 4.13: A simplified block diagram of the Simulink model showing only the main functionalities.

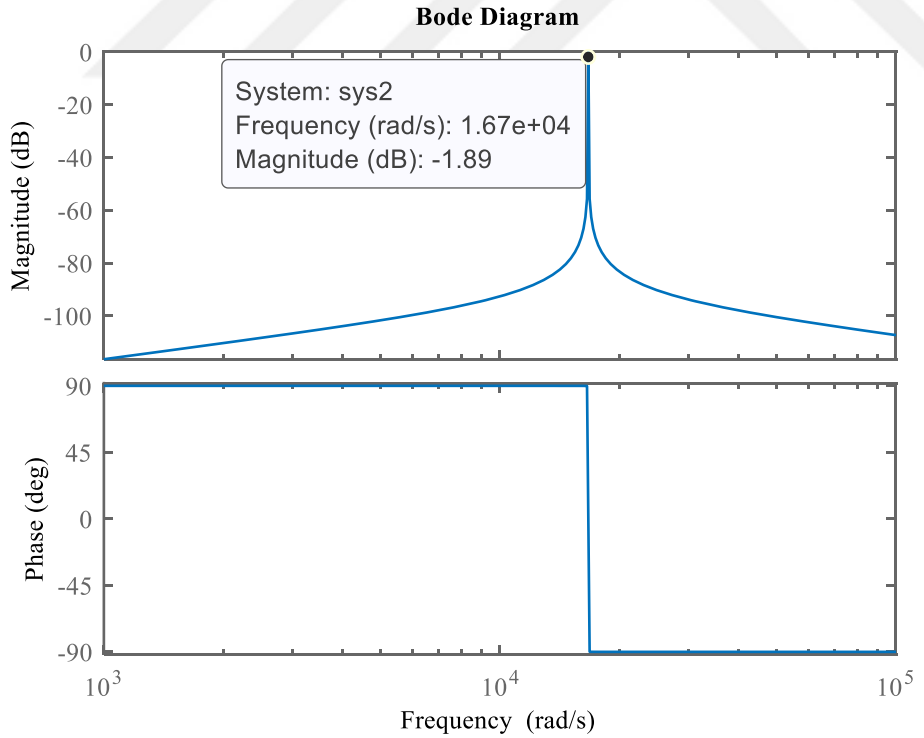

Figure 4.14: The Bode plot of the Simulink resonator model showing resonance frequency at the value determined by the model parameters.

Figure 4.15 shows the analog signal conversion to the digital domain in the Simulink model.

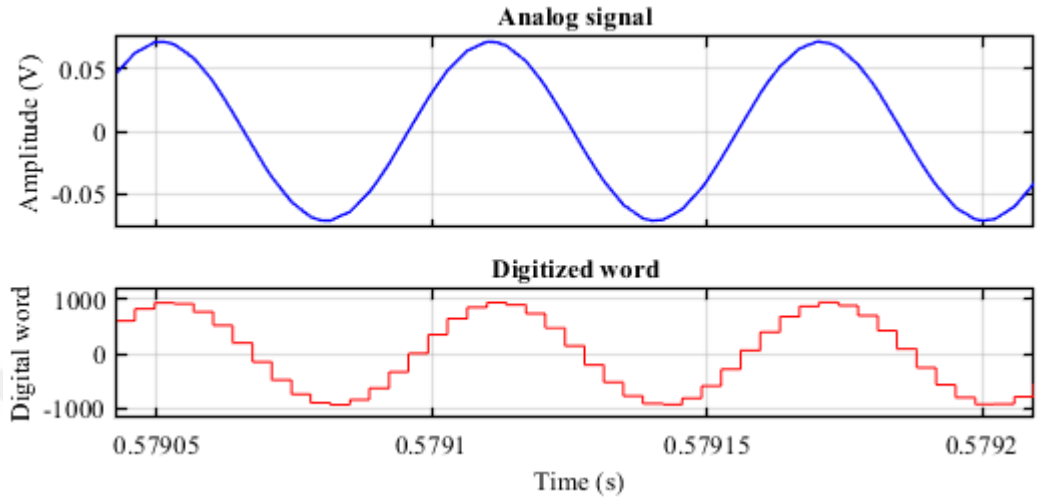

Figure 4.15: The conversion of the analog-to-digital domain of the resonator output signal (16700Hz) in the Simulink model with a sampling rate of 147kHz to emulate the actual microcontroller implementation.

c) Amplitude stabilization loop

Two loops work in parallel for amplitude and frequency control. The first loop controls the amplitude of the resonator output. This loop implements a wave rectification method to extract the signal's amplitude. The rectification method is used because of its simple implementation in the digital domain. In this method, a block obtains the absolute value of all the incoming samples. Low pass filtering is implemented in the Simulink model to extract the amplitude information. The output of the low-pass filter is directly proportional to the amplitude of the input signal. The time constant of the low pass filter determines the speed and accuracy of amplitude stabilization. The second component of this first loop is a PI controller that compares the signal amplitude with a setpoint value. The PI controller generates a control word that determines the amplitude of the drive signal to achieve the setpoint amplitude value. Figure 4.16 shows the effect of filter length on the convergence speed to the

set point amplitude value. The filter is implemented as two cascaded filters. The first plot has a filter with a length of 32x32 taps, and the second plot has a 128x128 length filter. The filter with a smaller length is faster than the other one. However, this filter is also noisier compared to the larger filter. There is a trade-off between the speed and accuracy of the amplitude stabilization filter. A slow filter implementation is more stable and accurate.

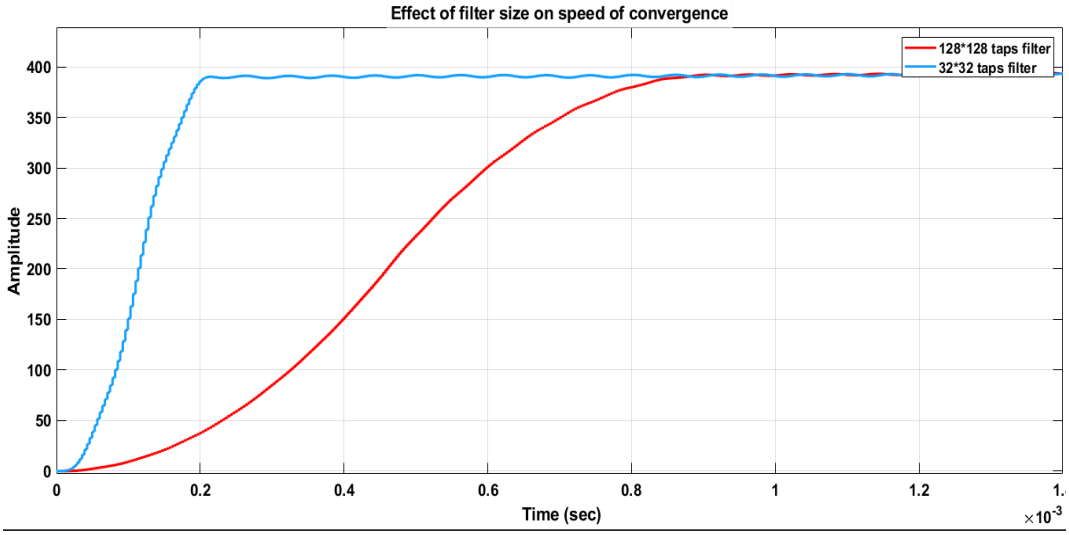

Figure 4.16: The effect of filter length on the amplitude stabilization speed of convergence.

d) Frequency tracking loop

The second loop that operates in parallel with amplitude stabilization is the frequency tracking loop. This loop reads the input signal and multiplies it with a reference signal, and the product passes through a low-pass filter. The output of the low pass filter is zero if the input signal and the reference signal are 90° phase-shifted. A PI controller compares the filter output with zero and generates a control word. The control word goes to another block that generates the reference frequency. The reference frequency corrects itself until the output of the demodulation filter is zero. This point indicates that the reference frequency is equal to the frequency coming from the resonator. Two blocks control the speed of convergence of the frequency

tracking. The first block is the filter that takes the average of the product of the input and the reference signal, and the second factor that controls the speed of the system is the values of the *P* and *I* parameters of the PI controller. High values of PI give a swift response, and low values give a slow response. Again, there is a trade-off between the speed and the noise performance of the system. A fast system is noisier than a slow system. The PI parameters are selected such that it meets the speed and performance criteria at the same time.

e) Fixed-point arithmetic operations

The microcontroller performs 32-bit operations, with all calculations in fixed-point numbers. The Q1.31 format is used in the microcontroller, in which the first bit indicates the sign of a number, and the remaining 31 bits give the value of the fraction part of a number. The CORDIC functions in the microcontroller have Q1.31 format as input and output. Therefore, all other calculations are performed in the fixed-point numbers to avoid conversion from fixed-point to decimal and vice versa. The Simulink model performs all the calculations in Q1.31 format. The floating-point numbers are converted to fixed-point numbers and used in all the calculations.

A knob control is present in the Simulink model to change the resonance frequency value during simulation to test the frequency-tracking capability of the algorithm.

Figure 4.17 shows a simulation result where the Simulink model tracks the changes applied to the resonance frequency during the simulation. The noise sources calculated in the previous section are added to the Simulink model to observe the effect of noise. The noise due to clock inaccuracy is not a dominant noise source. Therefore, the new model does not use this noise source. The Brownian and the pre-amplifier noise are added to the model. A simulation result for frequency tracking is shown in Figure 4.18. The fluctuation in the demodulated frequency increases five times with the addition of noise in the model compared to a noise-free Simulink model

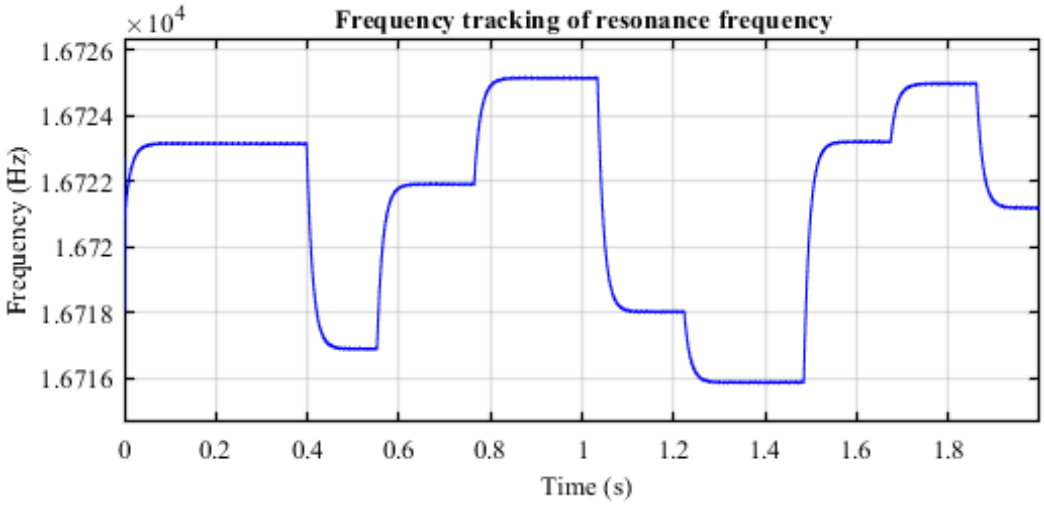

Figure 4.17: The simulation of the frequency tracking algorithm implemented in Simulink. The algorithm successfully follows the resonance frequency when it is modified during the simulation.

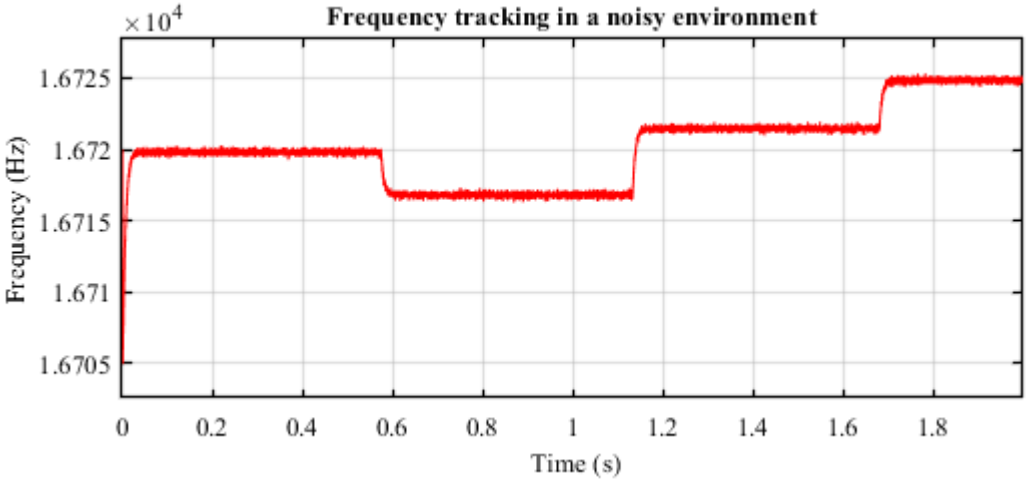

Figure 4.18: Simulation of frequency tracking algorithm with noise sources added in the Simulink model. The fluctuation in the demodulated frequency increases 5 times compared to the noise-free model.

4.6 Closed loop implementation

The microcontroller is at the center of the digital closed loop as it collects data from the sensor and generates a drive signal after processing. The pre-amplifier stage

creates a 90° phase shift in the signal. Thus, there is a 90° phase difference between the input to ADC and the signal generated by the DAC. This phase shift is used to track the resonance frequency. Let S_i denote the signal input to ADC, and S_d denote the generated drive signal.

$$S_d = A_d \cos(\theta_d) \quad 4.20$$

$$S_i = A_i \cos(\theta_i + \emptyset) \quad 4.21$$

The two signals are multiplied by each other.

$$M = S_d * S_i = A_M \cos(\theta_d + \theta_i + \emptyset) + A_M \cos(\theta_d - \theta_i - \emptyset) \quad 4.22$$

This data is passed through a low-pass filter. The high-frequency components are suppressed, and the remaining terms are shown in the following equation.

$$M = A_M \cos(\theta_d - \theta_i - \emptyset) \quad 4.23$$

The control loop is timed so that the ADC reads a 90-degree phase-shifted version of the reference signal. For this low-frequency term to go completely to zero, the angle of both signals should be nearly equal. These angles are directly proportional to the input frequency and the generated frequency. When this low-frequency term is passed through a PI controller, with the set-point equal to zero, the generated frequency follows the resonator's resonance frequency.

This technique is different from the conventional methods, where in-phase and quadrature components are used to calculate the phase of the input signals. The requirement to calculate the quadrature components is eliminated. Figure 4.19 shows the block diagram of the timed reference-based frequency tracking algorithm. This reduction significantly reduces the processing power required in digital implementation. The amplitude information is extracted from the input data and maintained at a set point value using a PI controller. The absolute value of the input signal is averaged using a low-pass filter. This averaged value is compared to the set point value, and PI generates an amplitude control signal. The set point is selected based on sensor characterization data such that the sensor operates in the linear region.

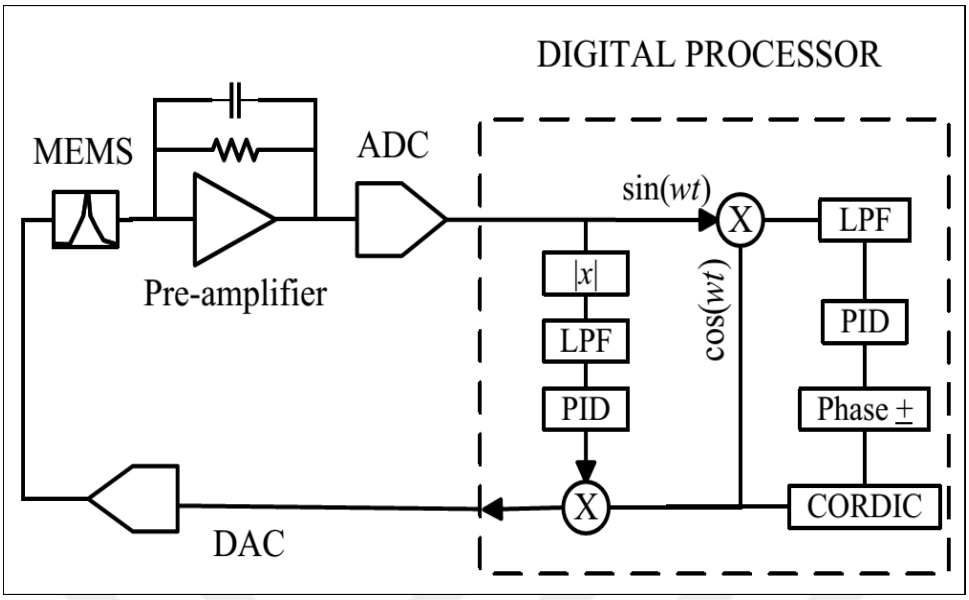

Figure 4.19: The amplitude extraction and frequency tracking implementation in the digital domain using the timed reference signal.

Table 4.1 compares the computations required for implementing the timed reference-based frequency tracking algorithm with the conventional method used in the literature [42, 43]. The timed reference technique uses fewer computations compared to the conventional method.

Table 4.1: Summary of computations used in the digital domain for frequency tracking, showing that the number of blocks and computational power used in this study is significantly less than the other studies.

Implementation	**CORDIC based**	**[42]***	**[43]****	**This work**
Floating point multiplications	2	2	2	1
Filters	2	2	3	1
CORDIC operations	3	2	2	1
PI Controller	1	2	1	1
NCO	1	2	1	1

*Additional processing units. Amplitude tracking was performed.

**Additional processing unit is also present for phase compensation. Amplitude stabilization is missing.

4.6.1 Implementation of Moving Average Filter

The moving average filter (MAF) is a type of Finite Impulse Response (FIR) filter with all coefficients equal. The general relation for the MAF is given below:

$$y(n) = \sum_{k=0}^{N} b\, x(k) \qquad 4.24$$

Where *x* is the input to the filter, *y* is the output, *N* is the number of taps, and *b* is the co-efficient of the filter. The value of *b* for all the terms is generally the same and equal to *1/N*. The z-transform of this equation is given as follows:

$$H(z) = b \sum_{k=0}^{N} z^{-k} \qquad 4.25$$

Another way to represent the frequency response of the MAF is given as follows:

$$H(\omega) = b * \frac{1 - e^{-j\,\omega\,N}}{1 - e^{-j\,\omega}} \qquad 4.26$$

The MAF used in this implementation has 1024 taps, and its magnitude response is shown in Figure 4.20. The MAF is implemented as a power of 2 so that the division operation can be replaced with a shift operation. The following recursive equation is used to simplify the computations further.

$$y(n) = y(n-1) + b\left(x(n) - x(n-M)\right) \qquad 4.27$$

This approach makes the moving average implementation computationally simple and fast. For each cycle, only three simple operations are performed: (1) one addition of new samples, (2) subtraction of the oldest sample, and (3) right shift to perform the division operation.

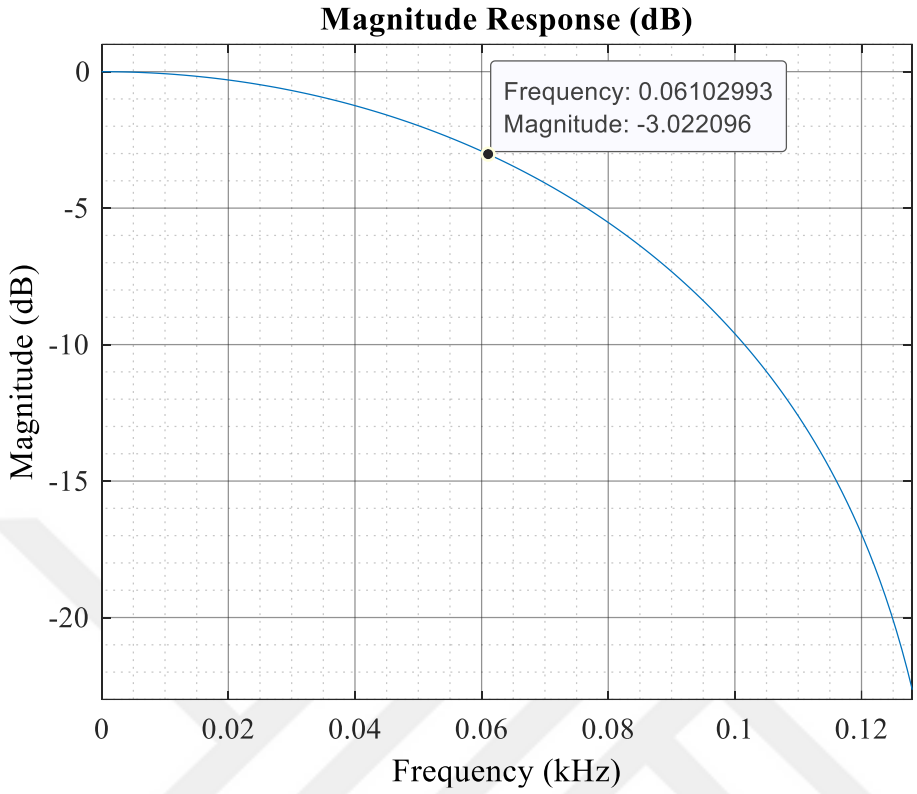

Figure 4.20: The magnitude response of the moving average filter implemented in the microcontroller with 1024 taps. The -3dB frequency is approximately 60Hz.

4.6.2 Control loop design

There are different components in the control loop of the digital control loop implementation, namely the resonator, the pre-amplifier, the loop filter, the PI controller, and the demodulation gain. Each component has its transfer function and affects the overall bandwidth of the closed-loop system. Equation 4.28 gives the transfer function of the resonator.

$$M(s) = \eta^2 V^2 \frac{s}{m\left(s^2 + {\omega_0}/{Q}\, s + {\omega_0}^2\right)} \qquad 4.28$$

Where η is the conversion coefficient (depends upon the sensor parameters), V is the proof-mass voltage, ω_0 is the resonance frequency, and Q is the quality factor of the

resonator. Equation 4.29 gives the transfer function of the pre-amplifier used in this digital control implementation.

$$A(s) = \frac{R}{1 + s\,R\,C} \qquad 4.29$$

Where R is the feedback resistance and C is the feedback capacitance of the circuit. Equation 4.30 gives the transfer function of the low-pass filter, where ω_c is the cut-off frequency of the low-pass filter.

$$L(s) = \frac{{\omega_c}^2}{s^2 + 2\,\omega_c\,s + {\omega_c}^2} \qquad 4.30$$

Equation 4.31 gives the transfer function of the PI controller implemented in the microcontroller.

$$P(s) = \frac{K_I + s\,K_P}{s} \qquad 4.31$$

Where K_I is the coefficient of the integral parameter and K_P is the coefficient of the proportional parameter of the PI controller. The closed-loop transfer function of the resonator can be written as Equation .4.32

$$H(s) = \frac{L(s)M(s)A(s)P(s)K_m}{1 + L(s)M(s)A(s)P(s)K_m} \qquad 4.32$$

The constant K_m stands for the gain of the demodulation. The actual parameters from the microcontroller implementation are inducted in this equation, and MATLAB is used to simplify the obtained relation. Figure 4.21 shows the bode plot of this closed-loop system with a -3dB frequency equal to approximately 66.8Hz.

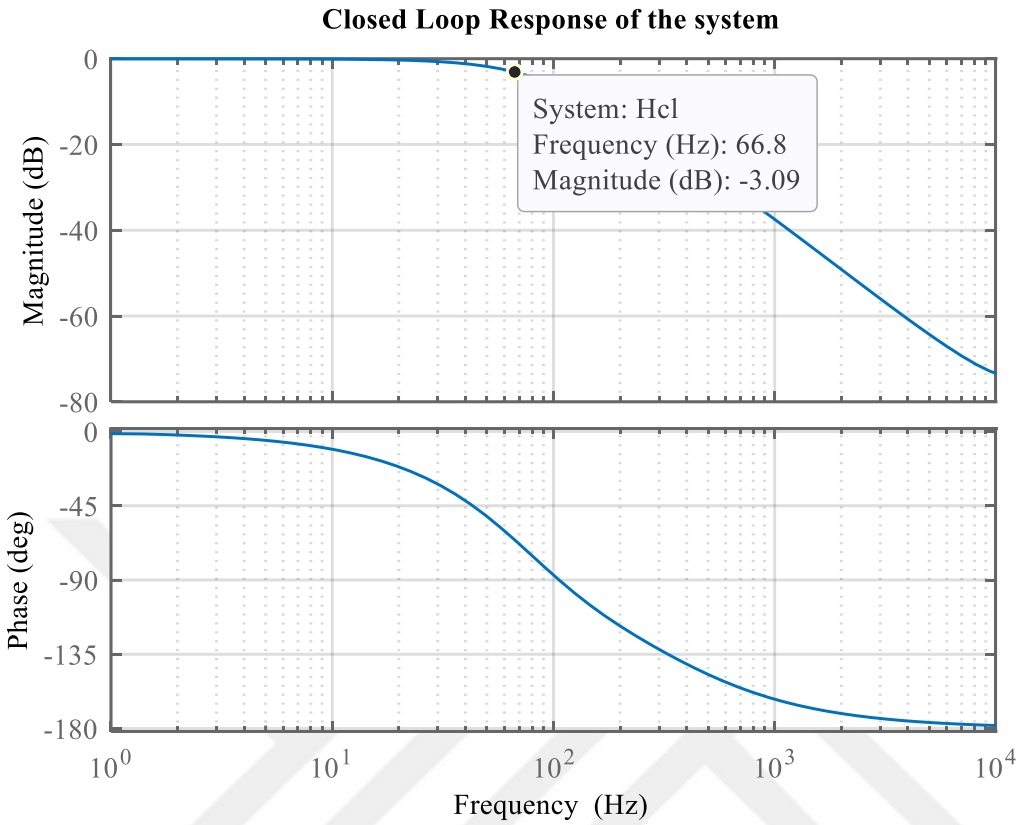

Figure 4.21: The bode plot of the closed-loop system of the sensor shows a system bandwidth of approximately 66.8Hz.

4.6.3 Frequency reading resolution of the developed readout circuit

The frequency reading resolution of the developed digital control loop-based readout circuit is calculated by measuring the sine wave generated with different accurate sources. The sine wave is generated by a Dynamic Signal Analyzer (DSA – 35670A Keysight Technologies), Zurich Lock-in-Amplifier (HF2L), and a Signal Generator (TGF4042), and the digital control readout circuit measures the frequency of the generated sine wave. Table 4.2 gives the critical specifications of the signal generators available in their datasheets. The signal generator has a frequency resolution of 1µHz and a sampling rate of 400MSa/s. However, it has a sine wave amplitude accuracy of 1.5% and a DC offset amplitude accuracy of 1%. A DC offset

of 1.25V is used in these tests to make the signals compatible with the digital readout circuit. The lock-in-amplifier has a demodulation frequency resolution of 0.7µHz and a sampling rate of 210MSa/s. The frequency resolution of the generated signal is not given in its datasheets, but it can be assumed that it must be close to the 0.7µHz value. The DSA has a frequency reading resolution of 61µHz, and it is assumed that the frequency generation is performed with a similar resolution.

Table 4.2: Specifications of the signal generators.

Device	Specifications
Signal Generator (TGF4042)	Resolution: 1µHz THD 0.05% 400MSa/s Sine amplitude accuracy: 1.5% DC Offset accuracy: 1%
Lock-in-Amplifier (HF2L)	210MSa/s Demodulated frequency resolution: 0.7µHz 64-bit data
Dynamic Signal Analyzer (35670A)	Sine amplitude accuracy: 4% Frequency reading resolution: 61µHz

The value of generated frequency for DSA and the signal generator is 16700Hz, and the value of generated frequency by the lock-in-amplifier is 16647Hz. Figure 4.22 shows the setup for connecting the digital readout circuit with the dynamic signal analyzer and the signal generator. The data is transferred to the computer using a serial port at 1 msec. The difference between this and the actual configuration (sensor + digital readout circuit) is that a sine source replaces the sensor plus the pre-amplifier stage. The circuit reads the frequency of a fixed sine source in contrast to the frequency output of the sensor resonator.

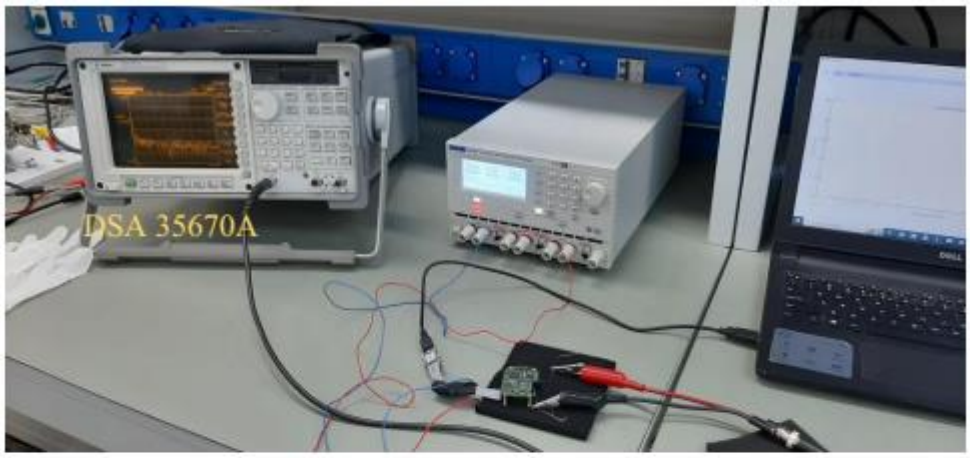

(a)

(b)

Figure 4.22: The setup for frequency reading from the signal generators (a) Dynamic Sıgnal Analyzer (DSA 35670A) (b) Signal Generator (TGF4042)

Figure 4.23 gives the Allan variance plot of the frequency data acquired from the signal generators. The minimum (of the three devices) frequency resolution measured at one second time is approximately 16.1µHz. The differential resolution is approximately 22.6µHz. Using the scale factor of the sensor, the expected white noise in the sensor data is approximately 0.23µg/√Hz, which is the minimum achievable noise level using this digital readout circuit.

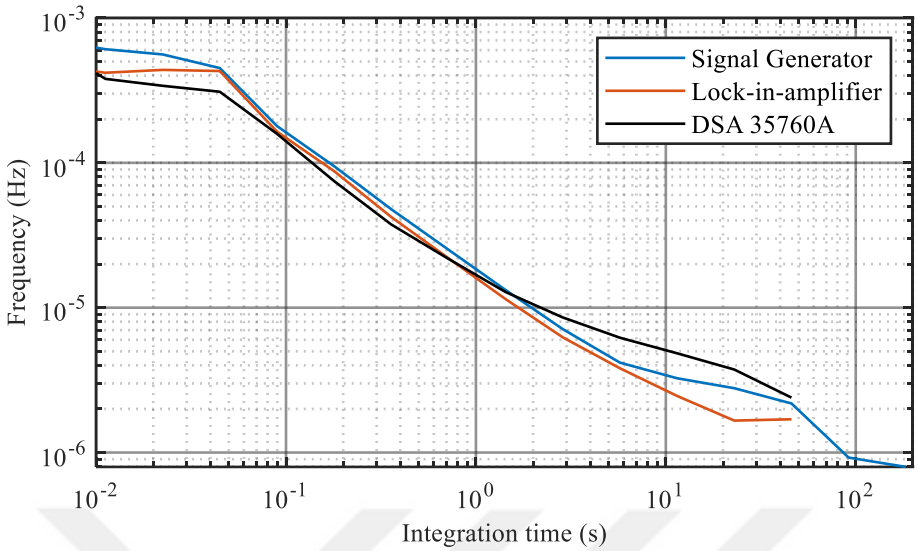

Figure 4.23: The Allan variance plot of data collected using three different signal generators. The frequency resolution is approximately 18.6µHz, 16.1µHz, and 16.9µHz for the signal generator, lock-in-amplifier, and the DSA, respectively.

4.6.4 Frequency step change response

The bandwidth of frequency reading is measured using the frequency generator (TFG4042). The frequency signal is changed instantly, and the response of the frequency tracking of the readout circuit is observed. The frequency step is changed with different magnitudes; 10Hz, 20Hz, 40Hz, 50Hz, 80Hz, and 100Hz. The digital readout circuit can track the frequency change in approximately less than 20 msec. Figure 4.24 shows the response of the digital control circuit's frequency tracking under different frequency steps. Frequency steps larger than 100Hz are also applied to the circuit, but it took longer to reach that step change. In the actual scenario, such a step change in the frequency corresponds to a shock. Frequency steps corresponding to more than 100g of shock are also applied to this circuit. The circuit fails to follow that high frequency but tracks the frequency as soon as it returns to its nominal value.

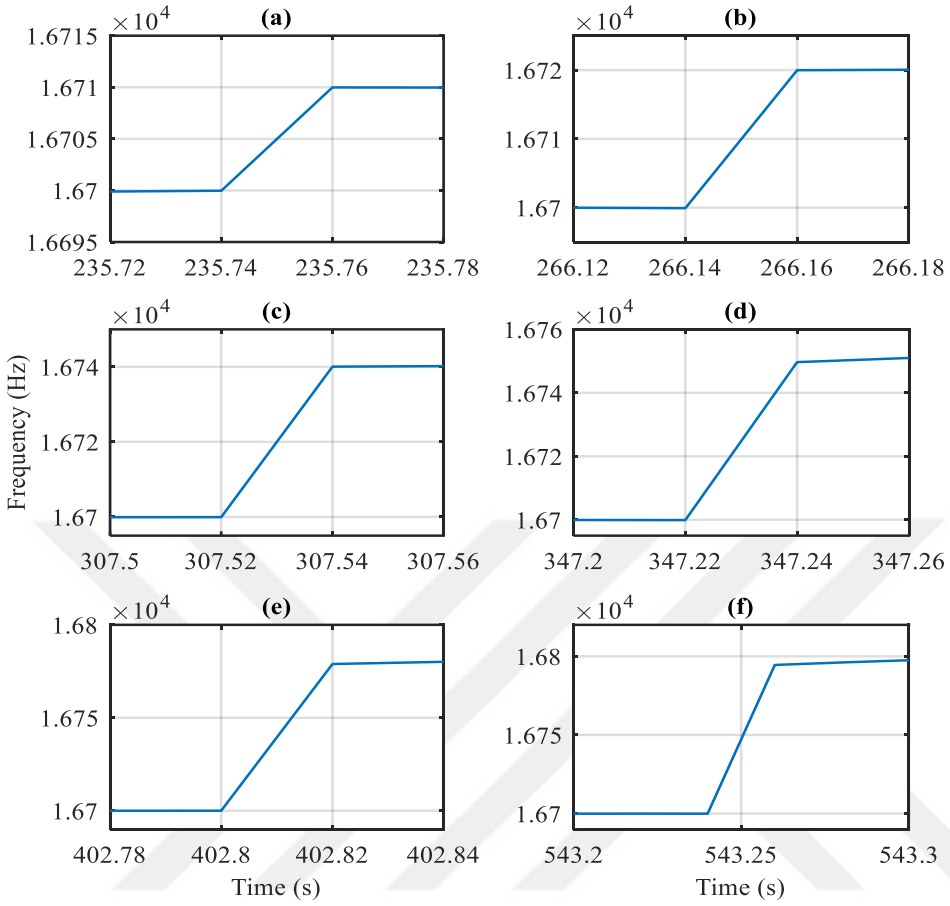

Figure 4.24: The frequency tracking speed of the digital readout circuit to a frequency step change (a) 10Hz (b) 20Hz (c) 40Hz (d) 50Hz (e) 80 Hz (f) 100Hz. The bandwidth of frequency tracking is almost 50Hz.

4.6.5 Effect of input on bandwidth

The bandwidth of a digital accelerometer can be defined in various ways. Commercial manufacturers define a digital sensor's bandwidth as half the sensor's output data rate [62]. From this perspective, the bandwidth of the proposed system is limited by the output data rate (ODR) of the microcontroller. The bandwidth is increased with an increase in the ODR. However, this is only true when the control loop of the sensor can achieve the ODR/2 bandwidth.

In the last section, the frequency tracking of the digital readout circuit is tested when a step frequency change is applied using a frequency generator. The frequency change of 100Hz is tracked in 20ms with the developed readout circuit. This frequency range corresponds to a ±2g acceleration. The current settings of the readout circuit do not detect very high values of step changes in the frequency. In another test, by modifying the parameters of the PI controller, a step change of 300Hz (equivalent to ±6g acceleration) is correctly followed by the readout circuit, but the white noise increases.

The input frequency range is also tested with the digital readout circuit. The circuit is used to read frequency over a different range of frequencies (5kHz, 10kHz, 15kHz, and 20kHz). Figure 4.25 shows the frequency tracking capability of the readout circuit at different values of input frequency. The results show that the readout circuit works efficiently over this extensive range of frequencies.

The Simulink model is used to observe the frequency tracking at different values of changes in the frequency shown in Figure 4.26. It is observed from the simulation data that the time to reach a stable frequency value increases with an increase in the frequency step size. The figure shows that the 1Hz frequency change is tracked in 100ms, whereas the 40Hz frequency change is tracked in 1.5s. This implies that the bandwidth of the readout circuit, in terms of frequency tracking, reduces with an increase in the step change in the input frequency.

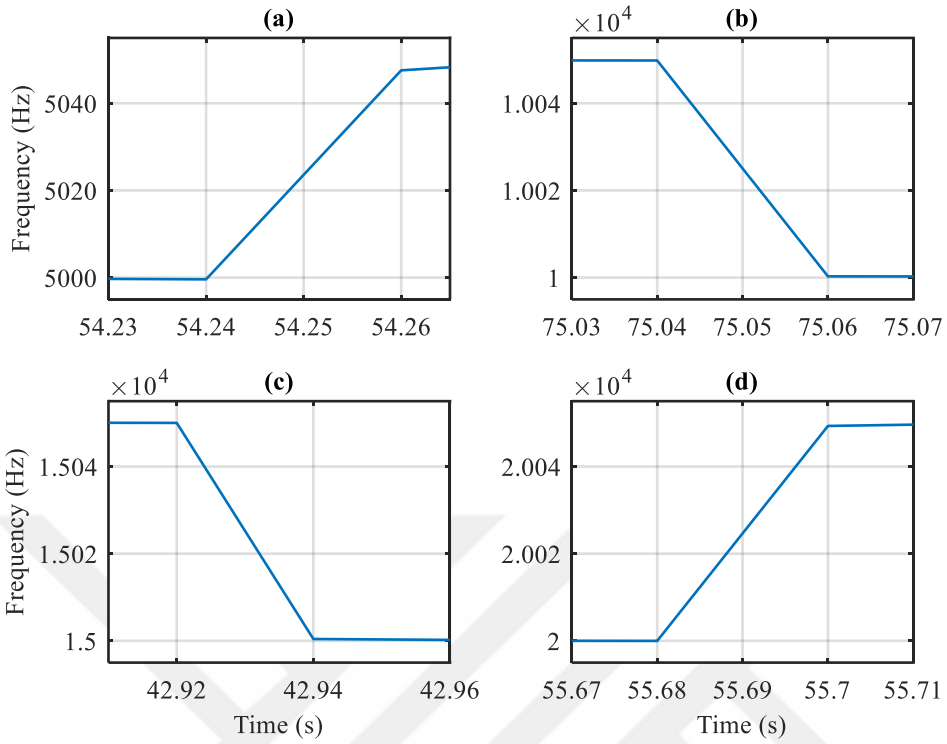

Figure 4.25: The frequency tracking capability of the readout circuit at different values of resonance frequencies: (a) 5kHz, (b) 10kHz, (c) 15kHz, and (d) 20kHz.

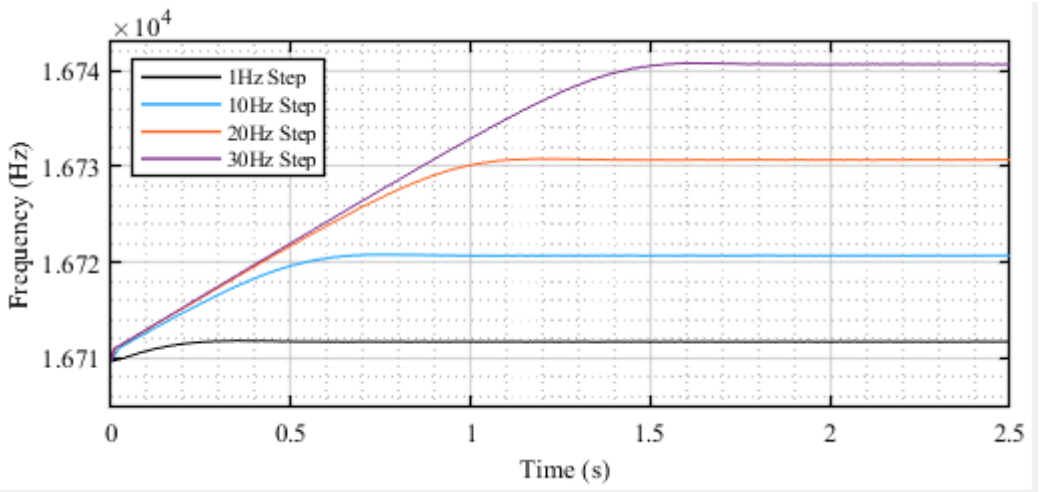

Figure 4.26: The frequency tracking at different frequency steps applied to the Simulink model. The time to reach the set frequency increases with an increase in the step size of the frequency.

4.7 Algorithms for microcontroller

The microcontroller performs different tasks to close the loop and operate two resonators of a resonant MEMS accelerometer. Various algorithms are programmed in the microcontroller to perform different functions. Some of these algorithms run in parallel, and some work in standalone mode. These algorithms include frequency sweeping, amplitude stabilization, frequency tracking, temperature compensation, and serial data transmission. Each of the mentioned functionality can be performed using different methods. These methods have different advantages and drawbacks when compared to each other. Two main parameters determining the efficiency of a method are speed and performance. The performance of the control loop depends on the performance of these functionalities. However, the processing power of a digital controller is limited. It is not practical to employ too many algorithms to improve sensor performance.

Similarly, algorithms that require complex calculations are also not suitable for implementation in a digital processor. Additionally, the time required to complete these tasks is short. For example, the time between two interrupts implemented in the microcontroller is 1.75µs. The method that completes the required functionalities within that time is preferred in the code. Therefore, it is very critical to use methods that employ minimal processing power of the digital processor.

4.7.1 Sine wave generation

There are different methods to generate a sine wave using a microcontroller. Look up table can be used, or sine values can be calculated using sine functions in a microcontroller. The microcontroller used in this study has built-in CORDIC support that quickly calculates sine and cosine without much processing power. Phase is incremented at every iteration and sent to the CORDIC function. The theory of this method is explained briefly here.

$$Oscillating\ frequency = f_o$$

$$Sampling\ frequency = f_s$$

$$Phase\ increment, \emptyset = 2\,\pi\,\frac{f_o}{f_s} \qquad 4.33$$

In this equation, only oscillating frequency is variable and determines the phase increment value. The sampling frequency is a controllable variable. The phase increment value also determines the number of samples in one input signal cycle. This phase increment value is added to the phase input of the CORDIC function available in the microcontroller. Figure 4.27 shows the implementation of this method in MATLAB with actual values.

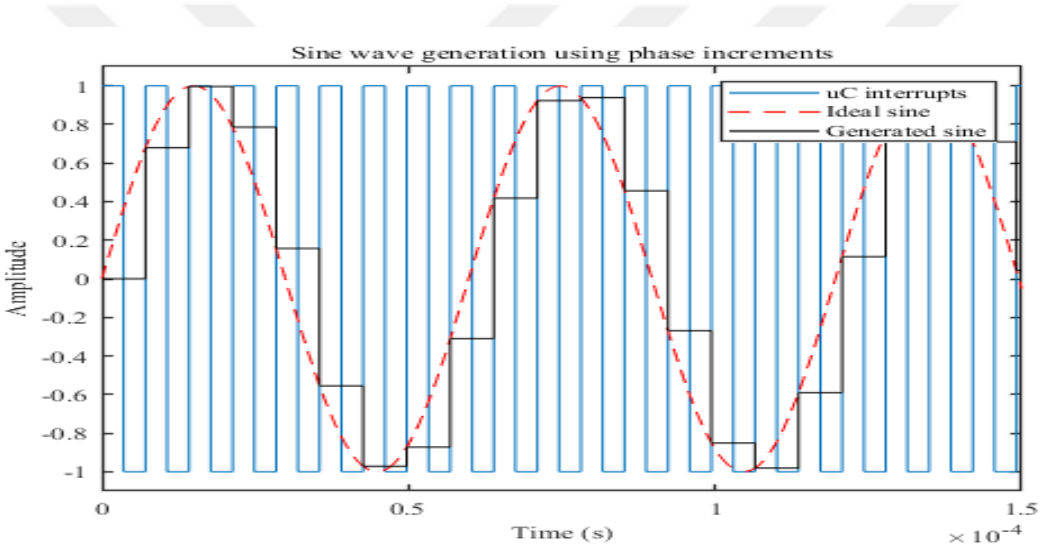

Figure 4.27: A MATLAB simulation of interrupt cycle, ideal sine wave, and sine wave generated using phase increments. A 20kHz sine wave generation is demonstrated in the simulation.

The same procedure is also verified using a microcontroller by generating a sinusoidal signal with a microcontroller and logging the generated signal using an oscilloscope. Figure 4.28 shows the generation of a 20kHz signal by the microcontroller using the method explained here. An oscilloscope is used to monitor this output signal. The noise observed on the generated signal is the noise of the oscilloscope. In the actual implementation, the clock frequency of the

microcontroller is 169MHz. The sampling rate of the ADC and the DAC refresh rate is set to 140.8 kHz, meaning that every 7µg, the microcontroller reads the ADC and writes a voltage to the DAC. The oscillation frequency of the sensor attached to the PCB is around 16700Hz, and approximately 8 samples are read for each cycle of the sensor output. The number of samples can be increased by increasing the sampling rate, but the ADC and the microcontroller speed limit the sampling rate. The phase increment is calculated as 42.739° by using Equation 4.33.

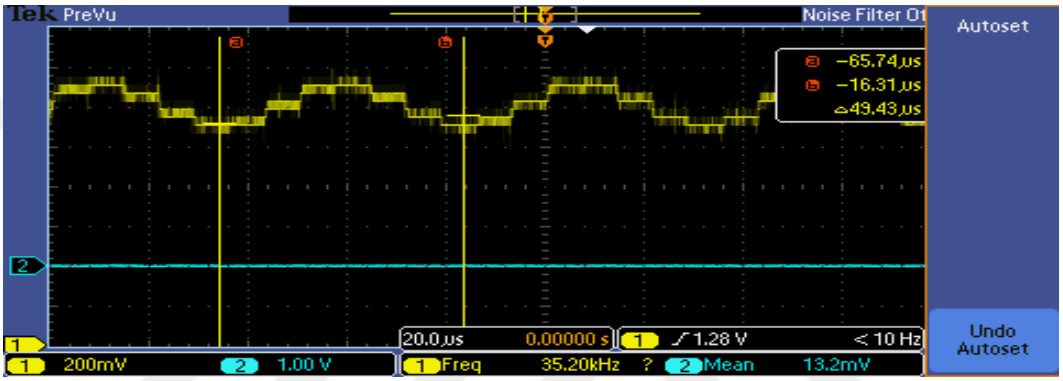

Figure 4.28: A 20kHz signal generated by the microcontroller using the phase increment method. The noise observed in the figure is from coming from the oscilloscope.

4.7.2 Frequency sweeping

The frequency sweeping functionality is significant for the digital control loop. The resonance frequency of resonators might shift over time for several reasons. Therefore, it is vital to know the actual resonance frequency of the sensor at a static position. It is observed from testing that the resonators need to be resonated close to the resonance frequency for the PI controller to track resonance frequency. This is because sensor output amplitude is minimal when oscillating at frequencies far away from the resonance frequency. Figure 4.29 shows a flowchart for the frequency sweep function. The algorithm has some initial settings defining different parameters

during the sweep, such as range, increment step, excitation voltage, and proof mass voltage.

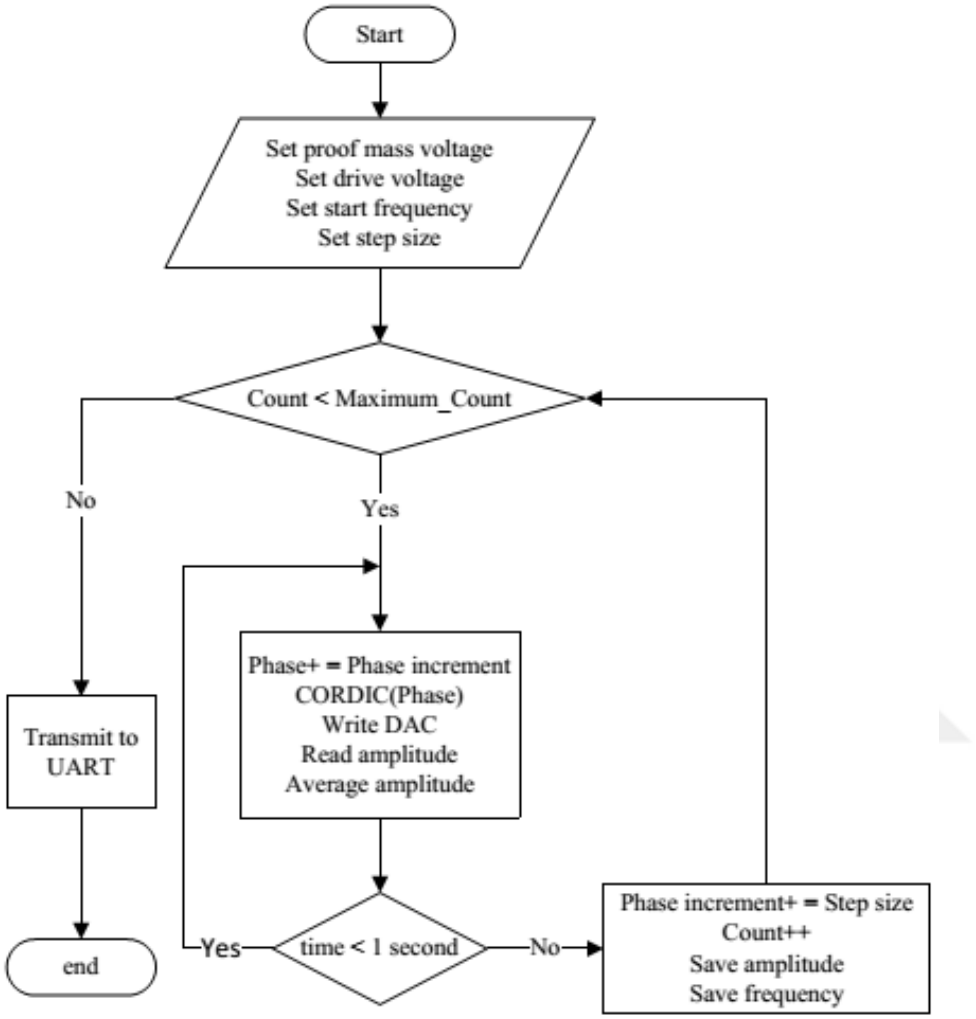

Figure 4.29: The frequency sweeping algorithm implemented in the microcontroller to obtain the resonance frequency of the resonant MEMS accelerometers.

The algorithm starts with initial settings, which include the setting of the proof-mass voltage by DAC. The excitation voltage is selected and multiplied by the sine generated by the CORDIC function. The initial frequency of the sweep is adjusted by its corresponding phase. The step size determines how much frequency is increased after one second. The maximum count is set to limit the upper frequency of the range. It is calculated by dividing the range by step size. At each frequency

value, the sensor oscillates for one second, and amplitude is recorded and averaged. After amplitude at all points is calculated, it is transmitted via serial port for plotting and analysis. The frequency sweep is an independent algorithm and does not require to be run with other algorithms. The same approach is used to test both resonators, which can be tested simultaneously or separately.

4.7.3 Amplitude stabilization

Amplitude is kept at a set point value, and a PI controller is employed to perform this functionality. The signals coming from resonators are read with an ADC, and a rectification method is used for amplitude extraction. This method is used because it is simple to implement in the digital domain. The ADC readings are converted to their absolute values, and a running average obtains amplitude information of the signal. This value is compared with a pre-determined setpoint amplitude value. The difference between amplitude and set point value goes to the PI controller as an error signal. The PI controller generates a control output that will either increment or decrement the amplitude of the excitation signal. Figure 4.30 shows a visual representation of this algorithm.

The averaging of the amplitude can be implemented with many techniques. The moving average filter is used in the current implementation. Exponential filter, least-mean-squares (LMS) filter, and Biquad filter are a few other averaging techniques. These techniques have different accuracy and speed performance. The moving average filter is not a very high-performance method compared to other techniques but is sufficient for this implementation. The parameters of the PI controller determine the speed and noise level of the extracted amplitude. A fast PI controller generates more noise than a slower PI controller. The noise and speed are also affected by the time constant of the averaging filter. A filter with a significant time constant collects a large amount of data and averages it, which results in low-noise data. The bandwidth of the averaging filter and the PI controller can be adjusted in

the software. Typically, the bandwidth of amplitude demodulation is much slower than the bandwidth of frequency demodulation.

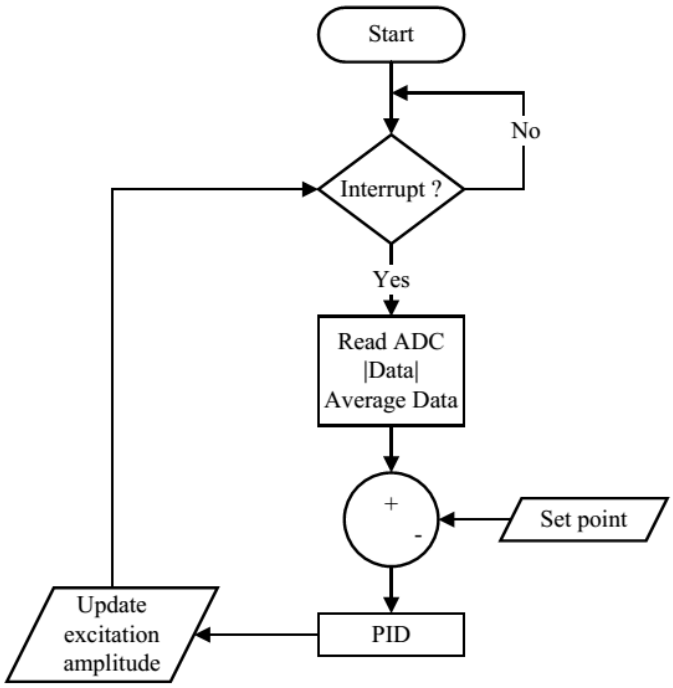

Figure 4.30: Flowchart of the algorithm for amplitude stabilization of the resonant MEMS accelerometer output implemented in the microcontroller.

4.7.4 Frequency tracking

Frequency tracking is performed by a new method similar to synchronous demodulation. The generated drive signal is multiplied by the signal read from the sensor, and the product is averaged to find its mean value, which should be zero for 90° phase shifted and equal frequencies. The 90° phase shift is ensured by adjusting the time difference between generating a drive signal and reading the sensor output with an ADC. With an adequately timed loop, the ADC will always read a 90° phase shifted version of the reference signal. Thus, the average of the multiplication values

will go to zero if the reference and the input signals have the same frequency. A PI controller is used to compare this mean to zero and generate a control output to increment or decrement the drive frequency. Figure 4.31 shows a simplified flowchart of this algorithm where the procedure is divided into four cases for efficient implementation with a microcontroller. The microcontroller reads signals from the two resonators and generates the drive signals to operate these resonators in one complete loop of four cases. The first case starts with reading the input signal from *Resonator 1* and multiplying it with the reference signal. Their product is passed through a moving average filter to get the mean value. This average value acts as the input to the PI controller that compares it with zero to generate an error signal, which the PI controller uses to generate a control word. This control word increments or decrements the phase, thus increasing or decreasing the drive signal frequency using the CORDIC function. The output of the CORDIC function is in Q1.31 (fixed point) format and is converted to a 16-bit format compatible with the DAC. The third case is used only for writing the calculated DAC value using the SPI interface. The fourth case interacts with the ADC through the SPI interface to prepare the data. The loop repeats itself for reading *Resonator 1* at one end and driving it from the other end. *Resonator 2* operates similarly, and its instructions are present in the same four cases.

The frequency tracking algorithm runs in parallel with amplitude stabilization. This algorithm sets the drive signal frequency, whereas the amplitude algorithm sets the amplitude of the drive signal. The drive signals are generated based on the amplitude and frequency demodulation data.

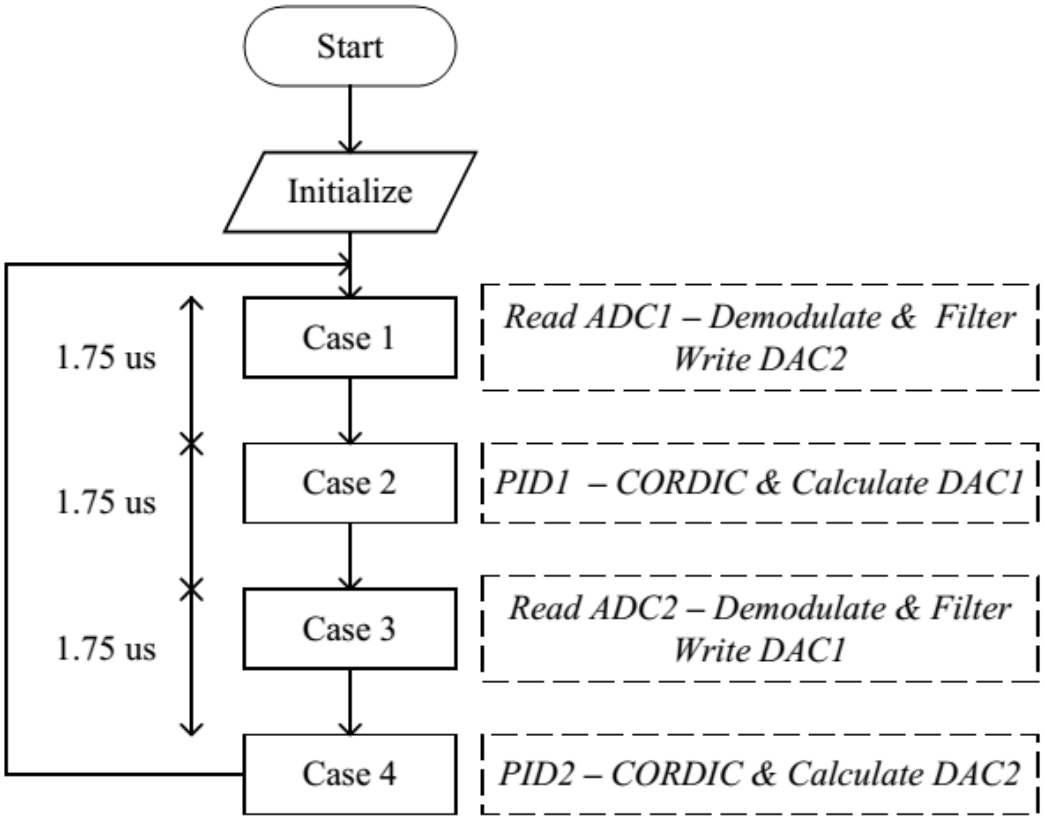

Figure 4.31: The frequency demodulation and tracking algorithm implemented in the microcontroller, showing different operations that are performed to read the resonant MEMS accelerometer output and generate a corresponding drive signal.

4.7.5 Temperature compensation

Temperature dependency is one of the major drawbacks of any MEMS sensor. Although the differential resonator design counters the effects of temperature, there is still an effect of temperature due to the non-ideal fabrication of the sensor. Therefore, temperature compensation is also critical to get better performance from a sensor. Temperature dependency is not linear for an extensive range, and it is not efficient to use second or third-order equations for temperature compensation. The computations become simple if only first-order equations are used for temperature compensation. Therefore, the temperature has been divided into regions with roughly linear temperature dependency. The corresponding compensation factor is selected

depending on the temperature reading from the on-chip temperature sensor. Figure 4.32 shows a simple algorithm to divide temperature into three linear regions and apply calibration accordingly. This algorithm is only for understanding purposes, assuming that the temperature dependency in the data has three linear regions. The actual temperature testing of individual chips will show the exact number of linear regions, and the algorithm will be adjusted accordingly. The temperature measurement refresh rate is not as fast as data sampling. Temperature changes are not very fast, and measurements can be taken much slower than data sampling.

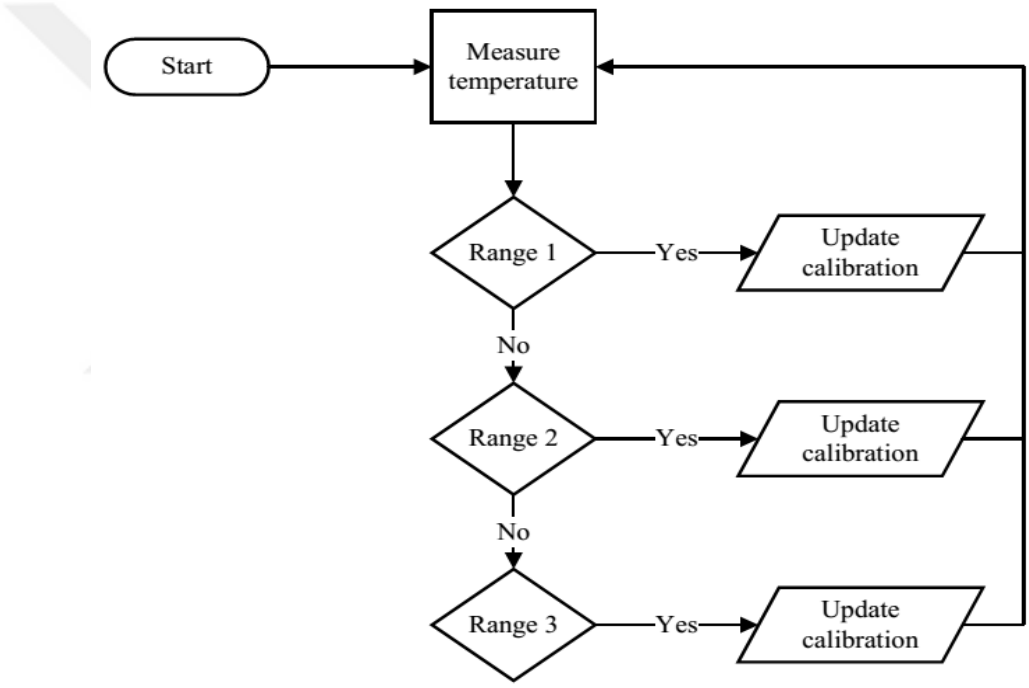

Figure 4.32: Flowchart of the algorithm used for updating the temperature calibration factor. The temperature range is divided into three regions to simplify the compensation equations.

4.7.6 Start-up procedure

A digital control loop has the benefit of starting the oscillation without needing an external start-up circuit. The resonance frequency oscillation knowledge is known before the start of the operation. In this process, the resonators oscillate simultaneously at their last know value of resonance frequency, and their amplitude is measured. The sensor oscillates near the resonance frequency if the measured amplitude is within 30~40% of the expected amplitude. In this case, the operation is transferred from an open loop to a closed loop. If the amplitude is too low, resonators are resonating away from their respective resonance frequencies. The correct resonance frequency value is required to start the operation in a closed loop. This second scenario is rare in stable sensors where resonance frequency does not shift without changes in external conditions.

4.7.7 Serial data transmission

The data is transmitted to a computer for monitoring using a serial port. Transferring the data through a serial port takes some time. The microcontroller is resonating two oscillators at approximately 17 kHz, and the time for each interrupt is approximately 1.75µs. Therefore, it is necessary to transmit serial data without disturbing the closed-loop operation. The microcontroller used in this study has different methods to transmit data using the serial port. The first method is a standard transmission which is serial and blocks a lot of other statements. This method is not suitable for our application. The second method is by using the interrupt of the serial port. This method is faster than the first and runs parallel with other interrupts. However, this method is also lengthy compared to the interrupt cycle duration. The third method uses Dynamic-Memory-Allocation (DMA) with UART, which is as fast as the interrupt-based method. However, interrupt, and DMA-based methods are not fast enough, and they may disturb the closed-loop operation. A fourth method is directly

writing to the serial port registers, which is the fastest and more suitable for high-speed applications.

4.8 Summary

This chapter provides the scheme for the digital control loop implementation of a resonant MEMS accelerometer using a microcontroller-based digital control PCB. The analog part of this implementation includes a low noise pre-amplifier stage (charge sensing pre-amplifier), an intermediate gain stage (instrumentation amplifier), and two amplifiers for generating high voltages for proof mass and cap wafer. A 16-bit ADC converts the signals to the digital domain, and all subsequent processing is performed in the microcontroller. The amplitude extraction is performed with the rectification method, and the frequency tracking is performed using a timed reference technique, which consumes less computational power compared to other methods. The drive signals are calculated in the microcontroller, and a 16-bit DAC is used to generate the excitation signals. The noise analysis shows that the pre-amplifier input referred noise (5.5fA/√Hz) is less than the Brownian noise of the sensor (19.5fA/√Hz). A Simulink model is used to simulate the operation of a resonant MEMS accelerometer using actual sensor parameters obtained from sensor characterization, showing the capability of the proposed design to track the resonance frequency of the resonators successfully. The last section of the chapter gives information about the algorithms that perform different functionalities in the microcontroller, such as frequency sweeping, amplitude stabilization, frequency tracking, and temperature compensation.

CHAPTER 5

RESULTS AND DISCUSSION

This chapter presents the results of a resonant MEMS accelerometer with a digital control loop implemented using a microcontroller. Section 5.1 shows the frequency sweep test results performed under several biasing conditions obtained using the digital control PCB. Section 5.2 presents the closed-loop operation of the sensor using a digital control loop implementation. Section 5.3 shows the testing to calculate the scale factor of the sensor and frequency tracking capability of the implemented algorithm in a microcontroller. Section 5.4 presents the effect of temperature on the sensor data and its compensation to obtain better immunity to temperature changes. Section 5.5 discusses the effect of filter parameters, proof mass voltage, excitation voltage, and data rate on the resonant MEMS accelerometer data. Finally, Section 5.7 summarizes the salient results of this chapter.

5.1 Frequency Sweep

The frequency sweep is performed at different biasing conditions (proof-mass voltage and excitation voltage) to observe the effect of these biasing conditions while operating the sensor with the digital control PCB. The proof mass voltage is set at 3V, 5V, 7V, and 10V, whereas the excitation voltage is set to 0.1mV, 0.3mV, 0.5mV, and 1mV in different tests. A similar frequency sweep test was also performed using the lock-in-amplifier setup and is repeated with the digital control readout circuit to observe any unwanted results involved with this readout circuit. Also, the discrete components used in this readout differ from those that present a lock-in-amplifier. Therefore, it is essential to perform similar tests with the digital control PCB to monitor the changes in the performance. The frequency sweep gives information

about the resonance frequency of each resonator and the gain of the resonator. The gain values may differ from lock-in-amplifier values as their gain amplifiers have different configurations. This section presents frequency sweep results at different biasing conditions for the R2B-type sensor (N4N2), which is one of the resonant MEMS accelerometer sensors characterized by the lock-in-amplifier and connected with the digital control PCB.

Figure 5.1 shows the frequency sweep of *Resonator 1* of sensor N4N2 performed at a 0.3mV excitation voltage, whereas the proof-mass voltage varies from 3V through 10V. The resonance behavior is comparable to the results taken from the lock-in-amplifier, and the sensor operates in the linear region at 0.3mV. There is a shift of approximately 3Hz in the resonance frequency when the proof-mass voltage increases from 3V to 10V, which is consistent with the lock-in-amplifier results.

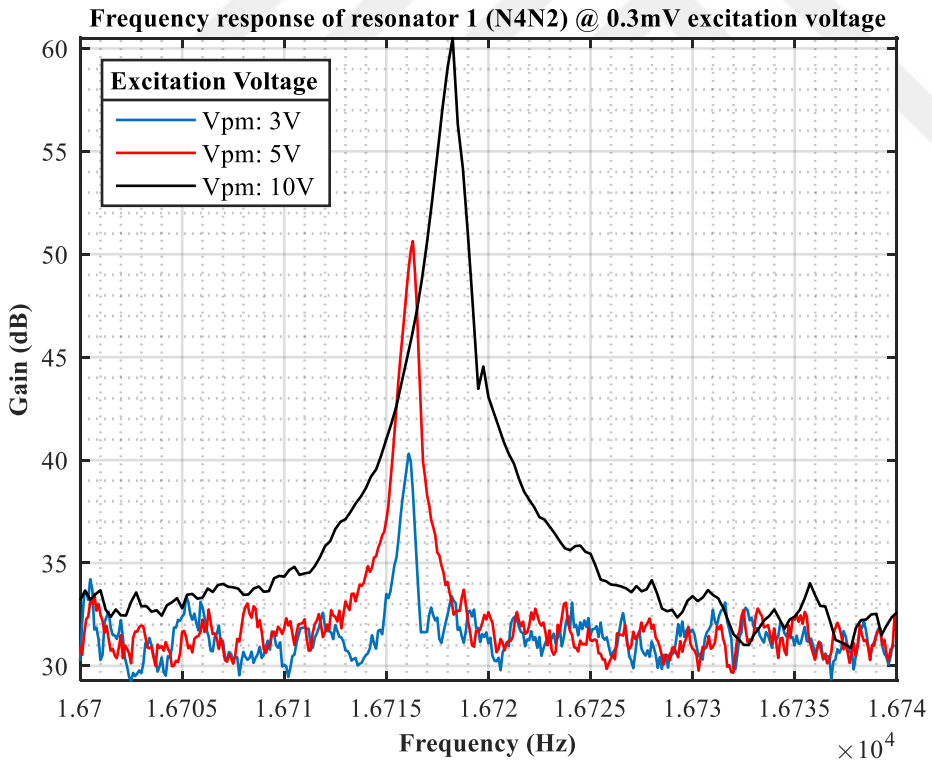

Figure 5.1: The frequency sweep response of *Resonator 1* of sensor N4N2 at 0.3mV excitation voltage at different proof mass voltage values using digital control PCB. The resonance frequency of *Resonator 1* is around 16716Hz.

Figure 5.2 shows the frequency response of *Resonator 2* of the sensor N4N2 under different values of proof-mass voltage while excitation voltage is set to 0.3mV. The plot shows an increase in the gain of the resonator as the proof-mass voltage increases from 5V to 10V. The frequency shift is approximately 3Hz with this change in the proof-mass voltage. The resonance frequency is approximately 16485Hz, which is lower than the resonance frequency of *Resonator 1*. This result is also consistent with the findings obtained using a lock-in-amplifier setup.

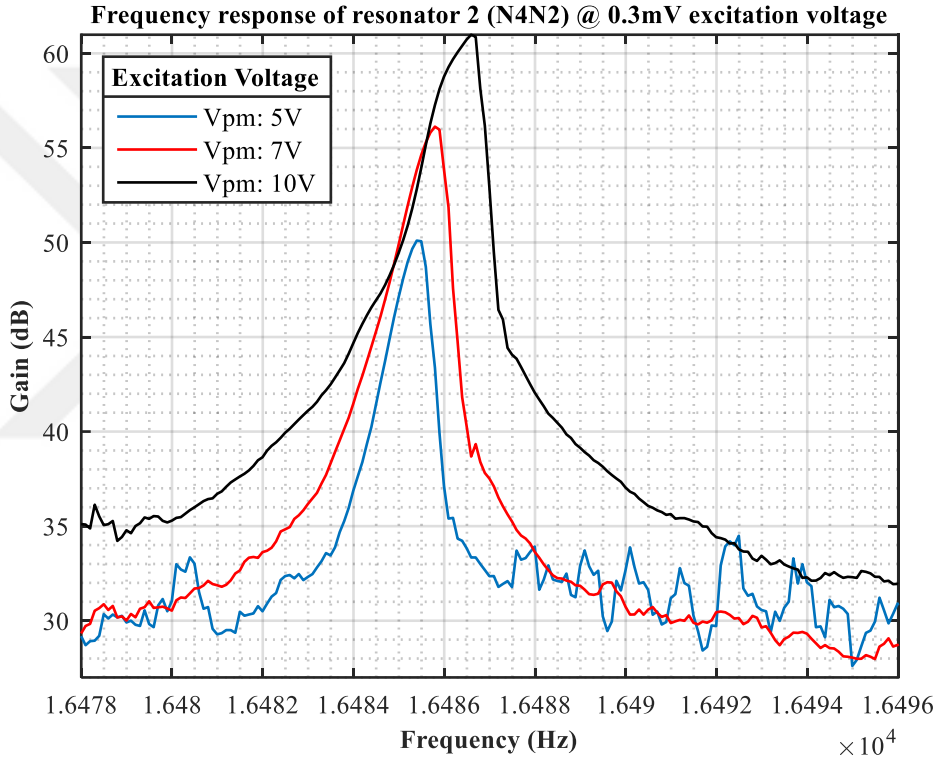

Figure 5.2: The frequency sweep response of *Resonator 2* of sensor N4N2 at 0.3mV excitation voltage at different proof mass voltage values using digital control PCB. The resonance frequency of *Resonator 2* is around 16485Hz.

Figure 5.3 shows a frequency response of *Resonator 1* of the sensor N4N2 at 5V proof-mass voltage when the excitation voltage is changed from 0.3mV to 0.5mV. The plot shows that this small change in the excitation voltage has no significant

effect on the gain of *Resonator 1*. The change in the resonance frequency is approximately 1Hz as the excitation voltage is increased from 0.3mV to 0.5mV.

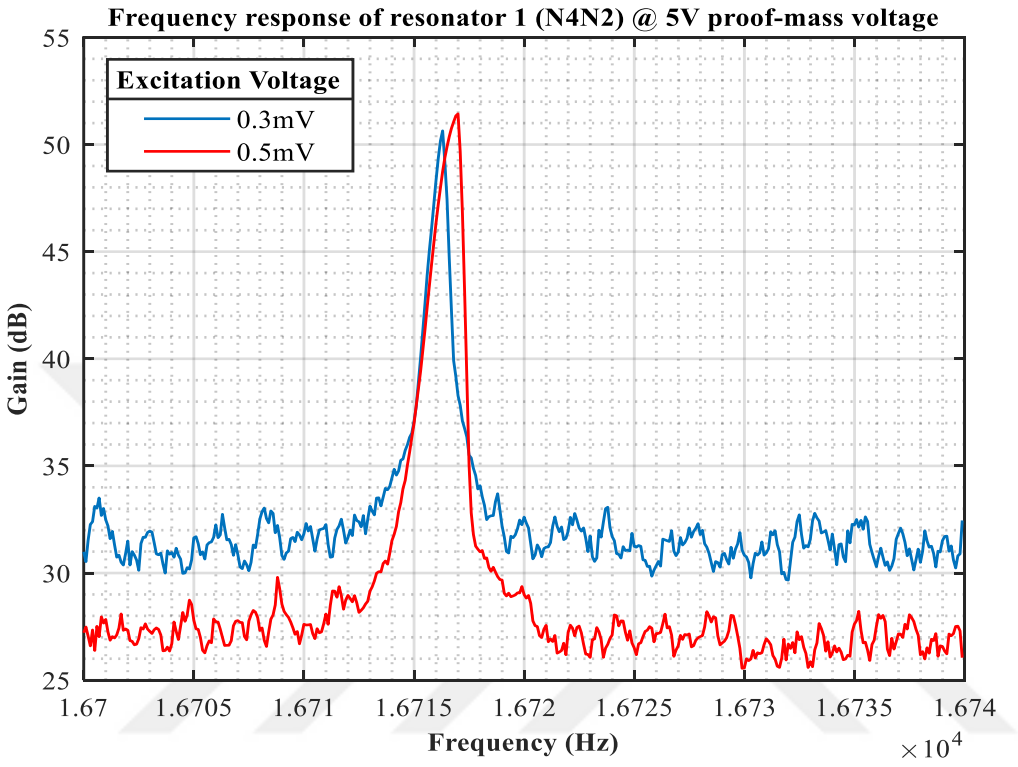

Figure 5.3: The frequency sweep response of *Resonator 1* of sensor N4N2 at 5V proof mass using digital control PCB. The resonance frequency is around 16716Hz.

Figure 5.4 shows the frequency sweep response of *Resonator 2* of the sensor N4N2 at 7V proof mass, with excitation voltage values of 0.1mV and 0.3mV. There is very little change in the gain as a result of the change in the excitation voltage from 0.1mV to 0.3mV. The change in the resonance frequency (16485Hz) is approximately 1Hz as the excitation voltage changes. The results are consistent with the lock-in-amplifier results.

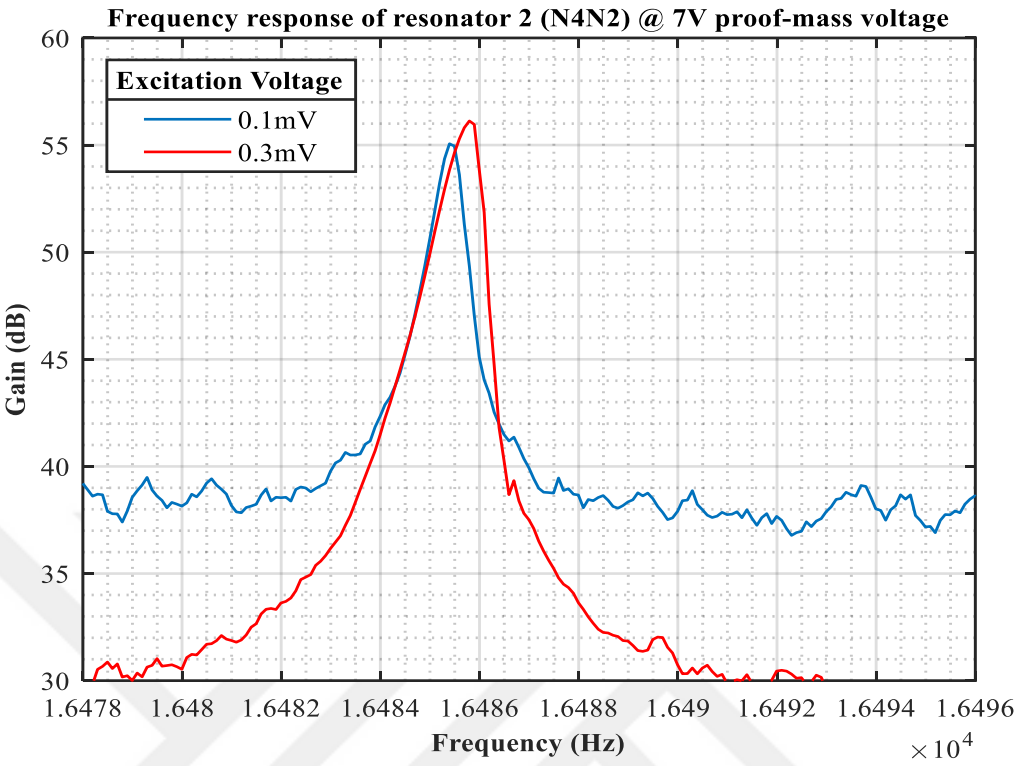

Figure 5.4: The frequency sweep response of *Resonator 2* of sensor N4N2 at 7V proof mass using digital control PCB. The resonance frequency is around 16485Hz.

These results emphasize that frequency sweeping at different biasing conditions is critical for effective sensor operation, and the limits of linear boundaries should be recorded for each resonator from these tests. These limits are beneficial for closed-loop operations. The amplitude stabilization is achieved using a PID controller that drives the output amplitude to a set-point value by changing the excitation voltage level. Therefore, a limit is required to the excitation voltage level to avoid going into the non-linear region.

These plots also provide information about the shift in the resonance frequency when the excitation voltage is changed. The shift in the resonance frequency is slight when the proof-mass voltage is small, and this shift increases with an increase in the proof-mass voltage. Therefore, the proof mass and excitation voltage must be selected to keep the sensor from non-linear regions.

Figure 5.5 summarizes the frequency response of *Resonator 1* of the sensor N4N2 performed under different biasing conditions. The proof-mass voltage is changed between 3~10V, and the excitation is varied between 0.1mV and 1mV. The plot shows that the resonance frequency is not affected much by the proof-mass voltage or the excitation voltage in the given ranges. There is a change of 2-3Hz in the resonance frequency at higher values of excitation voltage, indicating a shift towards non-linearity.

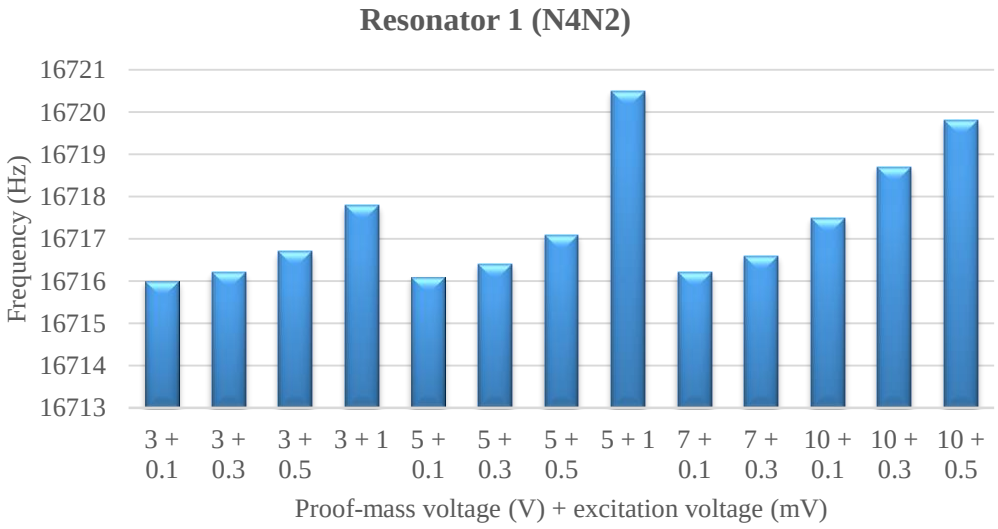

Figure 5.5: The summary of the resonance frequency of *Resonator 1* of sensor N4N2 obtained by frequency sweeping at different biasing values using the digital control PCB. The resonance frequency of *Resonator 1* is 16716Hz.

The results of frequency sweep are shown for both the resonators at different values of the proof mass and excitation voltage. The response is consistent for all biasing conditions, but slight differences exist in the data. Therefore, keeping track of these values is critical to efficiently operate the sensor in a closed-loop configuration without going into a non-linear region.

Figure 5.6 shows a summary of the resonance frequency of *Resonator 2* of sensor N4N2 at several biasing conditions. The overall behavior is consistent with results obtained using the lock-in-amplifier. The change in resonance frequency is minimal

when the proof mass or excitation voltage is changed. The resonance frequency does not change much for this small excitation voltage range.

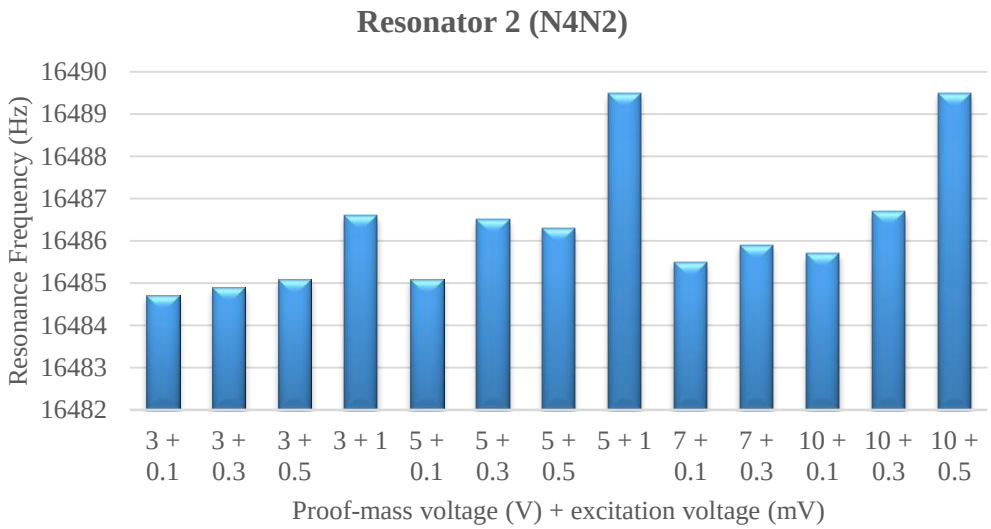

Figure 5.6: The summary of the resonance frequency of *Resonator 2* of the sensor N4N2 obtained by frequency sweeping at different biasing values using the digital control PCB. The resonance frequency of *Resonator 2* is around 16485Hz.

The gain of the resonators increases significantly with proof mass voltage.

Figure 5.7 summarizes the gain of resonators of the sensor N4N2 under different values of the proof mass and excitation voltage. The proof-mass voltage affects the resonator gain, but the excitation voltage does not significantly affect the gain. *Resinator 1* and *Resonator 2* show similar gain values under different biasing conditions.

5.2 Closed loop operation

The frequency sweep of the resonator gives optimum values of proof mass voltage and excitation voltage to drive the resonators in the linear region. Increasing the proof-mass voltage near 10V increases nonlinearity in the data, and decreasing the

proof-mass voltage to 3V decreases the gain and, consequently, the SNR of the data. 5V is an optimum value that provides sufficient gain, and the linearity threshold is better than 10V proof-mass voltage. The excitation voltage value between 0.3mV and 0.5mV shows a linear behavior at a 5V proof-mass voltage.

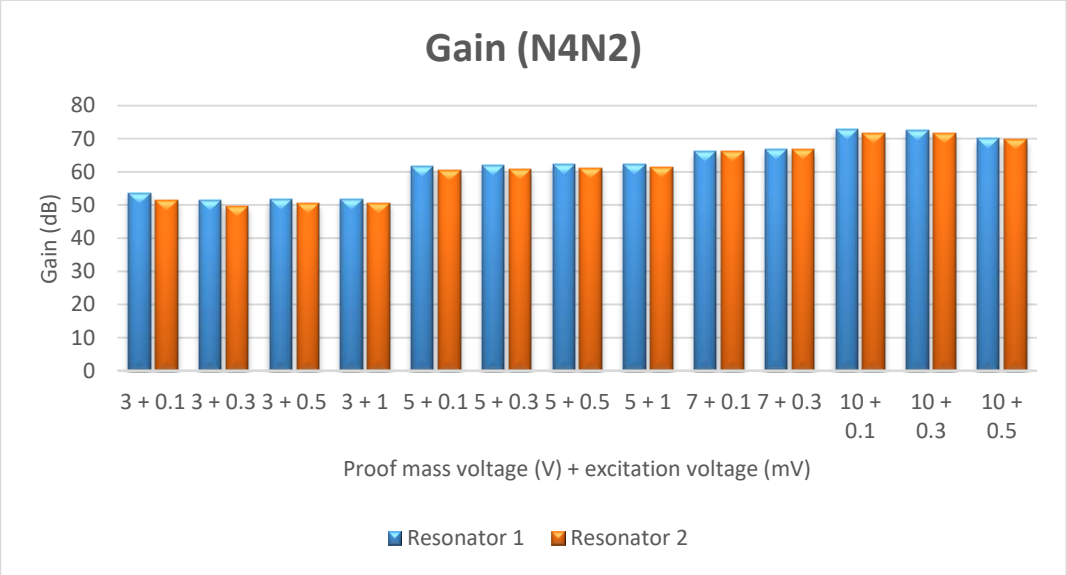

Figure 5.7: The summary of the gain obtained by frequency sweeping at different biasing values using the digital control PCB. The gain of the resonators increases significantly (from 50dB to 73dB) with an increase in the proof-mass voltage.

Figure 5.8 shows the Allan variance plot of data obtained from the sensor. The data is obtained as the difference of frequencies between two resonators and then converted to acceleration by dividing with the scale factor. It can be seen from this plot that bias instability of 9.7µg/√Hz can be obtained under these conditions. The achieved bias instability value is very close to that obtained using the lock-in-amplifier setup (7µg). The white noise value is higher compared to the data obtained using the lock-in-amplifier. This higher value is expected owing to a lower data rate and sampling rate in this implementation.

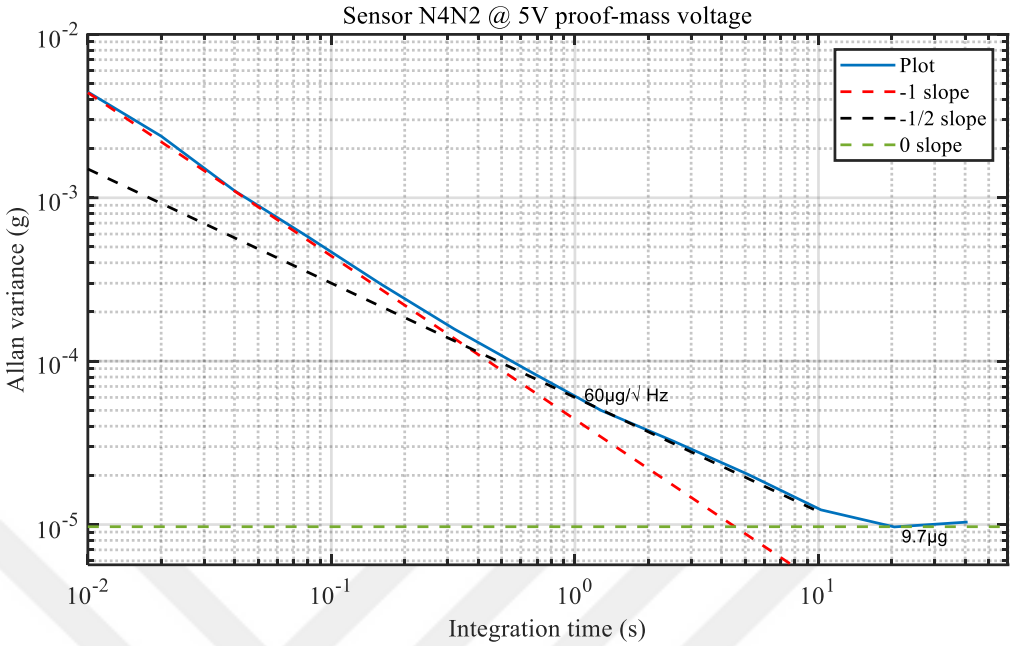

Figure 5.8: Allan variance plot of data obtained from sensor N4N2 at 5V proof mass voltage, showing a bias instability of 9.7µg, which is very close to the value measured with the lock-in amplifier (7µg).

The slope of different regions of the Allan variance plot shows the type of noise in the sensor data. The figure shows the Allan variance plot of the N4N2 data at 5V proof-mass voltage with two lines having a slope of -1 and -1/2. The quantization noise has a slope of -1 in the Allan Variance plot, whereas the white noise or VRW has a slope of -1/2. The plot shows that quantization noise initially dominates the noise in the data at high frequencies. The VRW dominates the noise around the value of one second.

Comparing this plot with the plot obtained using the lock-in-amplifier shows a difference in the noise in their data. The lock-in-amplifier data shows a slope of -1 until very close to the bias instability flat region. This plot shows the VRW noise well before it reaches the flat region. Therefore, the data collected with the digital control PCB has higher white noise than the lock-in-amplifier. The sampling rate in the lock-in-amplifier is 200Msamples/s compared to 147Ksamples/s of the

microcontroller used in the digital readout circuit. The data rate of the lock-in-amplifier is 225Hz compared to the 20Hz data rate of the digital control PCB. The speed of the microcontroller, used in the digital control readout circuit, limits the sampling and the data rate. Owing to these limitations, the data collected with the digital control PCB shows a higher value of white noise.

5.3 Scale factor

The scale factor is also calculated at different biasing values. In testing with the lock-in-amplifier, it was observed that the scale factor does not change with changes in proof mass voltage and excitation voltage. Similar behavior can also be observed in testing performed with digital control PCB. Figure 5.9 shows the test setup used to calculate the scale factor of this sensor. The sensor is rotated from the +1g position to the -1g position.

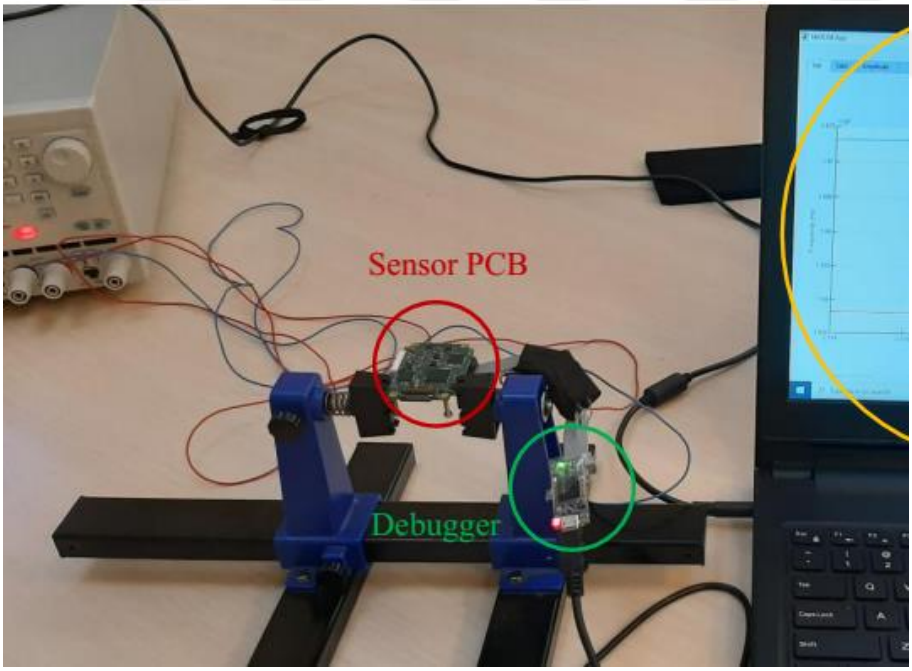

Figure 5.9: Test setup to calculate scale factor using digital PCB and real-time data logging on a computer. A mechanical structure is used to rotate the sensor with some level of accuracy.

The scale factor calculations require the readout circuit to efficiently track the frequency when the position of the sensor changes between different g positions. Therefore, this test also verifies the frequency-tracking capability of the algorithm used in this implementation.

Figure 5.10 shows the scale factor calculated at 7V proof mass voltage with 0.3mV excitation voltage. The scale factor of the sensor is 95.35Hz/g. The sensitivity of *Resonator 1* is approximately 45Hz/g, and the sensitivity of *Resonator 2* is approximately 50Hz/g. This difference in the sensitivity of the resonators is consistent with the results of the lock-in-amplifier.

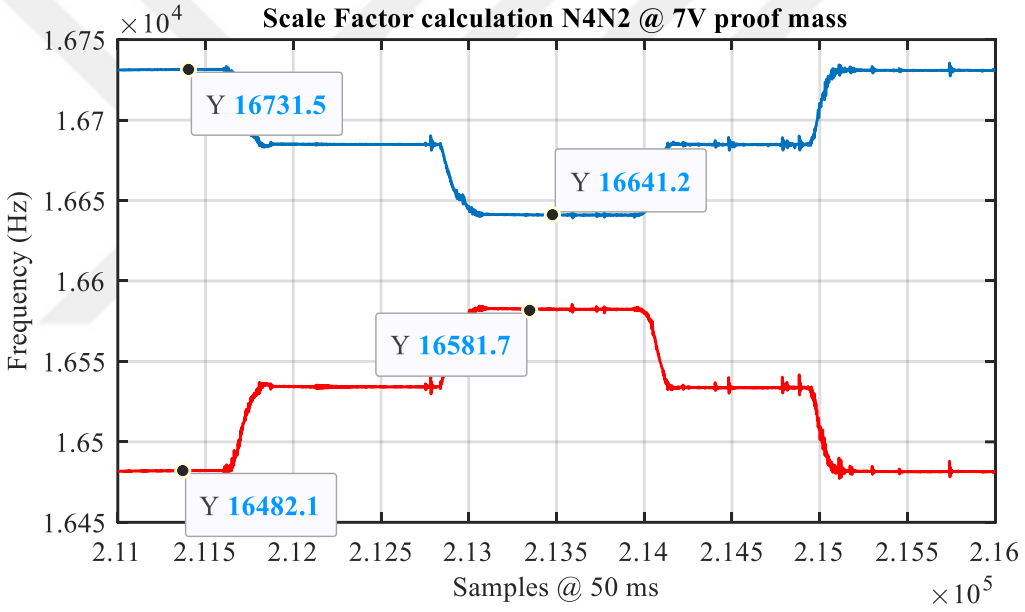

Figure 5.10: Scale factor calculation at 7V proof mass voltage. The scale factor value is calculated as 95.35Hz/g.

Another plot is presented in Figure 5.11, where the scale factor is calculated at 5V proof mass voltage and 0.5V excitation voltage. The scale factor of the sensor at these biasing conditions is 95.2Hz/g.

The tests with the lock-in-amplifier showed that the scale factor is stable for various biasing conditions with a value around 95Hz/g. The results from the digital control PCB also show that the scale factor of the sensor N4N2 is constant and does not significantly change with proof mass or excitation voltage. The sensitivity of *Resonator 1* is approximately 45Hz/g, and the sensitivity of *Resonator 2* is approximately 50Hz/g.

The scale factor calculation is another feature of the digital control PCB. The digital control implementation operates the sensor in a closed loop and performs other essential functionalities. This flexibility to perform several operations is impossible in analog-based sensors.

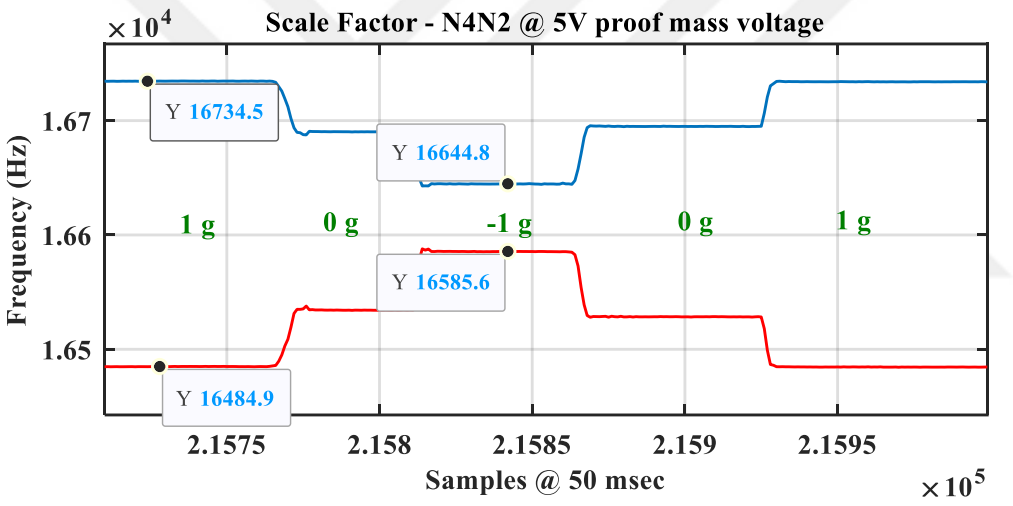

Figure 5.11: Scale factor calculation at 5V proof mass voltage. The scale factor is approximately 95.2Hz/g.

5.4 Temperature compensation

Temperature compensation is also necessary to counter the effects of temperature on the sensor output. Ideally, differential reading should cancel out temperature dependency. However, the mismatch of 5Hz/g in the scale factor of two resonators of the sensor N4N2 results in temperature dependency even after differential reading.

Figure 5.12 shows the resonance frequency data of both resonators collected in a temperature chamber. The data is collected while the temperature changes from 0°C to 70°C. The data is collected in this range only because a commercial debugger circuit is used to obtain the data from the microcontroller. This debugger has a limited range of operation and malfunctions at temperature values outside the given range. Therefore, the temperature test is performed between 0°C and 70°C. The plot shows that both resonators' resonance frequency is inversely proportional to the temperature in this range. The frequency of both the resonators changes similarly, so an initial temperature compensation is achieved by differential reading. The data plotted in the figure is filtered to observe the different rates of frequency change. Ideally, the change in the frequency is equal. However, the resonance frequency of *Resonator 1* changes by approximately 6.5Hz in this temperature range, and *Resonator 2*'s resonance frequency changes by approximately 6Hz in the same temperature range. The mismatch between the scale factor of the two resonators results in this difference.

The differential frequency data of this plot shows a shift of 5mg in acceleration at a stationary position, as shown in Figure 5.13. Under no applied acceleration, the sensor shows an acceleration of approximately 5mg due to changes in the temperature. The effect of temperature is minimal (less than 0.1mg/°C) and can be further improved by applying temperature compensation to the data. The temperature compensation can be applied to the individual frequency or differential data. The compensation performed in this study uses the differential data to map the temperature changes to the differential frequency changes. The temperature and the differential frequency relationship is simple in the given temperature range.

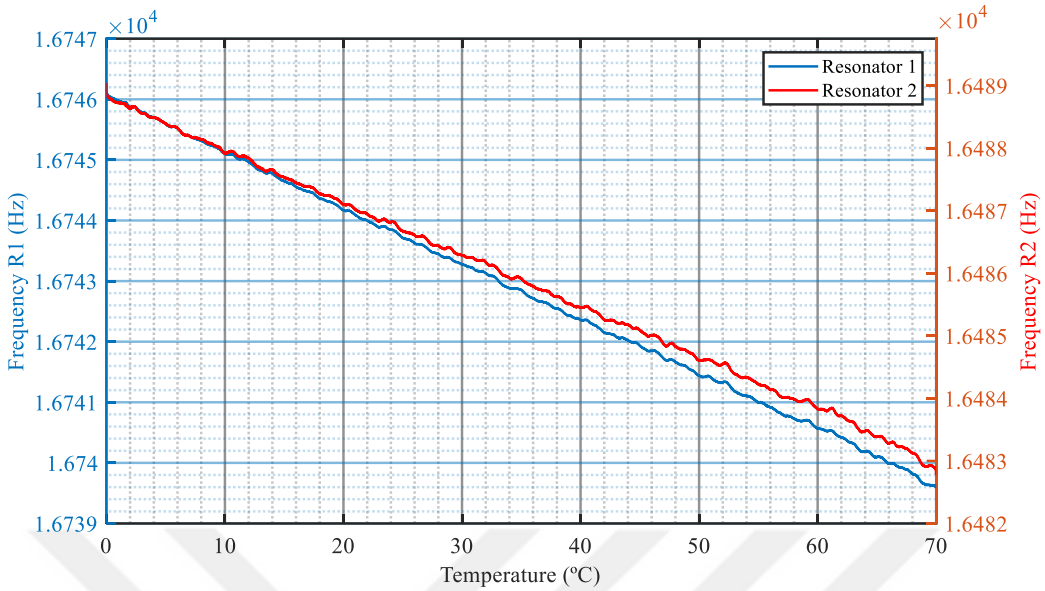

Figure 5.12: Temperature dependency of the resonance frequency of two resonators of sensor N4N2. The shift in the resonance frequency of *Resonator 1* is 0.093Hz/°C, and the shift in the resonance frequency of *Resonator 2* is 0.086Hz/°C.

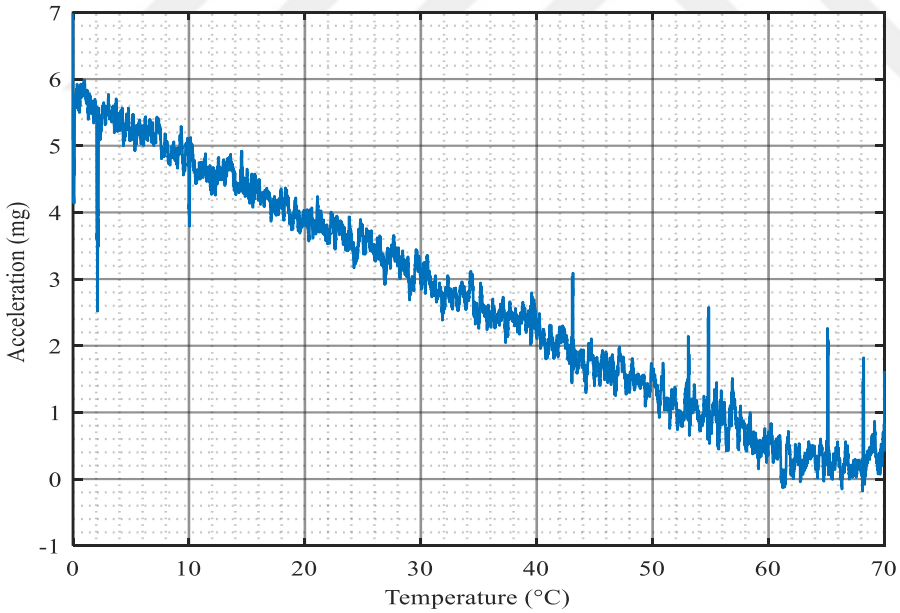

Figure 5.13: The acceleration data at zero input acceleration using the differential frequency reading in a temperature test (0°C to 70°C), showing less than 0.1mg/°C shift in the measure acceleration.

Figure 5.14 compares the Allan variance plot with temperature-dependent and temperature-compensated data. The figure shows that after compensation, the slope on the right side of the plot reduces, indicating lower temperature dependency. The second improvement is the decrease in bias instability. The plot shows that after temperature compensation, there is a three times improvement in the bias instability of the data.

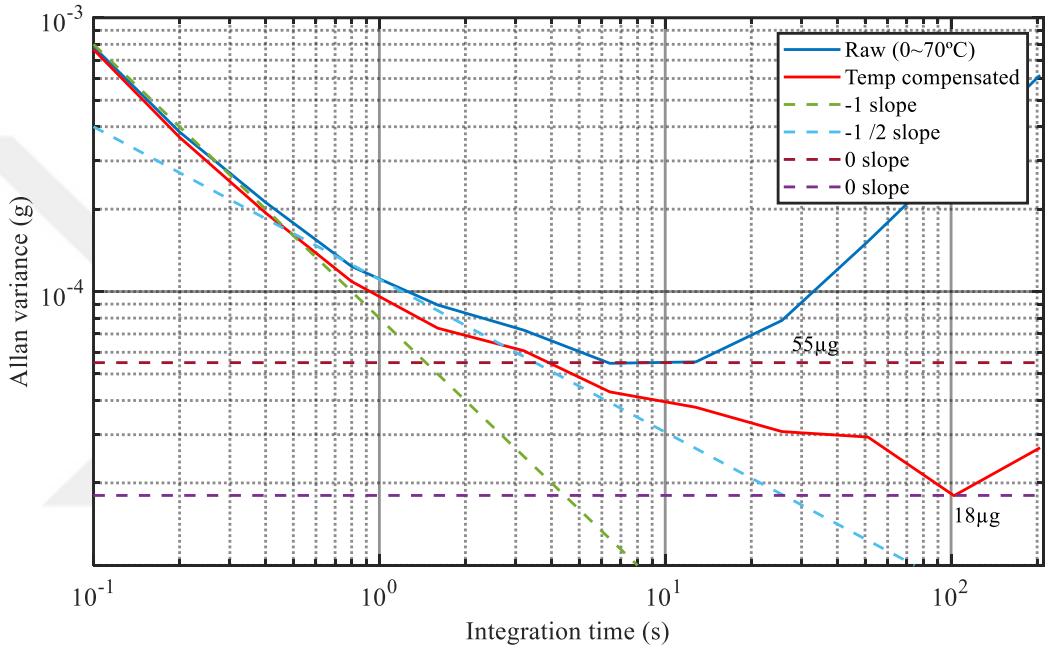

Figure 5.14: Comparison of Allan variance plot for temperature-dependent and compensated data collected in the 0°C~70°C range. After temperature compensation, the bias improves significantly (from 54µg to 18µg).

5.5 Relevance with the literature

Table 5.1 compares the developed digital control loop-based resonant MEMS accelerometer with the literature data, showing only a few selected analog readout-based works. Other published works are available, but their performance is comparable to those shown in the table. Some resonant MEMS accelerometers with analog readout circuits show sub-µg bias instability while obtaining the data using an external frequency readout method. However, most of the values are reported after

the post-processing of data, which removes the effects of temperature and other drift-causing factors. The bias-instability of the sensor used in this study is obtained as low as 7µg using the lock-in-amplifier setup and 9.7µg using the digital control PCB; however, these values are limited by the sensor performance. Theoretically, the digital control implementation used in this study can achieve a sub-µg bias instability value with an improved resonant MEMS accelerometer.

Table 5.1: Comparison of different features of the proposed system with some of the sensors available in the literature. The result of the digital control loop in this work is very close to the result obtained from professional lab equipment.

	Readout type	Bias Instability	Remarks	Temp. comp.	Debug and testing	Compact
[63]	Analog, CMOS	0.4µg*	Digital freq. reading	Post	X	-
[7]	Analog	56ng	High temp. dependency	Post	X	-
[16]	Analog, CMOS	0.6µg*	Digital freq. reading	Post	X	-
[42]	Digital, FPGA	-	Only a MEMS resonator	Possible	Possible	X
[43]	Digital, FPGA	18~40µg	No stable amplitude	Post	Possible	X
This work	Digital, Lock-in-amplifier	7µg***	Lab equip.	X	X	X
	Digital, micro-controller	9.7µg**	Speed limitations	√	√	√

*Post-processed data. The effect of temperature and other drift effects were removed. The difference in the resonators is also mitigated by post-processing.
**The bias instability is limited by the sensor performance as well as the microcontroller data rate.
***The bias instability does not go below 7µg even with a lock-in-amplifier setup.

5.6 Discussion

The results of frequency sweeping, scale factor calculation, closed loop operation, and temperature compensation are shown in the previous sections. The proof mas voltage and the excitation are changed to obtain data from the sensor at different biasing conditions. The sensor's bandwidth is also changed, affecting the sensor's performance. This section provides an in-depth interpretation of these results.

5.6.1 Effect of filter parameters

The closed loop implementation in the digital domain uses a PLL implementation in the microcontroller. There is a digital filter in the PLL that takes a mean value of the product of the input signal and the reference signal. The length of the filter controls its time constant. The second component of the PLL implementation is a PI controller whose parameters dictate the sensor's bandwidth. However, there is a trade-off between the sensor's bandwidth and the noise performance. Aggressive PI parameters make the tracking fast but cause an increase in the demodulated frequency fluctuation. If the PI parameters are assigned small values, the noise performance improves. Table 5.2 summarizes noise data collected at 20Hz and 35Hz sensor bandwidth.

Table 5.2: The noise level of the sensor-N4N2 (R2B-type) at 100Hz and 175Hz bandwidth. The noise performance degrades significantly with an increase in the sensor bandwidth.

Proof mass voltage	Excitation voltage	Noise, μg/√Hz	
Bandwidth		100 Hz	175 Hz
5V	0.1mV	99	619
	0.3mV	41	208
	0.5mV	28	154
3V	0.1mV	109	1900
	0.3mV	34	578
	0.5mV	28	356

Figure 5.15 shows the Allan Variance plot of data collected from the sensor-N4N2 at 3V proof mass and 0.3mV excitation voltage. There are two plots in this figure. One of the plots shows the data collection at 20Hz bandwidth, and the second plot shows data collection at 175Hz.

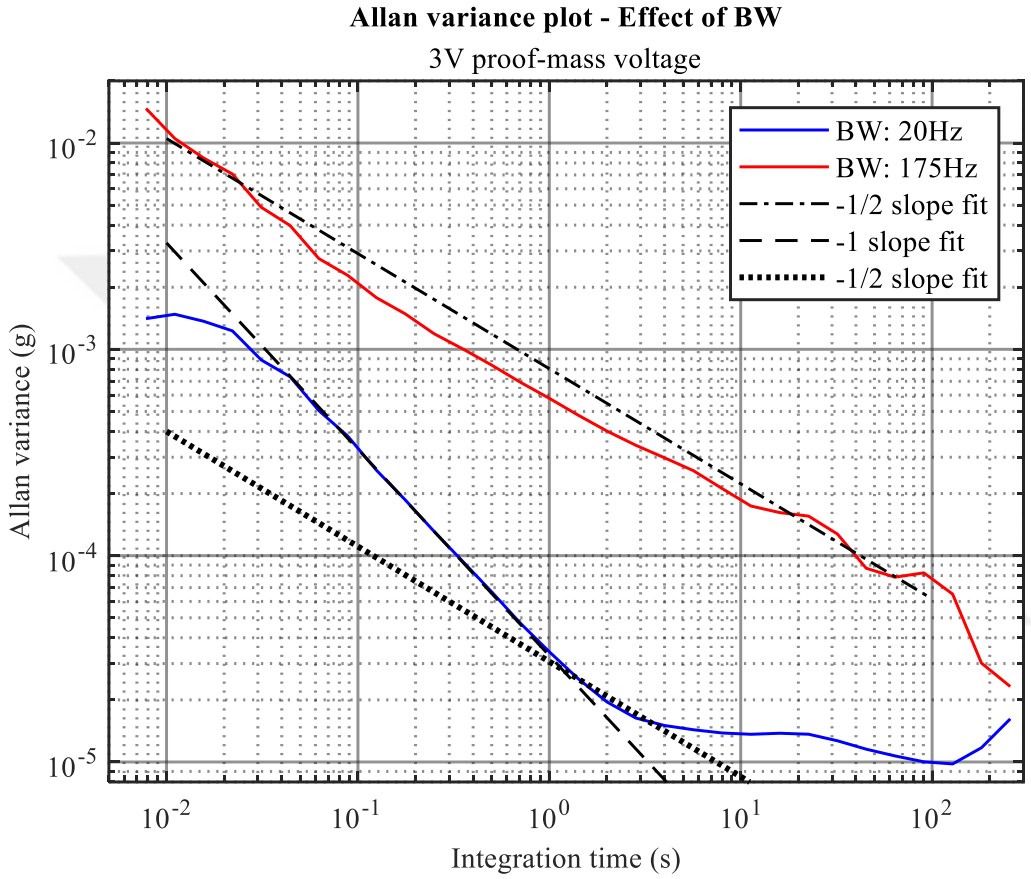

Figure 5.15: The Allan Variance plot showing the effect of bandwidth on the noise performance. The noise degrades from 34µg/√Hz to 600µg/√Hz as the bandwidth increases from 20Hz to 175Hz.

This plot aims to understand the effect of sensor bandwidth on the noise present in the data. Two lines are fitting the data with slopes -1 and -1/2. The slope of the data collected at 20Hz is -1, which corresponds to the quantization noise. The slope of the data collected at 175Hz is -1/2, which corresponds to VRW or white noise. The bias instability level values are close to each other. However, the lower bandwidth

data reaches the bias instability much faster than the 175Hz bandwidth data. Increasing the bandwidth of the sensor affects the noise performance. The white noise increases considerably by increasing the bandwidth of the sensor. The -1/2 slope can also be visualized in the 20Hz bandwidth data, but its span is minimal, and other regions overshadow it.

5.6.2 Effect of proof mass voltage

The gain of the resonators is directly proportional to the proof mass voltage. Figure 5.16 shows the gain of resonators of sensor N4N2 at a fixed value of excitation voltage. The dependence of gain on the proof mass voltage is clear from the plot, as both resonators show an increase in the gain with increasing proof-mass voltage.

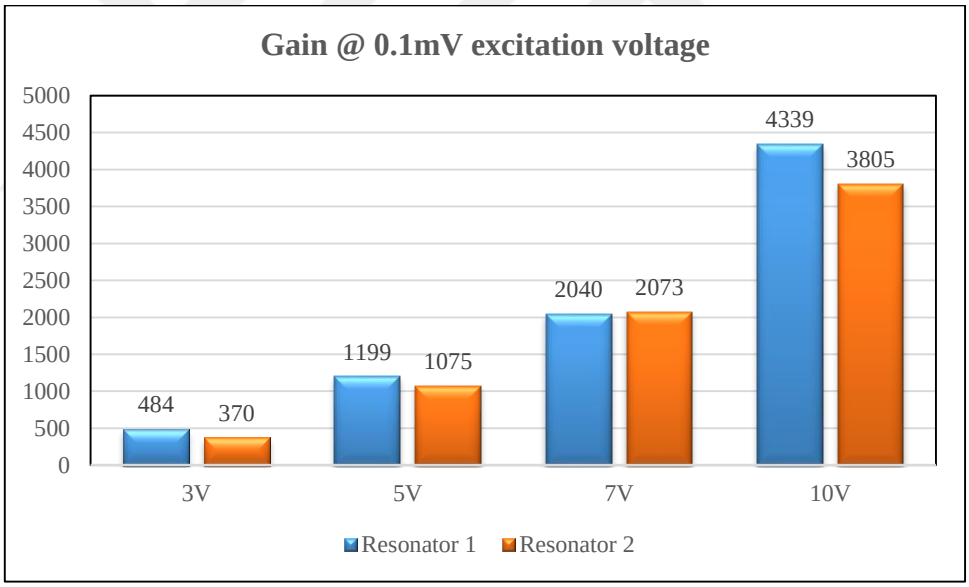

Figure 5.16: The effect of proof mass voltage on the gain of the resonators at 0.1mV excitation voltage using data collected by the digital control PCB. The gain increases 10 times as the proof-mass voltage goes from 3V to 10V.

The proof mass voltage also affects the resonance frequency of the resonators, but the effect is minimal. Figure 5.17 shows the effect of proof-mass voltage on the

resonance frequency of the resonators at a constant excitation voltage value. *Resonator 1*'s resonance frequency remains constant for 3V, 5V, and 7V proof mass voltage, increasing only by 3Hz at 10V proof mass voltage. *Resonator 2* shows a similar behavior where resonance frequency changes only 4Hz as the proof mass voltage increase from 3V to 10V. The proof mass voltage also affects the noise level of the sensor. Increasing the proof mass voltage increases the sensor's gain, increasing the SNR. Therefore, the noise performance improves due to high proof-mass voltage. The selection of proof mass for the closed-loop operation is made considering these parameters. A lower value is undesired as the gain will be low, and the input signal will be too noisy. A very high proof mass voltage is also not recommended as it limits the linear operating range of the resonators. There is a trade-off between high noise performance and the linearity of the closed-loop operation.

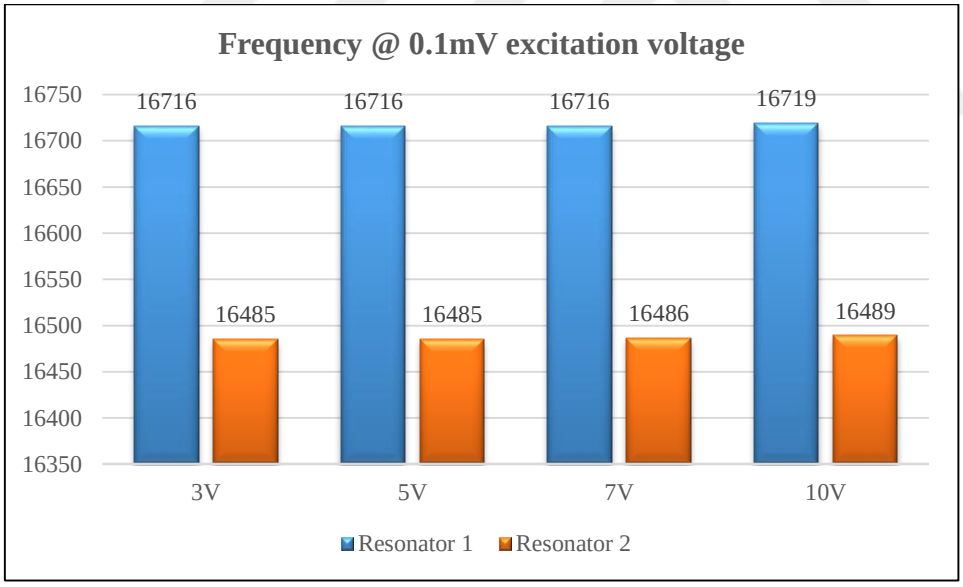

Figure 5.17: Effect of proof mass voltage on the resonance frequency of the resonators at 0.1mV excitation voltage. There is no significant change (<4Hz) in the resonance frequency as the proof-mass voltage changes from 3V to 10V.

5.6.3 Effect of excitation voltage

The excitation voltage is another parameter that is changed to observe its effect on the sensor's performance. Figure 5.18 summarizes the effect of the excitation voltage on the sensor's gain while the proof mass voltage is 5V. The increase in the gain of resonators 1 and 2 is 7% and 9%, respectively, when the excitation voltage increases from 0.1mV to 1mV. This change is negligible compared to the effect of proof mass voltage on the sensor gain.

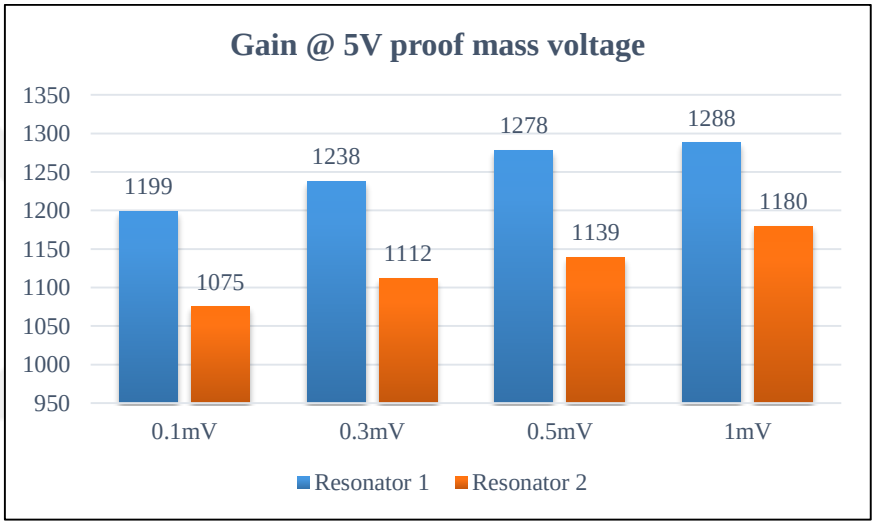

Figure 5.18: Effect of excitation voltage on the gain of the resonators at 5V proof mass. The change in the gain due to excitation voltage (9%) is insignificant compared to the change in the gain due to proof-mass voltage (10 times increase).

Figure 5.19 shows the excitation voltage's effect on the resonators' resonance frequency. In the mentioned excitation voltage range, the resonators' resonance frequency changes by approximately <4Hz, showing that the resonance frequency for this sensor design does not change significantly by a change in the excitation voltage while operating with the digital control PCB.

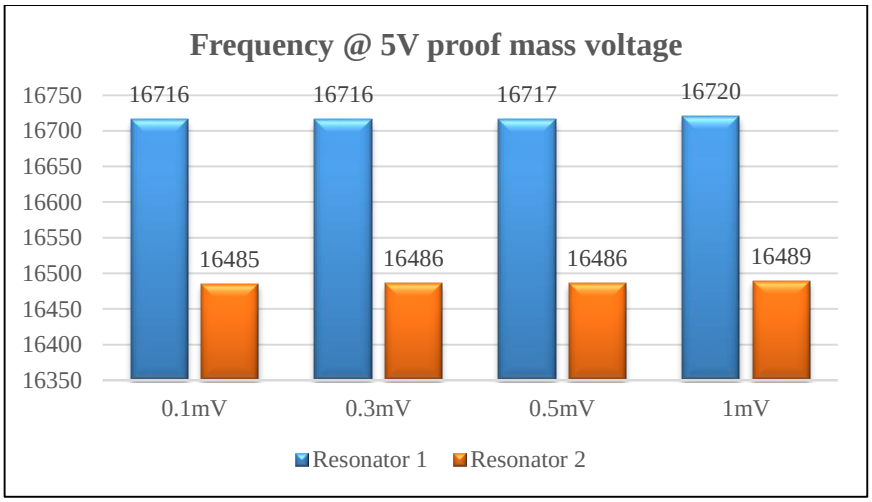

Figure 5.19: Effect of excitation voltage on the resonance frequency of the resonators at 5V proof mass. The resonance frequency changes <4Hz while the excitation voltage increases from 0.1mV to 1mV.

5.6.4 Effect of data rate

The data collection rate also affects the sensor noise. Figure 5.20 shows Allan Variance plots of data collected at 3V proof mass voltage and 0.3mV excitation voltage. The data rate in one of the plots is 224Hz, whereas the data rate in the second plot is 23Hz. The slope of -1/2 is present in the data collected at 224Hz, which corresponds to white noise. Decreasing the data collection rate to 23Hz degrades the noise performance. The co-efficient of VRW at T=1 degrades from 300µg/√Hz to 1.6mg/√Hz. However, the slope of the data is still -1/2, showing that the existing white noise in the data is increasing by a reduction in the data collection rate. This observation is critical in determining the rate at which the digital controller transmits the data for analysis.

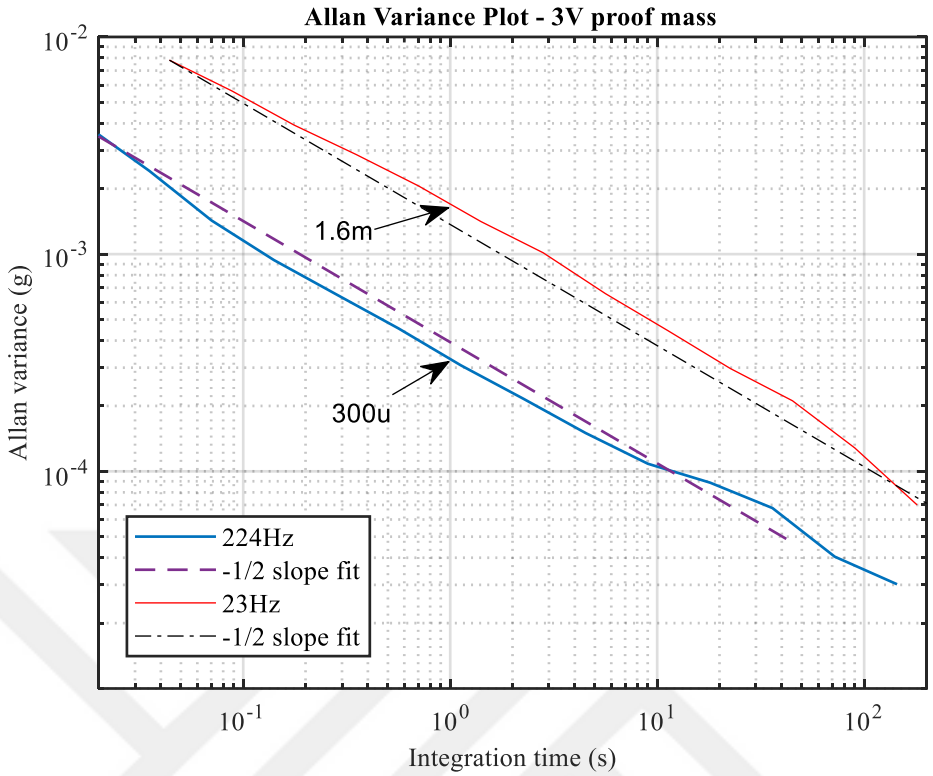

Figure 5.20: The effect of data rate on the data with dominant white noise. The noise level degrades from 300µg/√Hz to approximately 1600µg/√Hz as the data rate is reduced 10 times (224Hz to 23Hz).

The data rate also affects the sensor noise when the quantization noise is initially dominant. Figure 5.21 shows the Allan Variance plot of the data with 3V proof-mass voltage and 0.3mV excitation voltage. The sensor's bandwidth is low, suppressing the white noise and quantization noise appears with a -1 slope. When the data rate is reduced from 225Hz to 23Hz, the slope of the data becomes -1/2. This behavior shows that the white noise has become more prominent at a low data rate.

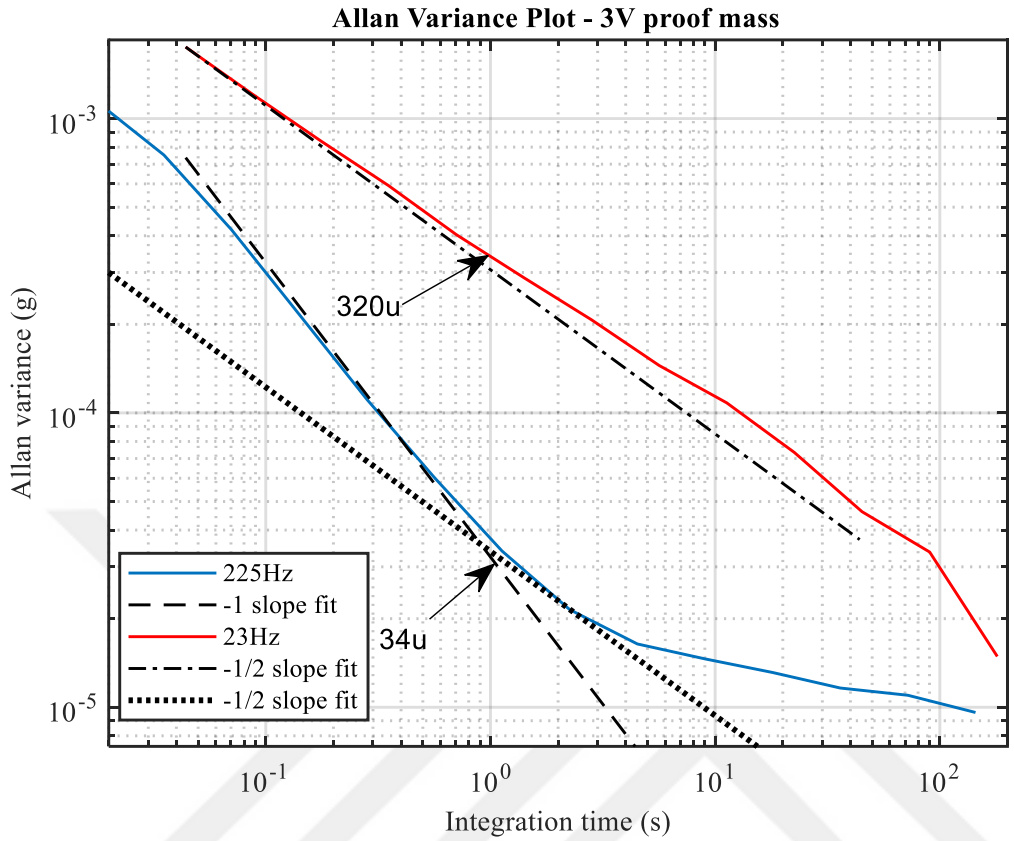

Figure 5.21: The effect of data rate on the data with dominant quantization noise. The noise type changes (quantization to white noise), and the noise performance degrades (34µg/√Hz to 320µg/√Hz) as the data rate reduces from 225Hz to 23Hz.

The last two figures (Figure 5.20 and Figure 5.21) show that data rate also affects the sensor noise. A lower data rate increases the noise level if white noise is present in the sensor data. If quantization noise is prominent in the sensor data, decreasing the data rate introduces visual white noise. This explains the higher noise in the data collected by the digital readout circuit (147K sampling rate and 20Hz data rate) compared to the data collected by the lock-in-amplifier (200M sampling rate and 225Hz data rate).

5.7 Summary of discussion

This chapter presents the results of a resonant MEMS accelerometer with a digital control loop using a microcontroller-based compact readout circuit. This readout circuit performs all the functions required to operate a resonant MEMS accelerometer, such as frequency sweeping, scale factor calculations, closed-loop operation, and acquiring temperature immune sensor data. The frequency sweep results show that optimum values of proof-mass voltage and the excitation voltage can operate the resonators at the desired gain value without going into a non-linear region. The scale factor (95Hz/g) is calculated accurately at different biasing conditions. This test also verifies the frequency tracking algorithm implemented in the microcontroller. The data obtained from the sensor shows a bias instability of 9.7µg, which is very close to the value obtained from the sensor using a lock-in-amplifier setup (7µg). However, the white noise in the data is higher owing to a lower data rate and sampling frequency. A temperature compensation algorithm implemented in the microcontroller significantly reduces the temperature effect, resulting in a three times improvement in the bias instability (54µg to 18µg).

CHAPTER 6

CONCLUSION AND THE FUTURE WORK

Several applications, ranging from commercial to inertial, use MEMS accelerometers. Resonant MEMS accelerometers have several advantages compared to other types of MEMS accelerometers, such as digital quasi-output, extended dynamic range, low electronic noise, immunity to temperature, and better sensitivity are some of the main features of a resonant MEMS accelerometer. This study presents a new digital control loop-based compact readout circuit for a resonant MEMS accelerometer providing high performance with reduced temperature and power supply dependence while utilizing low processing power. Digitalization increases the flexibility in modifying the sensor parameters, such as bandwidth, gets rid of noisy electronic components, and implements multiple algorithms to improve sensor performance. Section 6.1 presents a conclusion of this study while summarizing the main points. Section 6.2 suggests a few improvements for any future work aimed at improving the performance of a readout circuit for the resonant MEMS accelerometers.

6.1 Conclusion

A resonant MEMS accelerometer's readout circuit can be divided into three main parts. The first part is the pre-amplifier stage that converts the low motional current into voltage with significant gain. The second part of the readout circuit keeps the resonators vibrating at their resonance frequency, and a closed-loop operation is realized. The third part of the circuit is the frequency counting part which extracts frequency information from the circuit. In the digital control loop implementation, both the oscillation sustaining and frequency extraction is performed in the digital

domain; however, the pre-amplifier stage is a must for the digital implementation as well.

The resonant MEMS accelerometer sensors used in this study are characterized at the chip level and amplifier-PCB module level using a dynamic signal analyzer (DSA) and a lock-in-amplifier setup, performing FFT and frequency sweep tests. Based on the results of chip-level testing, detailed testing is performed with the lock-in-amplifier to understand the behavior of the resonant MEMS accelerometers. The frequency sweeping is performed under several values of the proof mass and the excitation voltage. The results show that the gain of the resonators is directly proportional to the proof mass voltage, and the excitation voltage has no significant effect on the resonator gain. The resonance frequency of the resonators does not change more than a few Hertz as the proof mass and the excitation voltage varies. The excitation voltage has a significant effect on the linearity of the resonators. A high excitation voltage drives the resonators in non-linear regions, which is undesirable. The threshold of the excitation voltage to keep the operation linear is changed under different proof mass voltage values. The higher the proof mass voltage, the lower the threshold for the excitation voltage. The scale factor of the sensor is calculated by adding the sensitivity of each resonator. The resonators of the sensor used in the characterization are not mechanically identical due to fabrication-related problems. The sensitivity of *Resonator 1* (sensor-N4N2[2]) is 45Hz/g, and the sensitivity of *Resonator 2* (sensor-N4N2) is 50Hz/g. The scale factor of the sensor is approximately 95Hz/g. The scale factor is calculated under different biasing conditions. The results show that the scale factor of the sensor is not affected by changes in the biasing conditions. The data collected from the sensor using a lock-in-amplifier shows a bias instability of 7µg and a noise value of 10µg/√Hz. The bias instability and noise value differ under different biasing conditions.

[2] Sensor-N4N2 is used for digital control loop realization with the digital control PCB. The mis-match in the resonance frequency is also observed in other resonant MEMS accelerometers.

In the digital control loop implementation, a charge-sensing pre-amplifier stage converts the motional current into voltage, achieving a significant gain. The voltage data is converted to the digital domain using a 16-bit ADC with a sampling rate of 147kS/s. All the functionalities of oscillation sustaining and frequency demodulation are performed in the digital domain. The amplitude information is extracted using the full wave rectification method from the input signal. A peripheral-integral (PI) controller is implemented in the microcontroller to maintain the sensor output at a set-point value. The PI controller controls the excitation voltage amplitude to maintain the sensor output. A PLL is implemented in the microcontroller to track the resonance frequency of the resonators. A timed reference technique is used in this study to implement the PLL while utilizing minimal processor resources. The amplitude and frequency information is used to generate the drive signal using a 16-bit DAC, which has a refresh rate of 5µs.

A Simulink model is also presented to simulate the proposed system, using parameters of the actual sensor obtained in the sensor characterization process. This model incorporates the effect of the microcontroller parameters and adds the noise sources to make it more related to the actual implementation. The simulation results show the model's amplitude stabilization and frequency tracking capability.

The digital control loop is implemented using a PCB based on the stm32 microcontroller. The frequency sweep tests are performed with the digital PCB to obtain resonance frequency and gain of the resonators under different biasing conditions, and the results from the digital PCB are consistent with the sensor characterization results obtained using a lock-in-amplifier. The bias instability calculated from the sensor data is 9.7µg which is very close to the value obtained by a lock-in-amplifier (7µg). The frequency resolution of the readout circuit is experimentally tested by reading sine signal from thre sources (lock-in-amplifier, dynamic signal analyzer, and signal generator), and found as 16.1µg , 16.9µg, and 18.6µg for the loc-in-amplifier, DSA, and signal generator respectively. This corresponds to a minimum noise level of 0.23µg/√Hz. The sensitivity of *Resonator 1* is 45Hz/g, and the sensitivity of *Resonator 2* is 50Hz/g. The scale factor calculated

with the readout circuit, 95Hz/g, is also consistent and accurate. The differential operation of the resonant MEMS accelerometer ensures insensitivity to temperature. However, due to a mismatch in the sensitivity of the resonators, temperature dependency exists in the sensor data. The temperature compensation improves the bias instability of the sensor by three times (54µg to 18µg).

6.2 Future work

The resonance frequency of the resonators of the resonant MEMS accelerometers used in this study is between 16~17kHz. The maximum sampling rate achievable by the ADC is 1M samples per second, but the sampling rate used in the study is approximately 147K samples per second. Oversampling and decimation techniques can significantly improve the quality of the input samples. Therefore, using a high sampling rate is recommended to acquire the input signal, but the microcontroller speed limits the sampling rate. The microcontroller used in this study operates at 169MHz clock speed, making a sampling rate higher than 147K challenging without affecting the other functionalities of the microcontroller. A 2 or 3 times faster processor can accommodate a higher sampling rate and allow decimating input samples to obtain less noisy data.

A microcontroller completes its instructions sequentially. A delay in one of the instructions affects the performance of the following instructions. An interrupt-based design is used in this study to perform different functionalities to produce a parallel processing effect. However, at the low-level coding, different interrupts operate sequentially and affect the performance of the implemented algorithm. For example, in this study, a UART is used to transmit the frequency information to a computer. This functionality operates in parallel with the primary function of the microcontroller. The serial transmission is slower than the interrupt frequency of the main loop. Using a fast microcontroller can improve the performance of a single sensor and may accommodate two or three sensors. However, increasing the number of sensors makes processing challenging for a microcontroller. An FPGA is

recommended for the integration of a higher number of sensors. However, the biggest drawback of an FPGA is developing code for all the basic functionalities from scratch compared to readily available in-built microcontroller functions.

The sensitivity of a resonator is an important performance parameter of a resonant MEMS accelerometer. There are different techniques to enhance the sensitivity of a resonator. The first method is to increase the proof mass of the sensor because a higher proof mass will produce more stress in the resonators. Secondly, a lever structure can also increase a resonator's sensitivity without increasing the proof mass's size. Another method to increase sensitivity is spring softening. The stiffness of a spring can be softened by mechanical design or electrostatic induction. It is recommended for a future study that the electrostatic spring softening effect to enhance the sensitivity should be implemented using a digital control loop. The digital control implementation used in this study provides a biasing voltage to proof mass and wafer cap. It can also provide a biasing voltage to the sensitivity-enhancing electrodes to change the sensitivity according to any application requirement.

REFERENCES

[1] H. Yanazawa and K. Homma, "Growing market of MEMS and technology development in process and tools specialized to MEMS," in *2017 IEEE Electron Devices Technology and Manufacturing Conference (EDTM)*, 2017, pp. 143-144.

[2] J. Bryzek, S. Roundy, B. Bircumshaw, C. Chung, K. Castellino, J. R. Stetter, *et al.*, "Marvelous MEMS," *IEEE Circuits and Devices Magazine*, vol. 22, pp. 8-28, 2006.

[3] S. Seonho, K. Hak, and C. Kukjin, "An inertial-grade laterally-driven MEMS differential resonant accelerometer," in *SENSORS, 2004 IEEE*, 2004, pp. 654-657 vol.2.

[4] R. K. J, "Applications of MEMS in surgery," *Proceedings of the IEEE*, vol. 92, pp. 43-55, 2004.

[5] M. Ali, "Compensation of temperature and acceleration effects on MEMS gyroscope," in *2016 13th International Bhurban Conference on Applied Sciences and Technology (IBCAST)*, 2016, pp. 274-279.

[6] X. Wang, J. Zhao, Y. Zhao, G. M. Xia, A. P. Qiu, Y. Su, *et al.*, "A 0.4 μg Bias Instability and 1.2 μg/√Hz Noise Floor MEMS Silicon Oscillating Accelerometer With CMOS Readout Circuit," *IEEE Journal of Solid-State Circuits*, vol. 52, pp. 472-482, 2017.

[7] C. Zhao, M. Pandit, G. Sobreviela, P. Steinmann, A. Mustafazade, X. Zou, *et al.*, "A Resonant MEMS Accelerometer With 56ng Bias Stability and 98ng/√Hz Noise Floor," *Journal of Microelectromechanical Systems*, vol. 28, pp. 324-326, 2019.

[8] T. A. Roessig, R. T. Howe, A. P. Pisano, and J. H. Smith, "Surface-micromachined resonant accelerometer," in *Proceedings of International Solid State Sensors and Actuators Conference (Transducers '97)*, 1997, pp. 859-862 vol.2.

[9] A. A. Seshia, M. Palaniapan, T. A. Roessig, R. T. Howe, R. W. Gooch, T. R. Schimert, *et al.*, "A vacuum packaged surface micromachined resonant accelerometer," *Journal of Microelectromechanical systems*, vol. 11, pp. 784-793, 2002.

[10] A. Partridge, J. K. Reynolds, B. W. Chui, E. M. Chow, A. M. Fitzgerald, L. Zhang, *et al.*, "A high-performance planar piezoresistive accelerometer," *Journal of Microelectromechanical Systems*, vol. 9, pp. 58-66, 2000.

[11] Z. Ghemari, "Study and analysis of the piezoresistive accelerometer stability and improvement of their performances," *International Journal of System Assurance Engineering and Management*, vol. 8, pp. 1520-1526, 2017/11/01 2017.

[12] W. Li-Peng, R. A. Wolf, W. Yu, K. K. Deng, L. Zou, R. J. Davis, *et al.*, "Design, fabrication, and measurement of high-sensitivity piezoelectric

microelectromechanical systems accelerometers," *Journal of Microelectromechanical Systems,* vol. 12, pp. 433-439, 2003.

[13] U. A. Dauderstadt, P. M. Sarro, and S. Middelhoek, "Temperature dependence and drift of a thermal accelerometer," in *Proceedings of International Solid State Sensors and Actuators Conference (Transducers '97)*, 1997, pp. 1209-1212 vol.2.

[14] X. Wu, X. Wang, S. Li, S. Huang, Q. Ge, and B. Yu, "Cantilever Fiber-Optic Accelerometer Based on Modal Interferometer," *IEEE Photonics Technology Letters,* vol. 27, pp. 1632-1635, 2015.

[15] A. Aydemir, Y. Terzioglu, and T. Akin, "A new design and a fabrication approach to realize a high performance three axes capacitive MEMS accelerometer," *Sensors and Actuators A: Physical,* vol. 244, pp. 324-333, 2016.

[16] Y. Zhao, J. Zhao, X. Wang, G. M. Xia, A. P. Qiu, Y. Su, *et al.*, "A Sub-μg Bias-Instability MEMS Oscillating Accelerometer With an Ultra-Low-Noise Read-Out Circuit in CMOS," *IEEE Journal of Solid-State Circuits,* vol. 50, pp. 2113-2126, 2015.

[17] X. Xiong, W. Zheng, K. Wang, Z. Li, W. Yang, and X. Zou, "Sensitivity Enhancement of Mems Resonant Accelerometers by Using Electrostatic Spring," in *2020 IEEE International Symposium on Inertial Sensors and Systems (INERTIAL)*, 2020, pp. 1-3.

[18] H. Gu, W. Su, B. Zhao, H. Zhou, and X. Liu, "A Design Methodology of Digital Control System for MEMS Gyroscope Based on Multi-Objective Parameter Optimization," *Micromachines,* vol. 11, 2020.

[19] J. Zhao, X. Wang, Y. Zhao, G. M. Xia, A. P. Qiu, Y. Su, *et al.*, "A 0.23 μg Bias Instability and 1 μg/√Hz Acceleration Noise Density Silicon Oscillating Accelerometer With Embedded Frequency-to-Digital Converter in PLL," *IEEE Journal of Solid-State Circuits,* vol. 52, pp. 1053-1065, 2017.

[20] G. Vigevani, F. T. Goericke, A. P. Pisano, I. I. Izyumin, and B. E. Boser, "Microleverage DETF Aluminum Nitride resonating accelerometer," in *2012 IEEE International Frequency Control Symposium Proceedings*, 2012, pp. 1-4.

[21] H. Ding, X. Le, Y. Ma, and J. Xie, "A biaxial resonant tilt sensor with two-stage microleverage mechanisms," in *2017 19th International Conference on Solid-State Sensors, Actuators and Microsystems (TRANSDUCERS)*, 2017, pp. 1013-1016.

[22] H. Ding, J. Zhao, B.-F. Ju, and J. Xie, "A new analytical model of single-stage microleverage mechanism in resonant accelerometer," *Microsystem Technologies,* vol. 22, pp. 757-766, 2016.

[23] F. Mohd-Yasin, D. J. Nagel, and C. E. Korman, "Noise in MEMS," *Measurement Science and Technology,* vol. 21, p. 012001, 2009/11/06 2009.

[24] R. Melamud, S. A. Chandorkar, B. Kim, H. K. Lee, J. C. Salvia, G. Bahl, *et al.*, "Temperature-Insensitive Composite Micromechanical Resonators," *Journal of Microelectromechanical Systems,* vol. 18, pp. 1409-1419, 2009.

[25] J. Du, Y. Guo, Y. Lin, X. Zheng, and Z. Jin, "A real-time temperature compensation algorithm for a force-rebalanced MEMS capacitive accelerometer based on resonant frequency," in *2017 IEEE 12th International Conference on Nano/Micro Engineered and Molecular Systems (NEMS)*, 2017, pp. 214-217.
[26] H. Lin, X. Yong-Ping, and Q. Anping, "Folded silicon resonant accelerometer with temperature compensation," in *SENSORS, 2004 IEEE*, 2004, pp. 512-515 vol.1.
[27] U. Park, J. Rhim, J. U. Jeon, and J. Kim, "A micromachined differential resonant accelerometer based on robust structural design," *Microelectronic Engineering*, vol. 129, pp. 5-11, 2014.
[28] A. A. Trusov, S. A. Zotov, B. R. Simon, and A. M. Shkel, "Silicon accelerometer with differential Frequency Modulation and continuous self-calibration," in *2013 IEEE 26th International Conference on Micro Electro Mechanical Systems (MEMS)*, 2013, pp. 29-32.
[29] S. Shin, A. Daruwalla, M. Gong, H. Wen, and F. Ayazi, "A Piezoelectric Resonant Accelerometer for Above 140db Linear Dynamic Range High-G Applications," in *2019 20th International Conference on Solid-State Sensors, Actuators and Microsystems & Eurosensors XXXIII (TRANSDUCERS & EUROSENSORS XXXIII)*, 2019, pp. 503-506.
[30] S. A. Zotov, B. R. Simon, A. A. Trusov, and A. M. Shkel, "High Quality Factor Resonant MEMS Accelerometer With Continuous Thermal Compensation," *IEEE Sensors Journal*, vol. 15, pp. 5045-5052, 2015.
[31] G. Xia, Y. Zhao, J. Zhao, Q. Shi, and A. Qiu, "Silicon vibrating beam accelerometer with ppm grade scale factor stability and tens-ppm grade full-range nonlinearity," in *2016 IEEE International Symposium on Inertial Sensors and Systems*, 2016, pp. 117-118.
[32] D. D. Shin, C. H. Ahn, Y. Chen, D. L. Christensen, I. B. Flader, and T. W. Kenny, "Environmentally robust differential resonant accelerometer in a wafer-scale encapsulation process," in *2017 IEEE 30th International Conference on Micro Electro Mechanical Systems (MEMS)*, 2017, pp. 17-20.
[33] D. D. Shin, Y. Chen, I. B. Flader, and T. W. Kenny, "Epitaxially encapsulated resonant accelerometer with an on-chip micro-oven," in *2017 19th International Conference on Solid-State Sensors, Actuators and Microsystems (TRANSDUCERS)*, 2017, pp. 595-598.
[34] H. Ding, C. Wu, and J. Xie, "A MEMS Resonant Accelerometer With High Relative Sensitivity Based on Sensing Scheme of Electrostatically Induced Stiffness Perturbation," *Journal of Microelectromechanical Systems*, vol. 30, pp. 32-41, 2021.
[35] M. Riverola, G. Sobreviela, F. Torres, A. Uranga, and N. Barniol, "Single-Resonator Dual-Frequency BEOL-Embedded CMOS-MEMS Oscillator With Low-Power and Ultra-Compact TIA Core," *IEEE Electron Device Letters*, vol. 38, pp. 273-276, 2017.
[36] C. Comi, A. Corigliano, G. Langfelder, A. Longoni, A. Tocchio, and B. Simoni, "A Resonant Microaccelerometer With High Sensitivity Operating

in an Oscillating Circuit," *Journal of Microelectromechanical Systems,* vol. 19, pp. 1140-1152, 2010.

[37] H. D. Gavcar, K. Azgin, S. E. Alper, and T. Akin, "An automatic acceleration compensation system for a single-mass MEMS gyroscope," in *2015 Transducers - 2015 18th International Conference on Solid-State Sensors, Actuators and Microsystems (TRANSDUCERS)*, 2015, pp. 19-22.

[38] A. Sharma, M. F. Zaman, and F. Ayazi, "A 104-dB Dynamic Range Transimpedance-Based CMOS ASIC for Tuning Fork Microgyroscopes," *IEEE Journal of Solid-State Circuits,* vol. 42, pp. 1790-1802, 2007.

[39] B. Razavi, "A 622 Mb/s 4.5 pA/√Hz CMOS transimpedance amplifier [for optical receiver front-end]," in *2000 IEEE International Solid-State Circuits Conference. Digest of Technical Papers (Cat. No.00CH37056)*, 2000, pp. 162-163.

[40] G. Xia, A. Qiu, Q. Shi, and Y. Su, "A wafer level vacuum packaged silicon vibration beam accelerometer," in *2015 IEEE International Symposium on Inertial Sensors and Systems (ISISS) Proceedings*, 2015, pp. 1-4.

[41] B. Yang, Y. X. Xu, Q. F. Hu, B. Yang, C. Y. Xing, and X. Rui, "Reserch on digital closed-loop control for silicon resonant accelerometer," in *2018 25th Saint Petersburg International Conference on Integrated Navigation Systems (ICINS)*, 2018, pp. 1-4.

[42] L. Xu, J. Xi, L. Gao, F. Li, J. Pi, C. Li, *et al.*, "A Closed-Loop System for Resonant MEMS Sensors Subject to Blue-Sideband Excitation," *Journal of Microelectromechanical Systems,* vol. 31, pp. 690-699, 2022.

[43] T. Fujita, H. Okada, K. Iguchi, and K. Maenaka, "Digital-controlled MEMS vibratory-beam-accelerometer," in *2008 World Automation Congress*, 2008, pp. 1-6.

[44] M. Saukoski, L. Aaltonen, and K. A. I. Halonen, "Effects of Synchronous Demodulation in Vibratory MEMS Gyroscopes: A Theoretical Study," *IEEE Sensors Journal*, vol. 8, pp. 1722-1733, 2008.

[45] L. Niannian, L. Dachuan, C. Jian, L. Longtao, C. Xiaozhu, Y. Zhenchuan, *et al.*, "An FPGA implementation of the LMS adaptive filter for MEMS gyroscope," in *2010 IEEE 5th International Conference on Nano/Micro Engineered and Molecular Systems*, 2010, pp. 744-747.

[46] D. Liu, C. He, Q. Zhao, Z. Yang, Y. Hao, and G. Yan, "Digital signal processing for a micromachined vibratory gyroscope based on a three dimensional adaptive filter demodulator," *Measurement,* vol. 50, pp. 198-202, 2014/04/01/ 2014.

[47] U. Sönmez, H. Külah, and T. Akın, "A ΣΔ micro accelerometer with 6μg/√Hz resolution and 130 dB dynamic range," *Analog Integrated Circuits and Signal Processing,* vol. 81, pp. 471-485, 2014.

[48] I. E. Ocak, R. Kepenek, H. Kulah, and T. Akin, "A high performance Σ-Δ readout circuitry for μg resolution microaccelerometers," *Analog Integrated Circuits and Signal Processing,* vol. 64, pp. 137-145, 2010.

[49] L. He, Y. P. Xu, and M. Palaniapan, "A CMOS Readout Circuit for SOI Resonant Accelerometer With 4μg Bias Stability and 20μg/√Hz Resolution," *IEEE Journal of Solid-State Circuits*, vol. 43, pp. 1480-1490, 2008.
[50] A. Tocchio, A. Caspani, G. Langfelder, A. Longoni, and E. Lasalandra, "A Pierce oscillator for MEMS resonant accelerometer with a novel low-power amplitude limiting technique," in *2012 IEEE International Frequency Control Symposium Proceedings*, 2012, pp. 1-6.
[51] H. Kulah, J. Chae, N. Yazdi, and K. Najafi, "Noise analysis and characterization of a sigma-delta capacitive microaccelerometer," *IEEE Journal of Solid-State Circuits*, vol. 41, pp. 352-361, 2006.
[52] B. E. Boser and R. T. Howe, "Surface micromachined accelerometers," *IEEE Journal of Solid-State Circuits*, vol. 31, pp. 366-375, 1996.
[53] M. Lemkin and B. E. Boser, "A three-axis micromachined accelerometer with a CMOS position-sense interface and digital offset-trim electronics," *IEEE Journal of Solid-State Circuits*, vol. 34, pp. 456-468, 1999.
[54] Z. J. Towfic and A. H. Sayed, "Clock jitter estimation in noise," in *2011 IEEE International Symposium of Circuits and Systems (ISCAS)*, 2011, pp. 1251-1254.
[55] E. Rubiola, "Phase noise and frequency stability," in *Phase Noise and Frequency Stability in Oscillators*, E. Rubiola, Ed., ed Cambridge: Cambridge University Press, 2008, pp. 1-34.
[56] M. Agarwal, K. K. Park, B. Kim, M. A. Hopcroft, S. A. Chandorkar, R. N. Candler, *et al.*, "Amplitude noise induced phase noise in electrostatic MEMS resonators," in *Solid State Sensor, Actuator, and Microsystems Workshop*, 2006.
[57] B. Eminoglu, "High Performance FM Gyroscopes," Ph.D. , Electrical Engineering and Computer Sciences, University of California, Berkeley, 2017.
[58] M. Tohidian, A. F. Ahmady, and M. Kamarei, "A simplified method for phase noise calculation," in *2009 IEEE Custom Integrated Circuits Conference*, 2009, pp. 535-538.
[59] T. H. Lee and A. Hajimiri, "Oscillator phase noise: a tutorial," *IEEE Journal of Solid-State Circuits*, vol. 35, pp. 326-336, 2000.
[60] (December 11). *"How Quantization and Thermal Noise Determine an ADC's Effective Noise Figure"*. Available: https://www.analog.com/en/technical-articles/how-quantization-and-thermal-noise-determine-an-adcs-effective-noise-figure.html
[61] X. Niu, Q. Wang, Y. Li, Q. Li, and J. Liu, "Using Inertial Sensors in Smartphones for Curriculum Experiments of Inertial Navigation Technology," *Education Sciences*, vol. 5, pp. 26-46, 03/01 2015.
[62] (December 11). *"Accelerometer Specifications - Quick Definitions"*. Available: https://www.analog.com/en/products/landing-pages/001/accelerometer-specifications-definitions.html
[63] Z. Jian, W. Xi, Z. Yang, X. Guo Ming, Q. An Ping, S. Yan, *et al.*, "A 0.23 μg bias instability and 1.6 μg/√Hz resolution silicon oscillating

accelerometer with build-in Σ-Δ frequency-to-digital converter," in *2016 IEEE Symposium on VLSI Circuits (VLSI-Circuits)*, 2016, pp. 1-2.

CURRICULUM VITAE

Surname, Name: Ali, Muhammad

EDUCATION

Degree	Institution	Year of Graduation
MS	METU Electrical and Electronics Engineering, Ankara	2014
BS	NUST, Islamabad, Pakistan	2008
High School	BISE Abbottabad, Pakistan	2004

FOREIGN LANGUAGES

English, Basic Turkish, Urdu (native language)

PUBLICATIONS

1. M. Ali, “Compensation of temperature and acceleration effects on MEMS gyroscope,” *2016 13th International Bhurban Conference on Applied Sciences and Technology (IBCAST)*, 2016, pp. 274-279

INTERESTS

Cricket, Football, Tennis, Computer Technologies, Movies